

GENERATION AND ANALYSIS OF LIKELY HYDROLOGIC SCENARIOS FOR THE SOUTHERN SANTA CRUZ RIVER

by

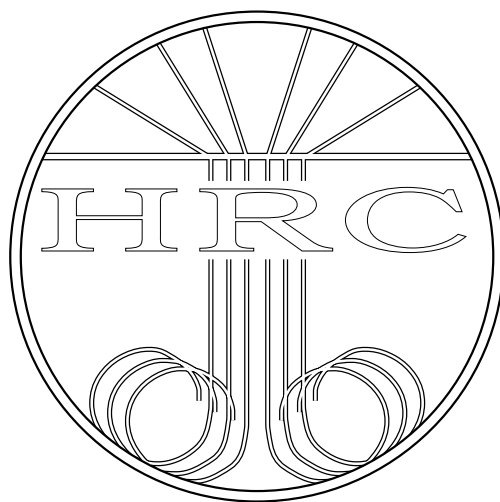
Eylon Shamir, Konstantine P. Georgakakos, Nicholas E. Graham, and Jianzhong Wang

with Annex A by

David M. Meko, University of Arizona, Laboratory of Tree-Ring Research

Sponsored by

The Arizona Department of Water Resources
(*AWARD No: 2005-2568*)



HRC Technical Report No. 4

Hydrologic Research Center
12780 High Bluff Drive, Suite 250
San Diego, CA 92130, USA

December 28, 2005

Generation and Analysis of Likely Hydrologic Scenarios for the Southern Santa Cruz River

Eylon Shamir, Ph.D.
Konstantine P. Georgakakos, Sc.D.
Nicholas E. Graham, Ph.D.
Jianzhong Wang, Ph.D.

with Annex A by

David Meko, Ph.D.
University of Arizona, Laboratory of Tree-Ring Research

Contents

Acknowledgements

Executive Summary

Chapter A:	Statistical Analysis of the Flow at the Nogales Gauge
Chapter B:	Stochastic Streamflow Modeling
Chapter C:	Synthetic Flow Model ARMA(1,1)
Chapter D:	Streamflow Scenarios with Dendrochronology Information
Chapter E:	Cost Loss Ratio Analysis for Santa Cruz Flows at Nogales
Chapter F:	Simplified Conceptual Groundwater Model for Santa Cruz River Microbasins
Chapter G:	Use of Modeling for Risk Analysis
Chapter H:	Conclusions and Recommendations
Chapter I:	References
Annex A:	Tree-Ring Reconstruction of Annual and Seasonal Precipitation at Nogales, Arizona
Annex B:	Notes from Field Tour of the Santa Cruz River (SCAMA and Mexican Regions)

ACKNOWLEDGEMENTS

The work that led to this report was sponsored by the Arizona Department of Water Resources (AZDWR) under Award No. 2005-2568. The study was conducted by the Hydrologic Research Center (HRC) in close collaboration with AZDWR staff. Special thanks are extended to the ADWR personnel Frank Corkhill, Gretchen Erwin, Keith Nelson, Frank Putman and Alejandro Barcenas for provided data and guidance, as well as insightful comments throughout the preparation of this report. As part of this study, HRC delivered to AZDWR MATLAB-based software (GENFLOW) that is capable of generating likely flow scenarios at the Nogales gauge site. The opinions expressed in this report are those of the authors and need not necessarily reflect those of the funding agency.

This is a technical report of the Hydrologic Research Laboratory (HRC), a nonprofit public benefit corporation. Printed copies of this report may be obtained by writing to: Managing Director, Hydrologic Research Center, 12780 High Bluff Drive, Suite 250, San Diego, CA 92130, USA.

EXECUTIVE SUMMARY

The mission of the Santa Cruz Active Management Area (SCAMA) in arid southern Arizona is to “conjunctively manage all water resources in the AMA and to assure reliable water supply for current and future uses, protecting aquatic and riparian habitat while sustaining a healthy economy.” The management goal of the SCAMA is “to maintain a safe-yield condition and to prevent local water tables from experiencing long term declines.”

To accommodate this goal, the AZDWR plans to use MODFLOW, a groundwater flow model, for the aquifers in the SCAMA. These aquifers are fed mainly by recharge along the Santa Cruz River. The objective of the present project is to develop models capable of simulating long-term climatic and hydrologic regimes and associated Santa Cruz River flows for the Nogales gauge site. The flows will be used to estimate groundwater recharge for several microbasins in SCAMA. Using the results of this study, likely future groundwater levels may be estimated under a variety of water demand scenarios for the planning of future water consumption that will maintain safe yield.

In this work, models were developed to generate plausible daily flow scenarios for the Nogales gauge which is located about 10 km east of the city of Nogales, Arizona. The drainage area of the USGS gauge near Nogales is about 1,400 km², of which approximately 1,150 km² are located in Mexico. Analysis of the observed streamflow record of this gauge for the years 1936 through 2003 revealed high year to year variability, with decreasing summer flows and increasing variability of monthly flows since the 70s. Winter-season precipitation in this region was found statistically related to the equatorial Pacific Ocean sea surface temperature (El-Niño events).

The models were built for four seasons, and the wet seasons (summer and winter) were divided into years that are relatively wet, medium or relatively dry. Such model configuration maintains the variability in a given year as well as the year-to-year variability. The models consist of: 1) a stochastic model of hourly precipitation scenarios that maintains the characteristics and variability of a 45-year hourly precipitation record from a nearby raingauge; and 2) a physically-based conceptual model that transforms the precipitation into daily streamflow using variable infiltration rates and estimates the basin’s antecedent moisture conditions.

Long term (i.e., 100 years) realizations (forming an ensemble) are generated by the above described models for two different regimes: the first regime is that of the historical rain gauge record and the second regime is based on reconstructed paleo-climatic precipitation estimates. For the latter regime, winter-season and annual precipitation were reconstructed for the Nogales gauge site based on tree ring chronologies. The reconstructed record, which spans the period 1654 through 1966, is used to generate a second ensemble of 100 realizations which spans 317 years.

Utilizing the simulated ensembles in water resources planning requires running the likely streamflow realizations in conjunction with the MODFLOW ground water model. Although MODFLOW has been implemented successfully by AZDWR staff in the area of interest with high spatial resolution, at present running this model in ensemble mode for long durations (e.g. 100 years) is not feasible. To provide initial ensemble groundwater content estimates from the

flow ensembles and to facilitate water resources planning under uncertainty, a simplified model that mimics MODFLOW behavior in the region of interest was developed. Application of this simplified model was made for the four microbasins downstream of the Nogales gauge, taking into consideration alluvial groundwater recharge, evapotranspiration and pumping losses.

To exemplify the use of the models developed for water resources planning, a risk analysis case study was conducted in which the two flow ensembles (historical and paleo-climatic) were used to evaluate the risk of each of the four microbasins declining below a predefined groundwater content threshold. Risk was measured in terms of the frequency of both a single and several consecutive occurrences of aquifer storage declines below a given threshold. The analysis used hypothesized monthly pumping scenarios and two parameters: (a) the level of risk that is considered acceptable, and (b) the threshold level or content that should be maintained in each of the microbasins.

Perhaps the main conclusion of this work is that the modeling system developed reproduces most of the variability characteristics of the historical streamflow record and it may be used to produce likely future scenarios of streamflow for screening risk analyses pertaining to the likely behavior of the groundwater volume and level in the microbasins of the south Santa Cruz River region under a variety of development scenarios. In conjunction with the detailed groundwater modeling tools of the Arizona Department of Water Resources the models and data developed form a powerful planning tool. Main recommendations are: (a) the use of risk analysis as exemplified in this work in collaboration with regional officials and agencies to establish policy regarding regional development in the microbasins region of the south Santa Cruz River; (b) application in other semi-arid or arid regions; and (c) incorporation of climate change scenarios to possibly improve the generation of future ensembles of Santa Cruz River streamflow.

TABLE OF CONTENTS

Acknowledgements	i
Executive Summary	iii
Table of Contents	v
Chapter A: Statistical Analysis of the Flow at the Nogales Gauge	A- 1-22
Chapter B: Stochastic Streamflow Modeling	B- 1-32
Chapter C: Synthetic Flow Model ARMA(1,1)	C- 1-16
Chapter D: Streamflow Scenarios with Dendrochronology Information	D- 1-4
Chapter E: Cost Loss Ratio Analysis for Santa Cruz Flows at Nogales.....	E- 1-6
Chapter F: Simplified Conceptual Groundwater Model for Santa Cruz River Microbasins.....	F- 1-10
Chapter G: Use of Modeling for Risk Analysis - Examples	G- 1-6
Chapter H: Conclusions and Recommendations	H- 1-6
Chapter I: References	I- 1-2
Annex A: Tree-ring Reconstruction of Annual and Seasonal Precipitation at Nogales, Arizona.....	AA- 1-36
Annex B: Notes from Field Tour of the Santa Cruz River (SCAMA and Mexico regions).....	AB- 1-8

Chapter A

Statistical Analysis of the Flow at the Nogales Gauge

A.1 Introduction

In the following discussion we provide a statistical characterization of the flow at the Nogales Streamflow Gauge (U.S. Geological Survey gauge #9480500), hereinafter called the USGS Nogales gauge. The USGS Nogales gauge measures the flow of the upper Santa Cruz River, which is an ephemeral desert river that drains 550 square miles, of which approximately 450 square miles are located in Mexico (see field trip summary in Annex B). The mean daily streamflow data was acquired from the USGS National Weather Information System (NWIS) web site (<http://waterdata.usgs.gov/nwis>). The data form a complete continuous record for 7/1/1935 -9/30/2003, and additional periods include 1/1/1913-9/30/1915; 10/1/ 1916-6/30/1920; 4/28/1921-6/30/1922; and 5/1/1930-9/30/1933. For the statistical characterization of the flow we use the period 9/30/1935-10/1/2003, which is equivalent to the water years 1936 through 2003. A general map with the location of pertinent data sensors and a daily hydrograph of the USGS Nogales gauge are provided in Figures A-1 and A-2, respectively.

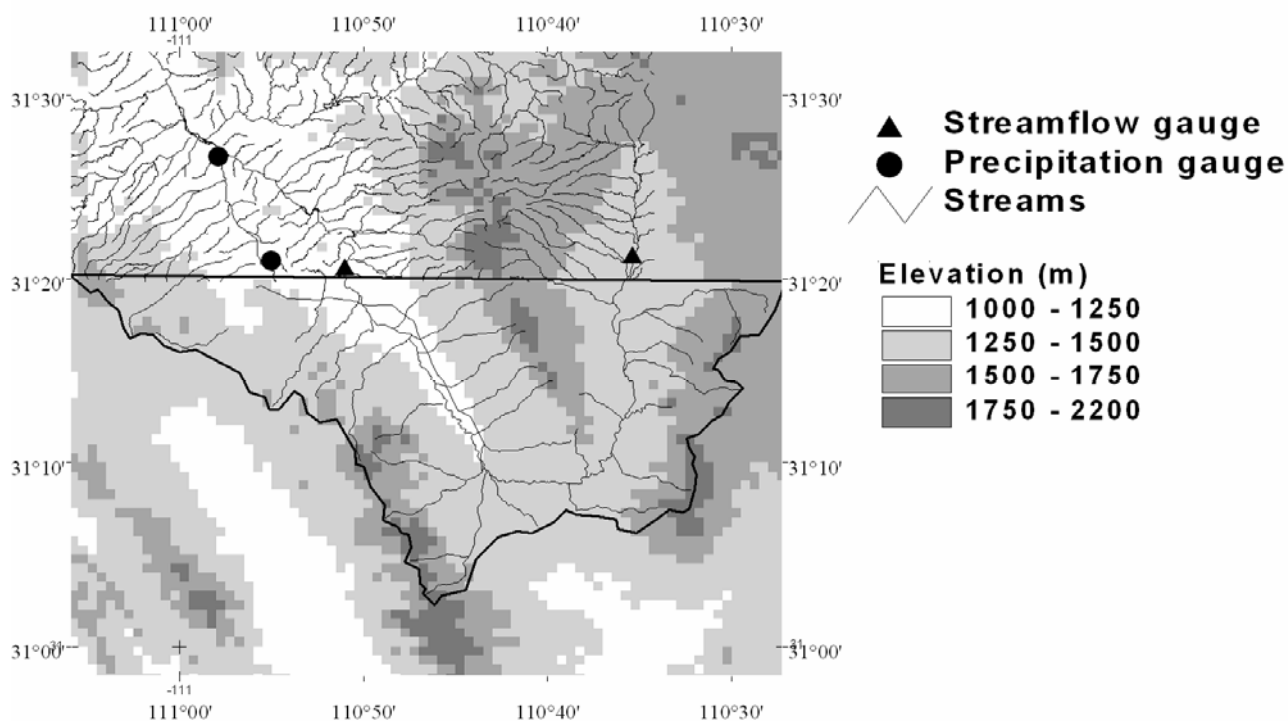


Figure A-1: Map of the Santa Cruz River, terrain elevation, and relevant data locations. Areas south of 31° 20' (thick solid line) are in Mexico.

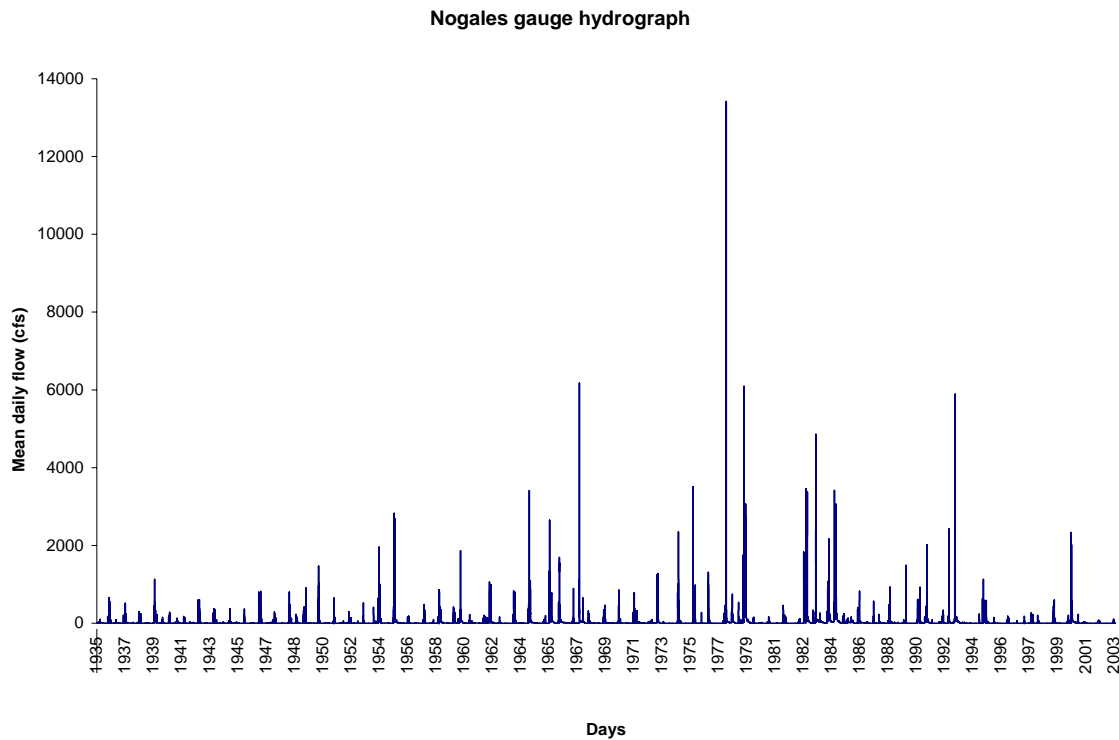


Figure A-2: Daily hydrograph (cubic feet per second, cfs) of Santa Cruz River at the Nogales stream gauge (1935-2003).

It is apparent that there are very few locations with available long-term precipitation and streamflow data upstream of or near the Nogales stream gauge. Figure A-2 also indicates that the streamflow record at the USGS Nogales gauge exhibits significant intermittence, and short- and long-term variability. Analysis of this variability is now pursued.

A.2 Daily Analysis

The exceedance probability plots of the daily flow are presented in Figure A-3 (left panel). In this Figure and in the right panel we present the exceedance of the Box-Cox transformed flow (*Box and Cox 1964*). This transformation is expressed as follows:

$$y_t = (x_t^\lambda - 1) / \lambda \quad (\text{A-1})$$

where x_t is the observed flow time series, t denotes time, and λ is a transformation parameter that is different than 0. For the special case of λ equal to zero the transformation is logarithmic. This power transformation is commonly used in hydrology to transform highly skewed time series into ones with normal distribution properties. Since the ranges and the variability are large this transformation is often used to facilitate

graphical presentation of the data. In this study, the λ parameter, unless mentioned otherwise, is assigned the value of 0.3 based on the recommendation of *Misrili, et al.* (2001).

Figure A-3 demonstrates the need for transformation. The left panel distribution possesses few extreme high values in very high percentiles with many more values throughout the rest of the percentile range. In the right panel, in which the Box-Cox transformation is used, there is a gradual increase in the flow values for higher percentiles.

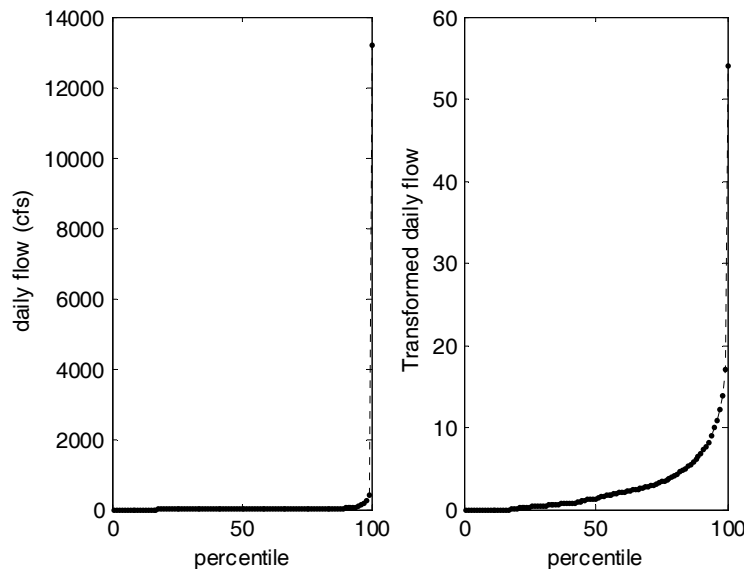


Figure A-3: The distribution of the untransformed mean daily flow (left panel) and the distribution of the Box-Cox transformed flow (right panel). The record is 67 years of daily flow values.

In Figure A-4 the number of peaks above a given flow threshold is shown. A peak in this case is defined as a flow value that is higher than the previous and the next daily flows. This analysis is done in order to gain perspective on the scale of flow that is driven directly by rainfall. We assume that the significant increase in flow above a given threshold is a result of rainfall in the basin. On the other hand small changes might be due to diurnal radiation variability that affects evaporation, evapotranspiration, or due to other natural or artificial (pumping) dynamics. The Figure shows that there is an exponential decline of the number of peaks that were counted with increasing threshold values.

The parametric descriptive statistics of the daily time series is provided in Table A-1. Items to note are: (a) the large variability in flows (compare standard deviation to mean), and (b) the high value of the skew coefficient that explains the difference between the mean and the median. In addition some persistence is exhibited in the daily values as inferred from the lag-1 autocorrelation coefficient value (ρ_1).

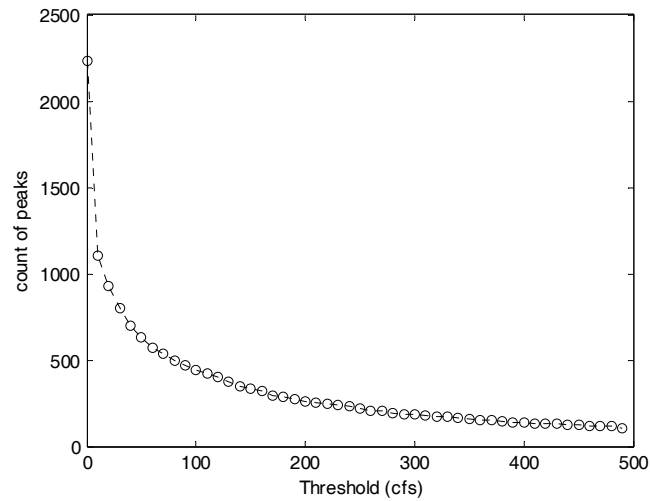


Figure A-4: Number of peaks of daily flow in the record that are above a given threshold.

Table A-1: Descriptive statistics of the daily flow, 1936-2002.

Sample size	Mean (cfs)	Median (cfs)	S.D. (cfs)	skew	ρ_1	ρ_2	Max (cfs)
24,834	26.6	2	180	33.7	0.56	0.25	13,200

A.3 Monthly and seasonal analysis

Aggregation of flow to seasons should provide time series with coherent signals. Such an aggregation is later used in the development of the synthetic model. Previously suggested seasons (*Webb and Betancourt 1990*) are July - August for summer, September - October for fall, November - February for winter. This division was considered for conducting flood analyses; however, for a water resources accounting study, March and April, which are water contributing months, need also be considered. The division to seasons may be based on statistical flow analysis to identify common traits among the various months, or on climate analysis to understand and aggregate flows based on the dominant atmospheric forcing for a given month.

To better understand the seasonality at the USGS Nogales gauge and to assess features of the monthly flow climate, we computed monthly statistics of the daily flow record. For such analysis the record duration was classified into 12 data samples, one for each month, and the statistics of each month were computed.

The most significant characteristic of the Santa Cruz River at the USGS Nogales gauge is that it remains dry in most days. Figure A-5(a) characterizes the intermittence of the stream for each month. It is shown that for all the months the chance to observe flow in the USGS Nogales gauge is lower than 50%, and the chance of occurrence possesses pronounced seasonality. August is clearly the month with the highest number of flow events, while the fewest flow events occur during May and June.

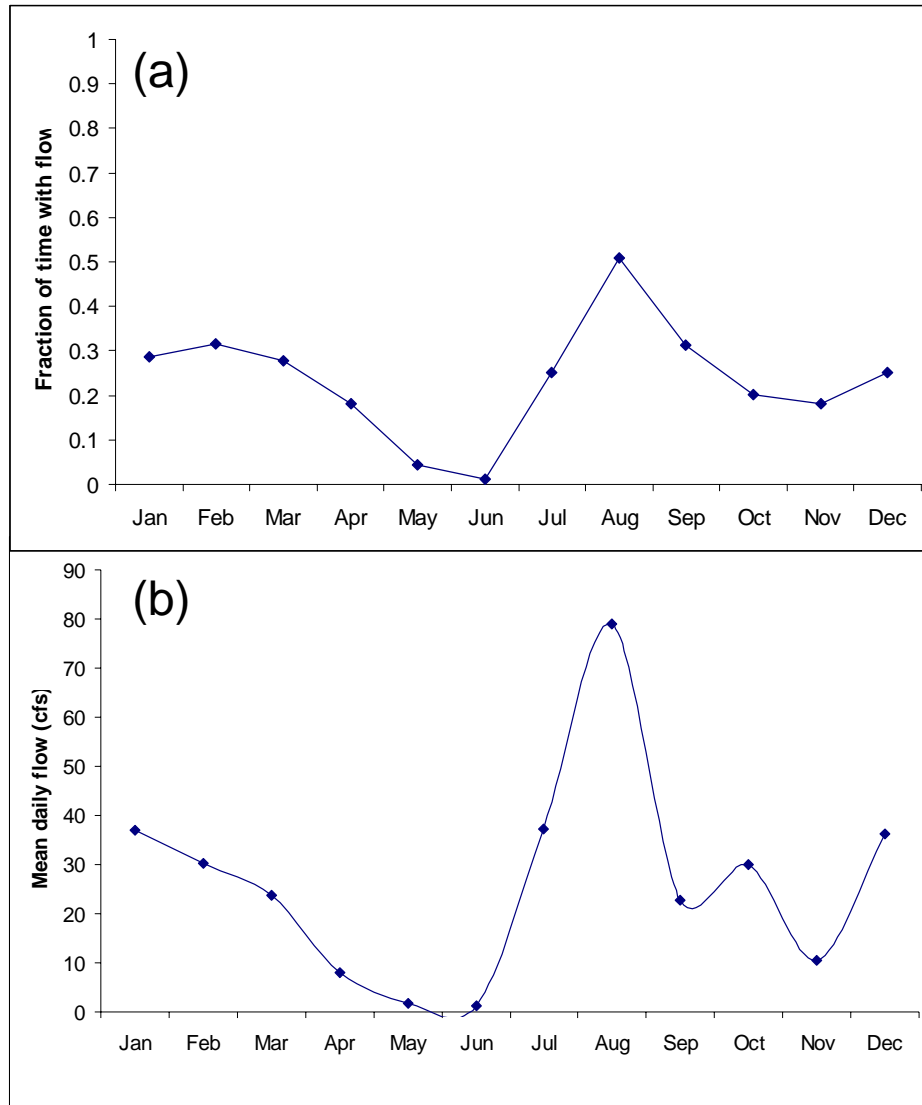


Figure A-5: Monthly statistics at the USGS Nogales gauge; (a) monthly fraction of days with flow; (b) monthly mean daily flow.

The monthly climatology of the mean daily flow is presented in Figure A-5(b). Significant seasonality is observed here too, with maximum flow in August and minimum flow in May and June. The seasonality characteristics in Figures A-5(a) and A-5(b) are in general agreement, suggesting that the frequency of occurrence of events is consistent with the quantity of the monthly yield. Contrary to this, it is noted that for the month of October fewer events were observed but with significantly higher flow

magnitude than for September. This is attributed to tropical storm contributions in October. Additional monthly descriptive statistics are provided in Table A-2. We note that in this Table the skew and kurtosis coefficients are normalized by the standard deviation to the third and fourth power, respectively, and they are adjusted for bias.

Table A-2: Long term monthly statistics of the mean daily flow for 1936-2003.

	Mean (cfs)	S.D (cfs)	Skew	Kurtosis	Max (cfs)
January	37	210	16	357	5880
February	30	123	16	360	3450
March	24	114	18	432	3340
April	8	19	8	90	337
May	2	4	5	37	56
June	1	12	18	349	300
July	37	143	11	189	3500
August	79	226	7	75	3410
September	23	89	14	301	2390
October	30	391	28	840	13200
November	10	56	22	580	1710
December	36	268	17	341	6160

It can be seen that the variability of flow is large and the coefficient of variation (the ratio between the standard deviation and the mean) varies from about 2 to about 10. The maximum record flow occurred in October (13,200 cfs). Next, monthly statistics of the mean daily flow peaks are presented in Table A-2. For the purpose of this analysis, a peak is defined as a daily flow event that is larger than 50 cfs, with mean daily flow that is greater than that of both the day before and the day after.

Table A-3: Statistics of monthly peaks greater than 50 cfs for 1936-2003.

	Mean (cfs)	Min (cfs)	Max (cfs)	S.D (cfs)	Skew	Kurtosis	Median (cfs)	75% (cfs)	90% (cfs)	95% (cfs)	99% (cfs)	count
January	714	54	5880	1136	2.7	10.9	224	758	1970	3050	5880	46
February	402	52	3450	629	3.5	16.5	166	380	1140	1730	3450	37
March	355	52	3340	635	3.4	15.1	112	245	740	2020	3340	38
April	130	51	337	109	0.9	2.5	63.5	195	337	337	337	8
May	56	56	56	0	-	-	56	56	56	56	56	1
June	159	51	300	83	0.5	2.2	146	172	300	300	300	8
July	279	51	3500	366	4.8	37.7	154	305	616	963	1470	171
August	324	51	3410	457	3.7	18.6	175	348	683	1130	2680	290
September	244	51	2390	340	3.8	21.1	128	241	455	934	2390	85
October	964	54	13200	2518	4.1	20.1	125	588	2020	4860	13200	30
November	314	58	1710	457	2.4	7.9	113	381	628	1710	1710	13
December	1010	51	6160	1469	2.3	8.3	390	1170	2640	6010	6160	38

The values in Table A-3 also indicate large variability of flow peak magnitude and strong seasonality. Note that peak magnitude has a maximum in October while there are significantly more peaks occurring in July and August compared to the rest of the months.

Although the Santa Cruz River is an ephemeral stream on the daily time scale, on the monthly time scale there are only 4 months that had zero flow over the entire analysis period. Therefore, although highly variable, the monthly flows can be analyzed using continuous-time-series statistics. Climatological statistics of monthly flow are presented in Figure A-6. This Figure is drawn in semi-logarithmic scale due to the existing 3-4 orders-of-magnitude difference in flow among the different months of the year. The Figure shows that the annual time series has a distinct seasonal signature. The monthly values are positively skewed with significant differences between the mean and the median. Worth noting also is that the monthly standard deviation is consistently higher than the monthly mean.

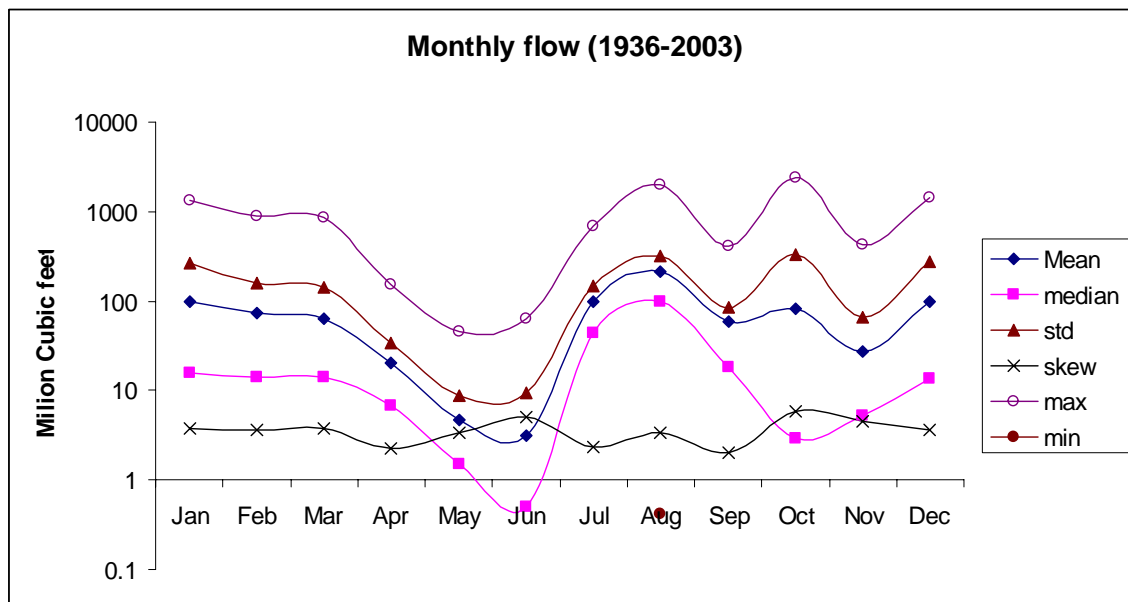


Figure A-6: Descriptive statistics for monthly flow at Nogales.

In Figure A-7 the monthly volumes were plotted as a time series for a given month and for the observation period (i.e., 1936-2003). The hydrographs of the different months have different appearances and magnitudes (e.g., compare June and July).

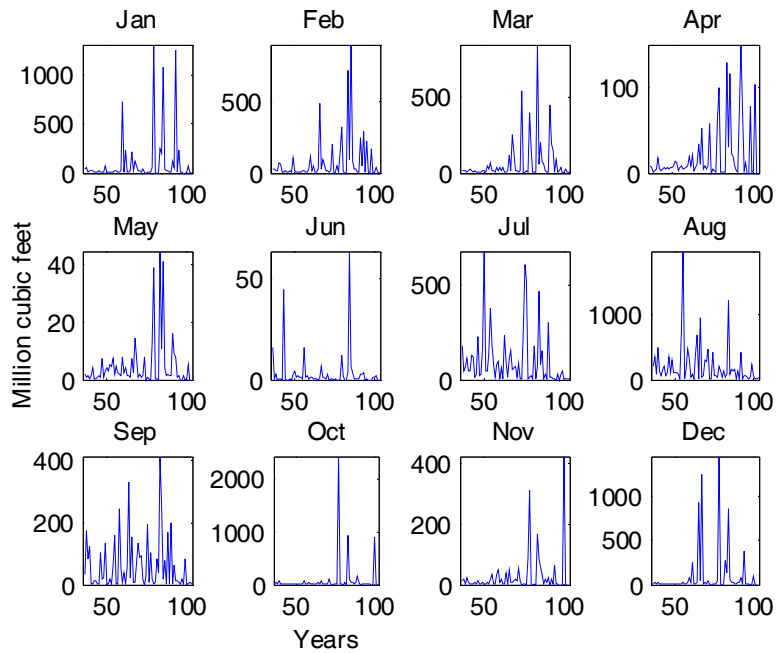


Figure A-7: Observed monthly flows for a given month and for the period 1935-2003.

The correlogram of the observed monthly volumes is presented in Figure A-8. It can be seen that even the lag-1 autocorrelation coefficient is low (about 0.35).

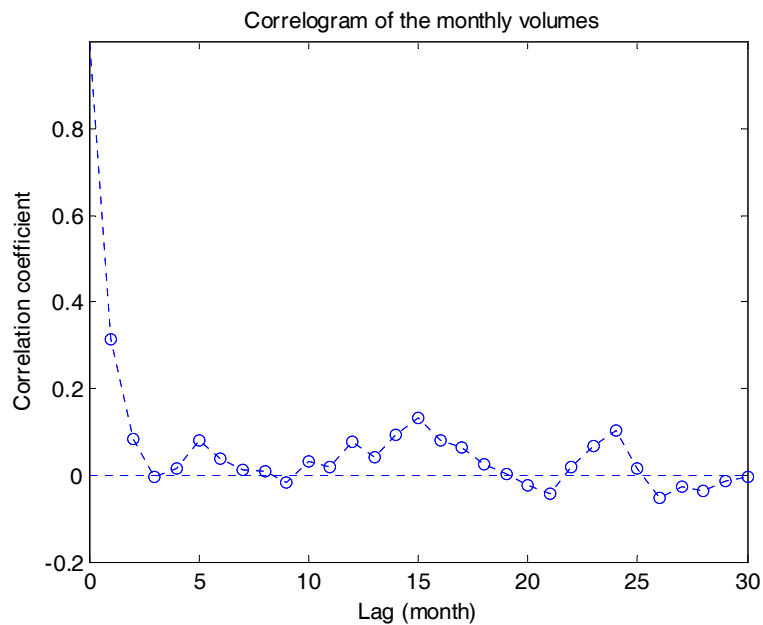


Figure A-8: Correlogram of the monthly volumes.

For the purpose of the current study and based on the above statistical results, we identify the seasons as follow: summer (July - September), fall (October), winter (November - March), and spring (April-June). The selection of these seasonal sub-groups is driven by a statistical grouping of the magnitude, frequency, and length of flow events. With regard to the annual flow volume, the wet seasons are summer and winter. Summer is characterized by flow events with a high frequency of occurrence, with relatively smaller magnitudes, and low baseflow. Winter has a lower frequency of occurrence of flow events, relatively high flow events, and longer lasting baseflow. Fall is a period with a low frequency of low flow events with an occasional occurrence of an extreme flow event (flood) caused by tropical storm influence. Spring is dominated by drought with rare low flow events.

A.4 Analysis of long-term trends in the flow record

In order to produce statistical parameters that are representative of the natural flow, the data is required to be statistically stationary in time. That is, to study the underlying day-to-day flow variability, any trends, abrupt shifts, and seasonality in the data must be estimated and removed. Furthermore, to be able to generate future likely flow scenarios, such longer-term properties of the data must also be estimated for the future period of interest. In Figure A-9, the five-year moving average of the July-August count of the number of peaks above a given threshold magnitude is plotted against the actual years for a number of such threshold magnitudes. It is clearly seen that the frequency of occurrence is showing a general progressive decline for all the thresholds except for the highest ones for which the number of peaks decreases to very small values, infusing significant sampling uncertainty in the results.

In Figure A-10 the same trend is observed for the monthly flow magnitude in July - August. In this Figure, the wet and dry year cycles have large amplitude and a trend is more concealed when compared to the results of Figure A-9. The fact that the trend is less significant for the larger thresholds might be because of upstream flow modifications that are eliminating many of the smaller streamflow events. For example, a summer over-exploitation of the upstream aquifer might increase the recharge capacity of the stream, thus reducing downstream flow. Such a trend is not evident in the January-February time series results shown in Figures A-11 and A-12. The behavior of both (a) the number of peak occurrence and (b) the peak magnitude has a cyclic appearance in winter, which might be associated with climate signals for this season.

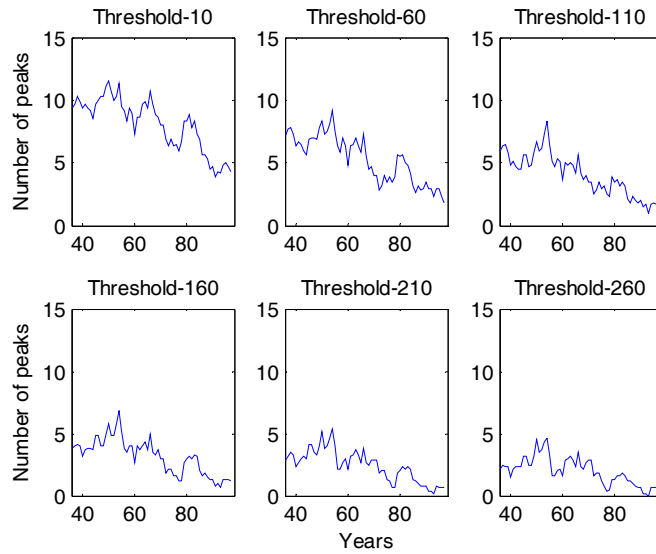


Figure A-9: Five-year moving average of the number of July-August peaks above a given mean daily flow (cfs) threshold. Thresholds from 10 cfs to 260 cfs are considered.

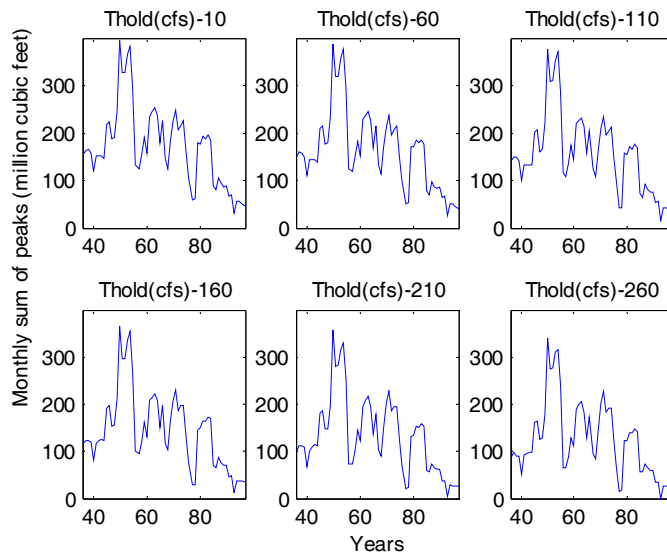


Figure A-10: Five-year moving average of the total monthly volumes of peak mean daily flow (million cubic feet) during July-August above a mean daily flow (cfs) threshold.

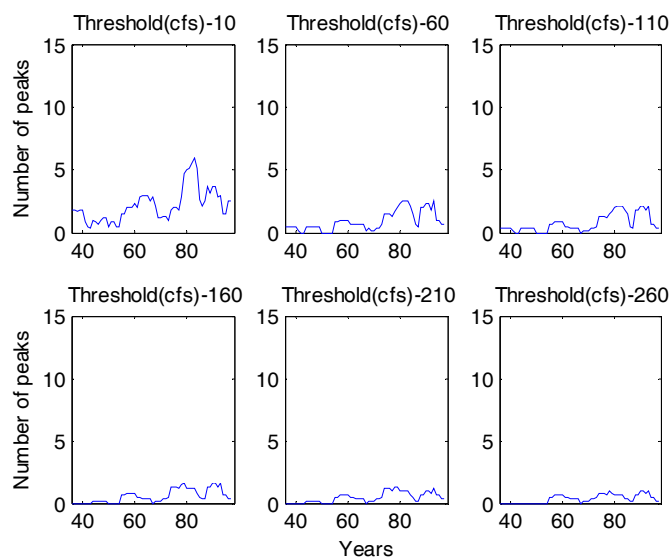


Figure A-11: As in Figure A-9 but for January and February.

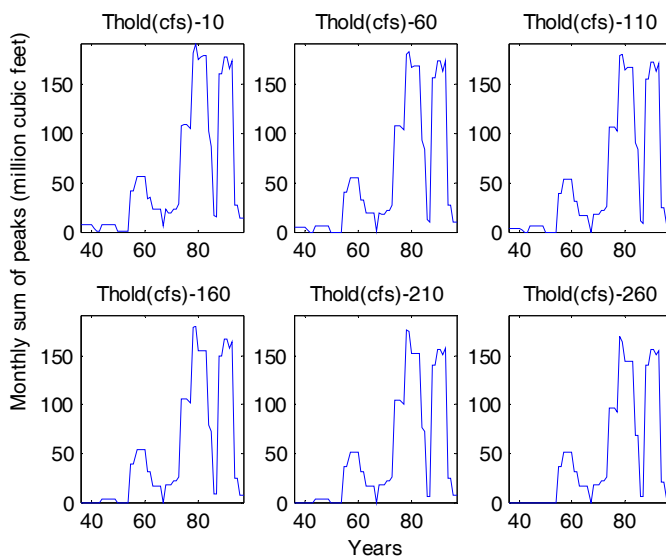


Figure A-12: As in Figure A-10 but for January and February.

For further exploration of this apparent summer trend we compared this record with the daily precipitation records for Nogales. In Figure A-13 the 5-year moving average of the number of peaks for the daily streamflow and the number of daily precipitation occurrences during summer are shown. It can be seen that both records are showing a decline trend in the frequency of occurrences for both precipitation and streamflow.

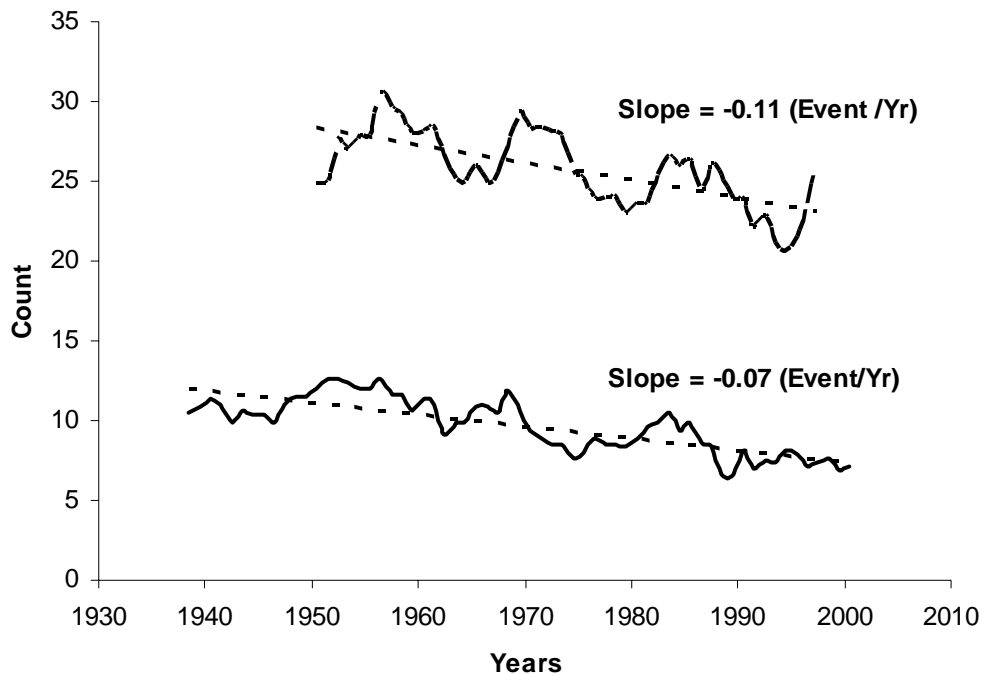


Figure A-13: The Nogales summer (July-August) 5-year moving average of the count of the number of peak flows (solid line) and of the number of daily precipitation events (dashed line). The slopes of a linear regression fit are also indicated in each case.

In Figure A-14, a 5-year moving average for the total summer precipitation and streamflow are presented. Although the streamflow values have high variability and few very wet summers were observed in the early 50's, the linear regression fitted to the record indicates a decline trend for the period of the record. An analogous trend is not apparent in the daily precipitation record. It must be noted, and it is further explored in Chapter B, that the precipitation record at the Nogales site went through a change in the sampling interval in the mid 70's. This may influence the results shown in Figures A-13 and A-14, and, therefore, the trend in the precipitation record requires further analysis.

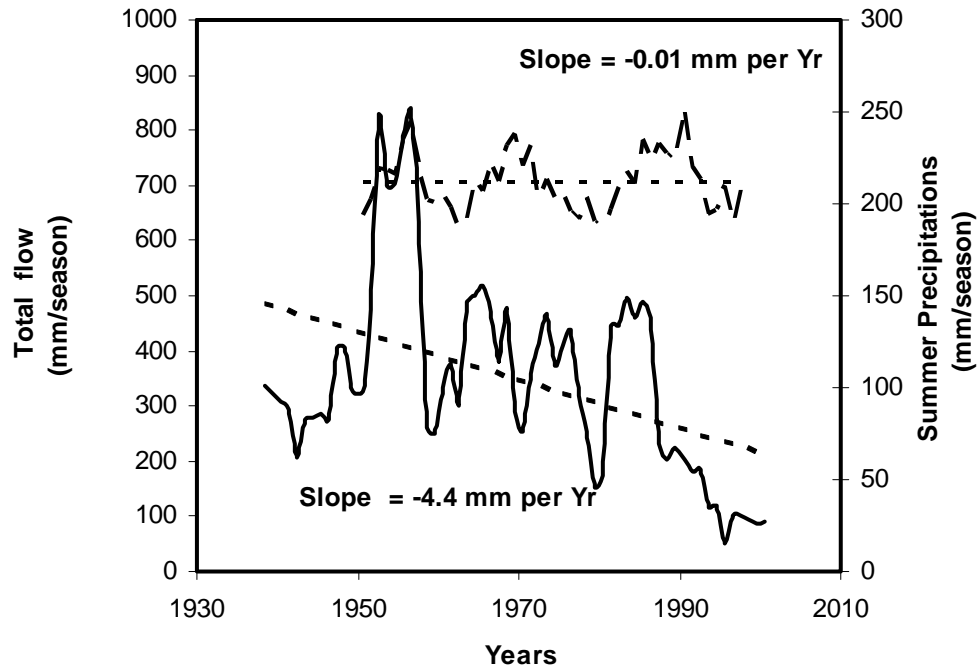


Figure A-14: The Nogales summer (July-August) 5-year moving average of cumulative flow (solid line) in mm/season assuming that the contributing area is 10 square miles. Analogous results for the seasonal cumulative precipitation (dashed line) are shown. The slopes of a linear regression fit are also indicated in each case.

A.4.1 Analysis of the Summer Flow Data for the Lochiel Site

The USGS Lochiel streamflow gauge is located in the headwaters of the Santa Cruz River and drains an area of 82.2 square miles (Figure A-1). The gauge record represents natural flow with limited effects of agriculture, and it spans the period 10/1/1948 - 30/9/1996 with daily resolution. This area is believed to experience the same climatic regime as the USGS Nogales gauge site, and, if the trend in the flows that was detected for the Nogales gauge is due to climatic forcing, it should be present in the record of the Lochiel gauge as well (unless in this case too there is significant anthropogenic influence in low flows). Daily cross-correlation analysis with the USGS Nogales gauge flow gave a lag-0 cross-correlation of 0.68, indicating that the same atmospheric forcing affects both sites. The lag-1 cross-correlation of 0.33 (USGS Nogales gauge lagging) indicates that there is little flow from Lochiel that finds its way to the USGS Nogales gauge site.

The same analysis as presented above for the USGS Nogales gauge site record was conducted for the Lochiel gauge time series, using smaller flow thresholds to accommodate the lower flows. The frequency of occurrence of peaks for thresholds greater than the threshold of 5 cfs, yields small numbers of peaks in summer and cannot be trusted. A trend may exist in the summer for peaks greater than 5 cfs as indicated in the first panels of Figures A-15 and A-16. At this time it is not known whether this trend for low thresholds is a result of the limited agricultural activities in the area (see field trip

summary in Annex B) or whether other climatic effects are important. The January-February plots (Figures A-17 and A-18) show the same features as observed in the USGS Nogales gauge site analysis with no clear record trends.

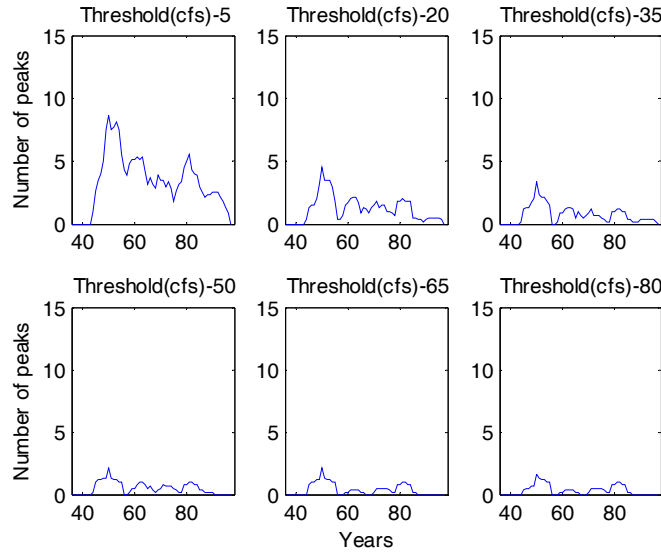


Figure A-15: As in Figure A-9 but for the Lochiel gauge record.

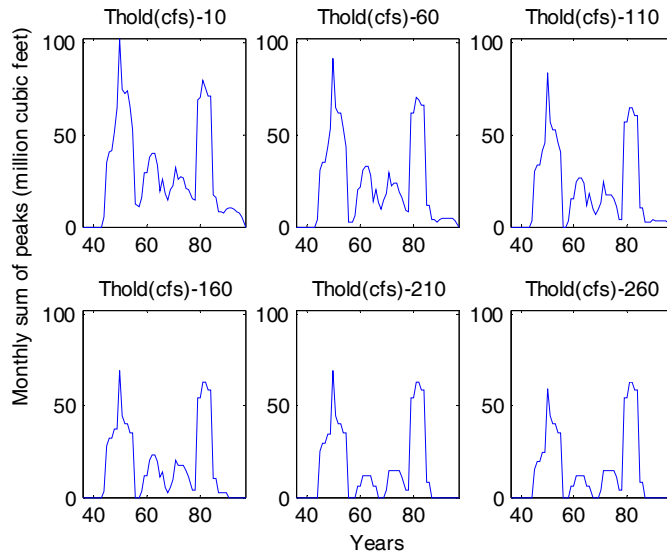


Figure A-16: As in Figure A-10 but for the Lochiel gauge record.

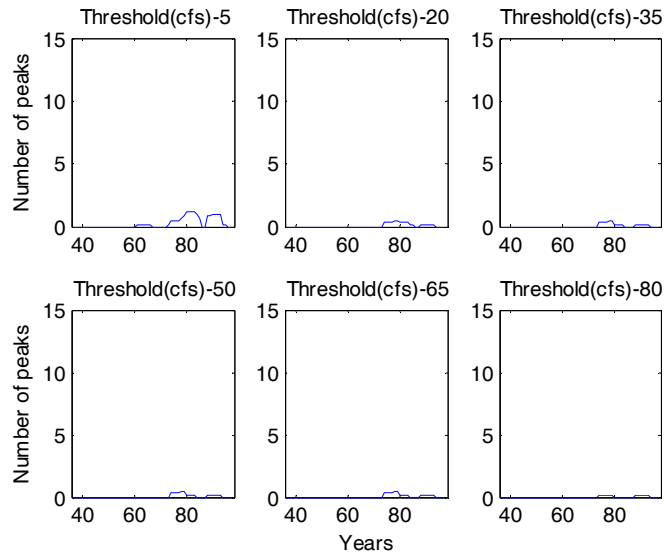


Figure A-17: As in Figure A-11 but for the Lochiel gauge record.

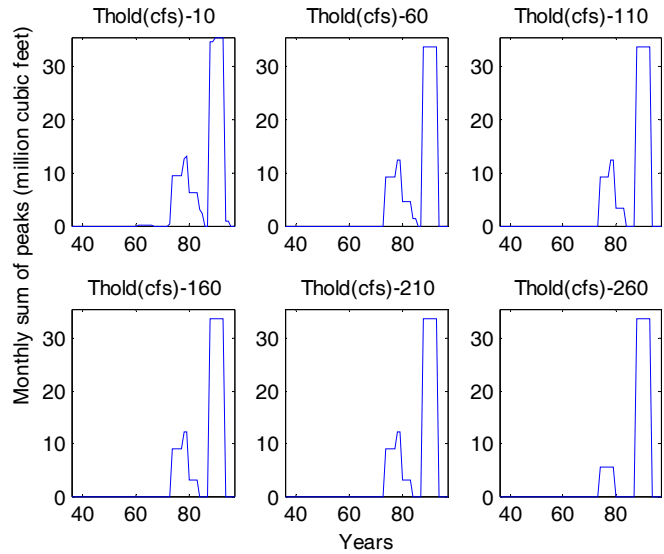


Figure A-18: As in Figure A-12 but for the Lochiel gauge record.

Additional daily records from the stations at Laveen and Tucson on the Santa Cruz River, downstream of the Nogales gauge, were examined as well for summer trends. The Tucson gauge data are missing during the 80's and 90's. The analysis is carried out again with respect to the number of peaks and the total summer flow. Figure A-19 shows that the trend is apparent for the number of occurrences from the mid 50's. A decline trend is

also seen for the total flow although the large inter-annual variability makes this trend less obvious. In Figure A-19, the total summer flow is normalized by the maximum value for each time series shown.

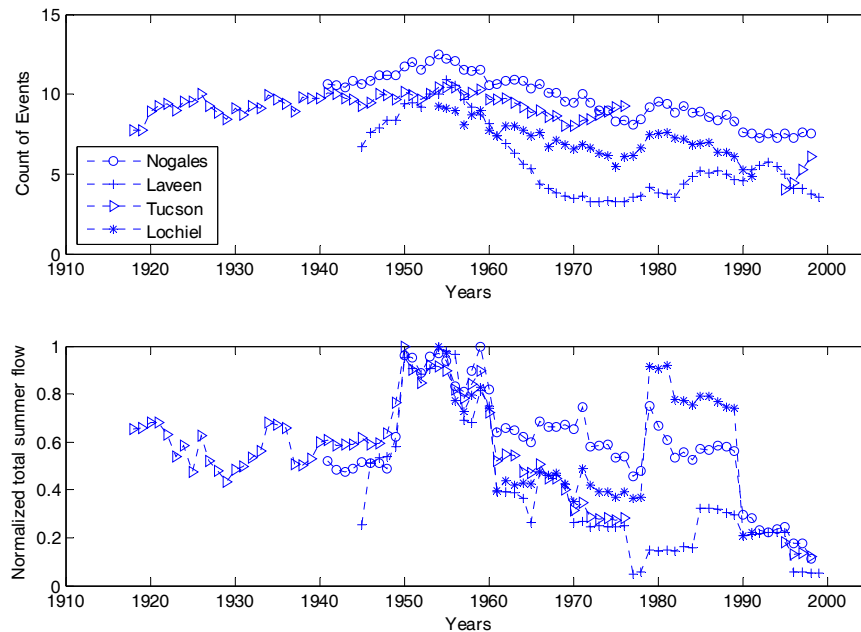


Figure A-19: Time series of the 10-year moving average of summer flow (July-August) at four gauging sites. The upper panel is for the number of events and the lower panel is for the normalized total seasonal flow volume.

Such trends in peak magnitude and number of peak occurrence have been documented by *Pool and Coes (1999)* for the Upper San Pedro Basin. In their study, precipitation records from four stations show a slight decline trend in the season totals. Moreover they have reported a clear indication of summer total flow decrease from 1935 to the 1990's. They further claim that the amount of precipitation that transforms into flow at the channel is also declining for the summer season. Such a trend was not observed for the winter which might indicate that this trend is associated with changing precipitation patterns rather than land use/cover changes and channel improvement. The changes in precipitation can be attributed to decreases in storm duration, spatial scale, and/or magnitude of summer precipitation. The change in precipitation pattern might also be related to the reported land cover changes in the San Pedro basin that have occurred since the 70s (e.g., *Kepner 1999*).

A.5 Wavelet analysis of streamflow record at Nogales

Additional insight about the character of global and local variability of the streamflow time series may be obtained by using wavelet analysis (e.g., *Saco and Kumar 2000*). Denoting the streamflow as a function of time by $q(t)$ and the wavelet by $\psi(t)$, we define the continuous wavelet coefficients of the streamflow signal from:

$$C(a,b) = \int_R q(t) \frac{1}{\sqrt{a}} \psi\left(\frac{t-b}{a}\right) dt; a > 0 \quad (\text{A.2})$$

where a is a scaling parameter (scale), b is a location or translation parameter (time). Large absolute values of the coefficients signify strong resemblance of the streamflow signal with a scaled and translated version of the wavelet. The coefficients are displayed in a scale versus time plot in Figure A-20 using the streamflow mean daily flow time series from 1935 through 2003. The colorbar indicates the absolute value of the coefficients $C(a,b)$ for each scale a and time b . The scale parameter a varied from two days to ten years in monthly intervals. Daubechies' fourth-order asymmetric and orthonormal wavelet was used to define the function $\psi(t)$ in Figure A-20. It is noted that there is a correspondence between wavelet scales and frequency, with low scales a corresponding to high frequency fluctuations and vice versa.

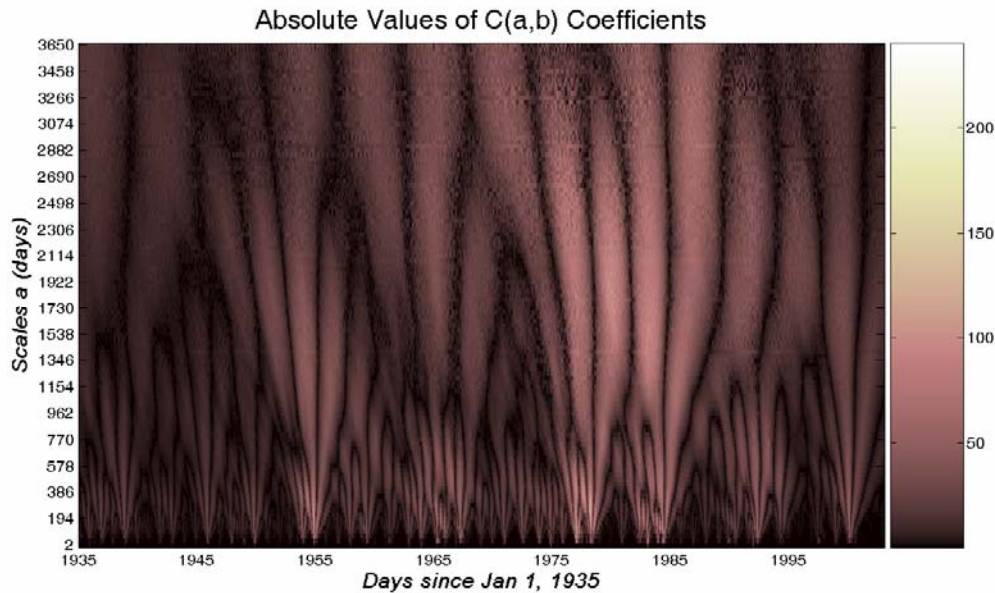


Figure A-20: Wavelet coefficient magnitude as a function of time and scale.

The results show a range of scales that is exhibited by streamflow throughout the period of record. Substantial periodicity exists on decadal time scales (scale of about 3650 days) throughout the record but particularly from the 50s to the 90s. The 70s and 80s also exhibit a continuum of scales in streamflow from days to decades (high coefficient values throughout). Pronounced daily, monthly, annual and biennial time scales are shown for the mid 50s, mid 60s, late 70s, early 80s, early 90s and near 2000. The scale-time plot

shows that the decadal periodicity is most regular, while for shorter scales and in several epochs the signal appears self similar, implying that the time series of streamflow may possess fractal properties. The existence of scales of variability of several years and of several decades suggests correlative analysis with climatic forcing such as El Niño Southern Oscillation (ENSO) and Pacific Decadal Oscillation (PDO). These analyses are described next.

A.6 Precipitation in relation to large-scale climatic indices

A composite precipitation dataset for Nogales was prepared from the “Old Nogales” gauge covering 1914-52 (available from <http://www.wrcc.dri.edu>), and the gauge near the International Wastewater Treatment Plant (IWTP) for 1953-2000. Winter precipitation comes almost entirely from frontal storms approaching from the west, dry season rainfall comes both from winter-type systems and from early monsoon episodes, summer precipitation is primarily of monsoonal origin with some contribution from remnants of Pacific tropical storms, and October has some contribution from all three sources and includes instances of heavy rainfall associated with tropical storm activity. The NINO3 index [area-average sea surface temperature (SST) anomaly over the region 150-90°W, 5°S-5°N; data from *Kaplan et al., 1997*)] was used to characterize El Niño activity. Decadal-scale Pacific climate variability was characterized by the Pacific Decadal Oscillation (PDO) index (*Mantua et al., 1997*). This index characterizes sea surface temperature fluctuations in the central North Pacific (cool SSTs give high values of the PDO index), and is an indicator of the strength of the winter westerlies and storm track activity in that region. High values of the “PDO” are associated with generally higher precipitation across the southwestern US in the modern record. Both the NINO3 and PDO indices were composited seasonally as described above.

Correlations between seasonal Nogales precipitation and the NINO3 and PDO indices are shown in Table A-4. These results show that when the data are treated on a season-by-season basis, only the El Niño signal has any substantial relationship with Nogales precipitation, and this only for winter. As seen in Figure A-21, the relationship between El Niño and Nogales precipitation is typical of such relationships in the western US (e.g., *Redmond and Koch, 1991*) and shows increasing scatter with increasing NINO3 SST. The lack of a strong relationship between El Niño variability and regional precipitation in other seasons is in agreement with earlier analyses (e.g., *Webb and Bettencourt, 1990*).

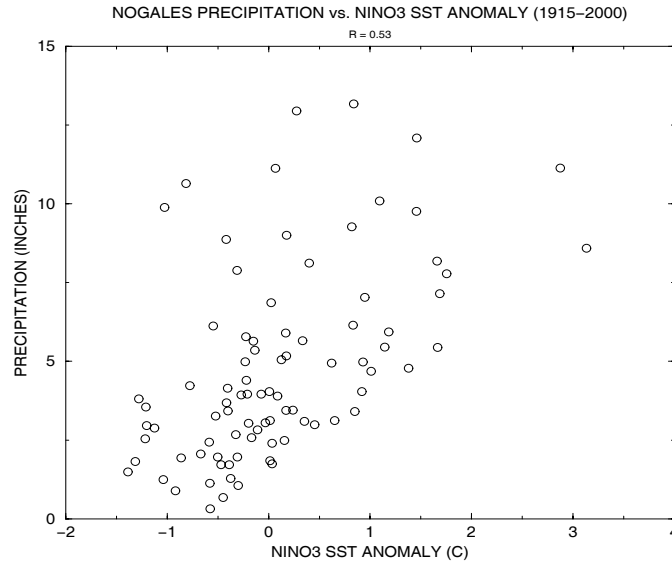


Figure A-21: Scatter plot of Nogales winter precipitation vs. NINO3 SST anomaly, 1914-1999.

The well known relationship between Southwest rainfall and the PDO (e.g., *Cayan et al., 1998*) becomes apparent when the precipitation records are smoothed (Figure A-22), though there is little to distinguish effects apparently related to the PDO or with the smoothed El Niño signal (El Niño years are also associated with storminess and cool North Pacific SSTs). Therefore, it is not possible to clearly distinguish independent effects from the PDO or El Niño (see *Zhang et al., 1997*), especially with a record this short in comparison to the time scales of interest (multi-decadal).

Table A-4: Correlations with Nogales precipitation, 1914-2000.

	NINO3	PDO	ARIZ. DIV. 7
WINTER	0.53	0.27	0.94
DRY	0.11	0.22	0.70
SUMMER	-0.06	0.09	0.53
OCTOBER	-0.03	-0.09	0.87

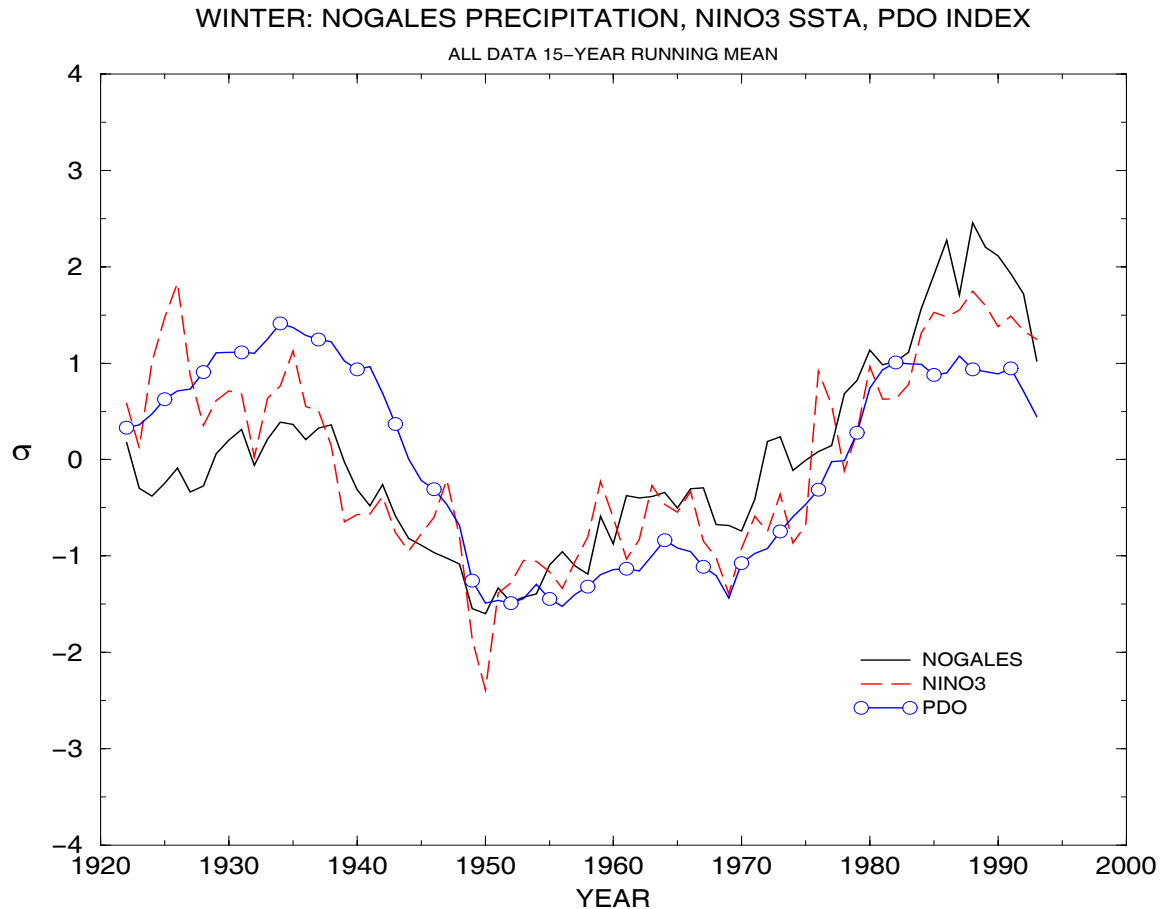


Figure A-22: 15-year running mean Nogales precipitation (solid), NINO3 SST (dashed) anomaly, and PDO index (solid with circles). All data are standardized.

A statistical analysis was conducted in which the effects of El Niño on the Nogales winter precipitation record were removed using linear regression, and residuals from that analysis were then compared with the PDO record. The results showed that the PDO explained almost none of the residual record, reinforcing the difficulty in assessing clearly independent effects of decadal variability in El Niño and the PDO.

Also shown in Table A-4 are correlations between the precipitation average for Arizona Climate Division 7 (most of southernmost Arizona) and Nogales precipitation, again for the seasons defined earlier. These correlations emphasize how changes in the spatial scales of precipitation systems alter correlations between point measurements and large-scale area averages in the Southwest, as demonstrated in the research of R. Webb and K. Wolter (NOAA Climate Diagnostics Center, Boulder; as described in the November 2004 “END Insight Newsletter” produced by the CLIMAS project at the University of Arizona). The weather systems that bring winter precipitation are large, so that a point measurements agree relatively well with large-scale averages (and vice versa), e.g., the correlation between winter Nogales precipitation and the Climate Division 7 average is 0.94. In contrast, the weather systems that bring summer precipitation are much smaller (or at least the individual storm cells that bring rainfall are much smaller), so that seasonal precipitation averages from an individual station are much less representative of

large-scale area averages during summer than during winter (e.g., the correlation between Nogales and Arizona Division 7 precipitation is only 0.53 in summer). Interestingly however, this seasonal difference in statistical character has little effect on the seasonally stratified correlations with the PDO and El Niño (i.e. the correlations for Division 7 show a pattern similar to that shown in Table A-4).

The suggestion that variability in the tropical Pacific has an effect on southern Arizona precipitation is clear from the results above, and this can be seen in proxy records as well. Figure A-23 (after *Graham, 2004*) compares a tree-ring derived reconstruction of regionally-averaged moisture availability for the Southwest (*Cook, 2000*) with a detrended stable isotope ($\delta^{18}\text{O}$) record from an ice core taken from the Quelccaya ice cap in the tropical Andes (*Thompson et al., 1984*). Fluctuations in ice cap $\delta^{18}\text{O}$ are thought to reflect changes in tropical SSTs (*Bradley et al., 2003; Graham, 2004*). The correspondence between the records is compelling and emphasizes the role of tropical Pacific sea surface temperatures in modulating centennial variability in winter precipitation in the Southwest (a signal shared by the reconstructed data from the Nogales region, not shown).

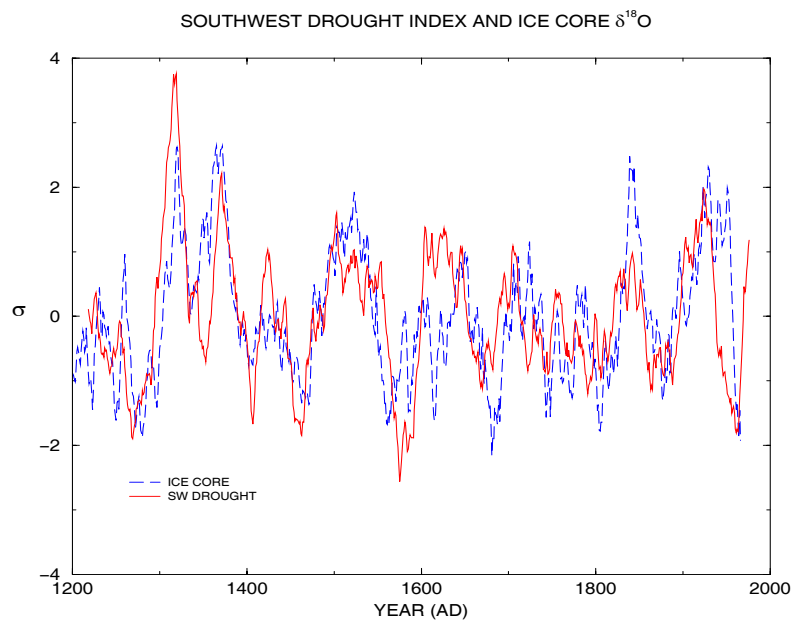


Figure A-23: Comparison of the Southwest Drought Index [reconstructed moisture availability in the Southwest (associated with cool season precipitation)] with $\delta^{18}\text{O}$ from the Quelccaya ice cap in the Peruvian Andes (thought to reflect changing tropical Pacific SSTs).

Chapter B

Stochastic Streamflow Modeling

B.1 Introduction

The goal in this Chapter is to develop a stochastic model that generates equally likely streamflow scenarios that preserve characteristics of the observed streamflow time series at the USGS Nogales gauge site. The model is designed to reproduce the properties: frequency of occurrence of a flow event, event inter-arrival period, event duration, event volume, event peak flow, and the monthly flow volumes. It is thought that for groundwater recharge applications the small flow events can be considered as effective events in the sense that for such a flow regime there is no spill of streamflow from the southern aquifer domain as defined by the Arizona Department of Water Resources (AZDWR) groundwater model. The magnitude of these events depends on the available storage of the regional groundwater microbasins, and, in general, it is estimated that flows lower than 100 cfs comprise these events (*Gretchen Erwin personal communication*).

An intuitive approach one might take to generate such a model is to analyze the streamflow record and extract meaningful descriptors, and then develop a re-sampling technique that preserves these descriptors. Such an approach is presented in Chapter C with the use of an Autoregressive Moving Average (ARMA(1,1)) model for the generation of monthly flows. In this Chapter however we present the development of a more physically based modeling system, which first generates synthetic precipitation for a site and then uses the generated precipitation to force a conceptual parametric hydrologic model that converts the precipitation into streamflow at Nogales.

The motivation and advantages of developing synthetic streamflow from precipitation are: (a) precipitation is dominated by climatic signals and is less prone to be affected locally by human activity and therefore might be more reliable for future projections; (b) precipitation has a better connection to the paleo-climatic record that is planned to be used to infer long term trends; (c) precipitation data are collected by direct measurements, as opposed to flow which requires a rating curve to convert the measured head to discharge values; and (d) the precipitation-to-flow model parameters may be used to ask “what if” questions regarding any upstream anthropogenic future activity.

Such an approach is plausible in regions for which precipitation is the dominant forcing of the streamflow, and clear response of the flow to the precipitation can be discerned from the available records. The major concerns and disadvantages for such an approach are: (a) the ability to represent areal precipitation from one or more point measurements; and (b) the identifiability from observed records of the parameters and structure of the required transformation of precipitation into streamflow. It is important to note that these concerns introduce new sources of uncertainty for the synthetic flow realizations.

The only precipitation data available for the basin upstream of the USGS Nogales gauge site are monthly values during the period 1968-1981 at San Lazaro in Mexico. This dataset does not have the record length and temporal resolution required for the model development. Precipitation data on the United States side include hourly data sets from two precipitation gauges in the Nogales area, which are located a few miles north of the USGS Nogales gauge site (Figure A-1). These are the gauges closest to the flow gauge site with a sufficiently long record. Use of these gauges that are located north of the USGS Nogales gauge carries the assumption that the long term statistics of precipitation at this site are representative of the precipitation characteristics that force the flow observed at the USGS Nogales gauge site.

Although the precipitation gauges located in the valley (Figure A-1) might not be representative of the orographic precipitation at the higher elevations, we believe that these gauges provide valuable information because the forcing that contributes to the flow at the USGS Nogales gauge is local and close to the gauge (see the analyses of the Lochiel gauge below). It also appears that the physical setting (e.g., elevation, aspect, land cover) is comparable. We further evaluate this statement in Section B.2.2 with the aid of an atmospheric mesoscale model to investigate the relationships between the precipitation record and the contributing basin area to the Nogales stream gauge.

B.2.1 Precipitation Analyses

Hourly precipitation data is compiled and published by the National Climatic Data Center and for the purposes of this project was acquired from EarthInfo Inc. The precipitation record consists of cumulative hourly data for the period between 7/1/1948 to 12/31/1992. This time series was compiled from two gauges. The first (W110:55, N31:21) has a record from 7/1/1948 to 12/31/1983, while the second located at the Nogales International Wastewater Treatment Plant (W110:57, N31:25) has a record from 1/8/1983-12/31/1992 (Figure A-1). Following the discussion in Chapter A, the record was divided into four seasons: summer (July - September), fall (October), winter (November - March), and spring (April-June).

To better understand the time scale of the precipitation events in the region, in Figure B-1, the duration of precipitation events, as interpreted from the hourly record, is plotted as a function of the summer and winter seasons. It can be seen that in both seasons most of the events last less than 2 hours. For about 70% of the events, rain was recorded within 2 hours. Such findings demonstrate the very short regional time scales of the precipitation events, and the need to conduct the precipitation analysis with a fine temporal resolution (i.e., hourly time steps).

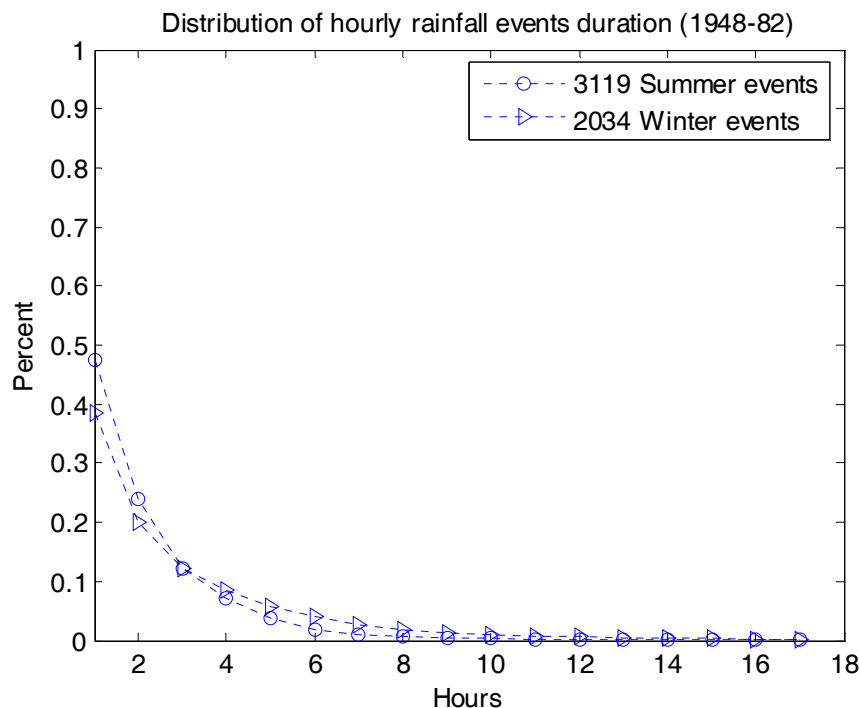


Figure B-1: Frequency distribution of the duration of summer and winter precipitation events at Nogales.

Based on the monthly flow analysis presented in Chapter A, the wet seasons (i.e., the summer and the winter) exhibit large inter-annual variability. Therefore an attempt to develop a synthetic model using sample statistics that include all the years from these wet seasons would average very different years and would compromise the resampling of the extremes (both dry and wet years). Instead, in this study, the summer and the winter seasons were further categorized by relatively wet, medium (normal) and dry years. These categories are based on the seasonal flow. A wet winter (summer) is a year with total seasonal mean daily flow that exceeds 9000 (12000) $\text{ft}^3 \text{s}^{-1}$. A dry winter (summer) is a year in which the total seasonal flow is below 500 (5000) $\text{ft}^3 \text{s}^{-1}$. The years of medium flow are the years in which the seasonal total flow is in between the threshold defined for the wet and the dry years. Such categorization implies for both seasons that about 20%, 40% and 40% of the years are wet, medium, and dry, respectively. The selection of these thresholds was subjective and aimed to create three sub-groups that are distinct and with sufficient sample size that would enable reasonable inference from statistical analysis.

B.2.2 Atmospheric Mesoscale Modeling

The MM5 model, a mesoscale model that simulates atmospheric processes, was used to explore the precipitation spatial variability and the areal relationships between the rain-gauge precipitation and the mean areal precipitation over the drainage area upstream of the Nogales stream gauge. The MM5 has been developed by the Pennsylvania State University and the National Center for Atmospheric Research (*Dubhia, 1993*). The domain that was used for the simulations is about 300,000 km² with a 6 km² resolution and the domain was centered at the area of interest. For model initialization and boundary fields, the ETA reanalysis dataset from the National Center for Environmental Prediction was used [<http://wwwt.emc.ncep.noaa.gov/>]. This dataset is provided with a 6-hour temporal resolution and 32-km² spatial resolution.

The model was constructed to simulate the atmospheric processes for three selected Januaries (1979, 1991 and 1992). These months, each containing two distinct storm events, offer typical winter storms with a variety of precipitation patterns and intensity and with south to south west wind direction that transports humidity from the Pacific shore of Baja California. The current model setup has been found suitable to describe the spatial variability of precipitation due to orographic effects for winter frontal events (*Wang and Georgakakos, 2005*). The model ability to simulate the precipitation areal distribution during the convective summer monsoon is modest.

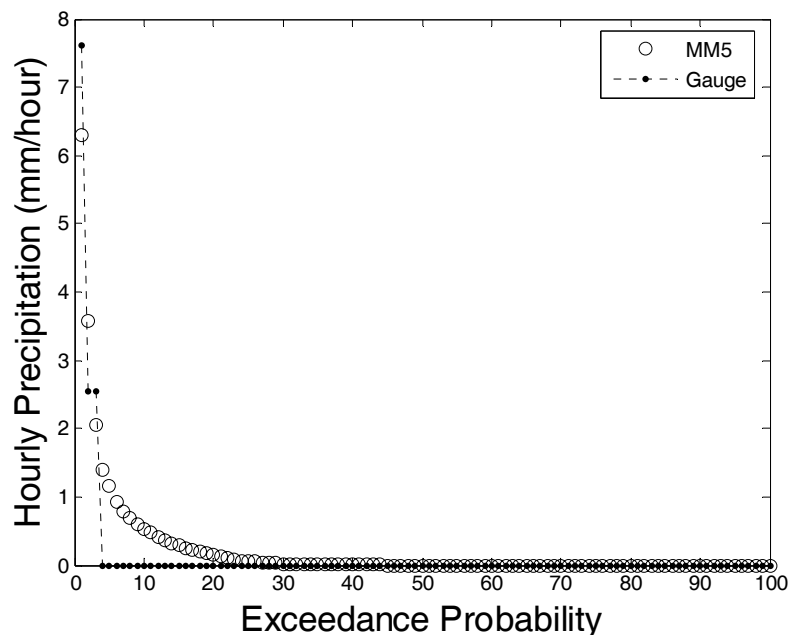


Figure B-2: A comparison of the precipitation exceedance probability between the Nogales gauge precipitation and the corresponding mean areal precipitation calculated for the three Januaries.

The exceedance probability of the simulated hourly mean areal precipitation during these three months is compared with the corresponding gauge record in Figure B-2. It can be

seen that during the simulated months about 95% of the events had rain that is smaller than 0.1 inch (2.54 mm) which is the gauge measurement threshold (trace amount). The model and the gauge curves agree reasonably well for precipitation greater than the gauge trace amount.

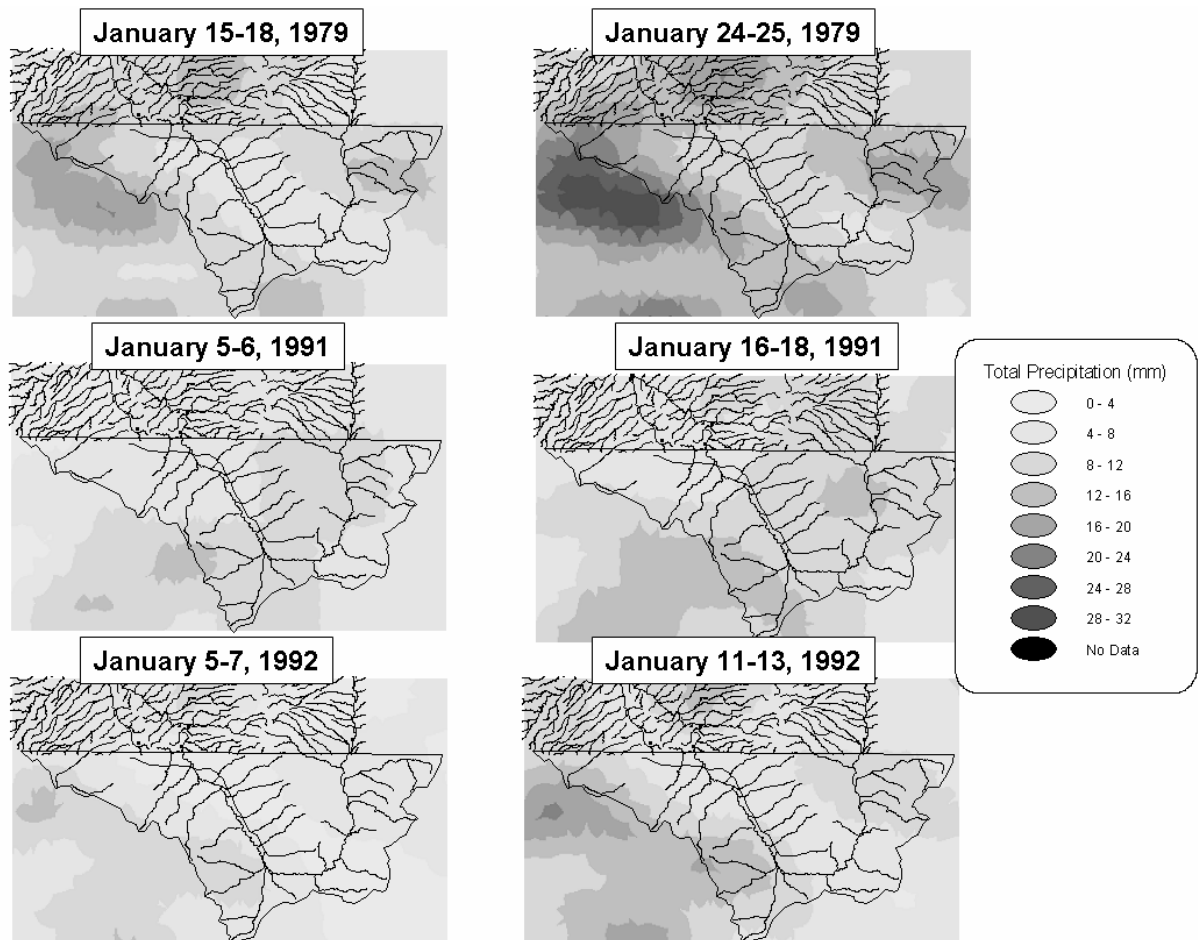


Figure B-3: The cumulative precipitation (mm) for six different storms as simulated by the MM5 Mesoscale atmospheric model.

In Figure B-3 the areal distribution of total precipitation for the 6 events is shown in gray scale. For all the events, the western mountain ridge of the drainage area is the rainiest area. Humid air coming from the west and southwest produces higher precipitation at high elevations that occasionally (during larger storms) drains into the Santa Cruz River (e.g. January 1979). However, for this case, the majority of precipitation occurs outside the basin drainage area on the western slopes which feed a tributary (i.e., Nogales Wash) that joins the Santa Cruz River main stem downstream of the Nogales gauge. Another relatively wet area is the eastern part of the basin, in the vicinity of the river crossing into Mexico. Earlier analysis in Chapter A indicates that much of that precipitation does not flow through the Nogales gauge. The majority of the basin area (especially near the

Nogales gauge) receives rain volumes that are similar to those experienced by the raingauges used in this analysis.

B.2.3 Stochastic Precipitation Model Development

The stochastic precipitation model is developed as a point process model of precipitation clusters and hourly precipitation amounts. A pivotal decision in the development of such model is the definition of rainfall clusters. Storms tend to arrive in clusters as a response to transient synoptic scale atmospheric disturbances. Each synoptic event might produce multiple intervals of precipitation with hours or days of no precipitation in between. One approach to separate the independent events is based on the identification of the independent larger-scale atmospheric disturbances. This approach requires the creation of a long-term meteorological synoptic database and it is difficult to apply for summer convective events. An alternative approach is based on statistical analysis and identifies the minimum inter-arrival time that yields clusters that are statistically independent. This later approach is pursued in the following.

Restrepo-Posada and Eagleson (1982) proposed a statistical test for independence that is based on the assumption that the cluster arrivals constitute a Poisson stochastic process. That is, it is hypothesized that there is random arrival of instantaneous events with an exponential distribution of inter-arrival periods. An empirical test to examine if a sample can be assumed to have the properties of a Poisson population is that which determines whether the mean and the standard deviation or inter-arrival periods are equal (that is, coefficient of variation (CV) equal to 1). This test essentially assumes exponential distribution of inter-arrival periods. Therefore, a statistical test may be constructed for the precipitation time series that identifies the minimum precipitation inter-arrival period that yields $CV \sim 1$. In Figure B-4, such analysis is presented for the four seasons. It can be seen that increasing the minimum inter-arrival period results in decreasing CV of the inter-arrival time distribution. It can also be seen that the CV approaches 1 for an interval of 2 days for the summer spring and fall, while for the winter the CV approaches 1 for an interval of 6 days. The apparent lack of a decline trend in CV with the increase of time intervals (greater than 4 days) for the spring and the fall is because of the significant decrease of the number of clusters in these seasons. Further analyses of the wet seasons' three yearly (Figures B-5 and B-6), shows that the wet winter yields 7 days of minimum inter-arrival time, and for the summer, the three categories have a minimum inter-arrival time of about 2 days.

These time values are within the range of minimum inter-arrival values reported in *Restrepo-Posada and Eagleson (1982)* for Arizona rainfall. The seasonal differences in the duration of inter-arrival periods also reflect the different temporal scales of storms, convective versus frontal in summer and winter, respectively.

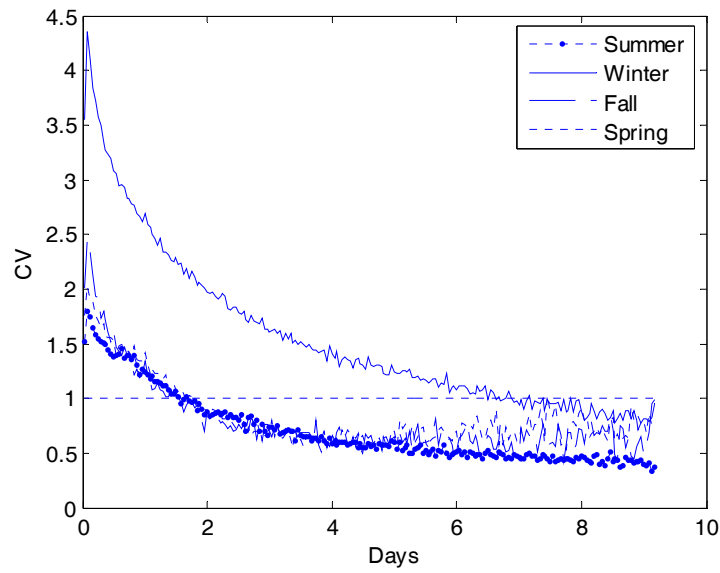


Figure B-4: Testing the minimum precipitation inter-arrival period that yields statistically independent clusters (*Restrepo-Posada and Eagleson, 1982*). The coefficient of variation (CV) of the precipitation inter-arrival periods is plotted as a function of the minimum precipitation inter-arrival period, for each season.

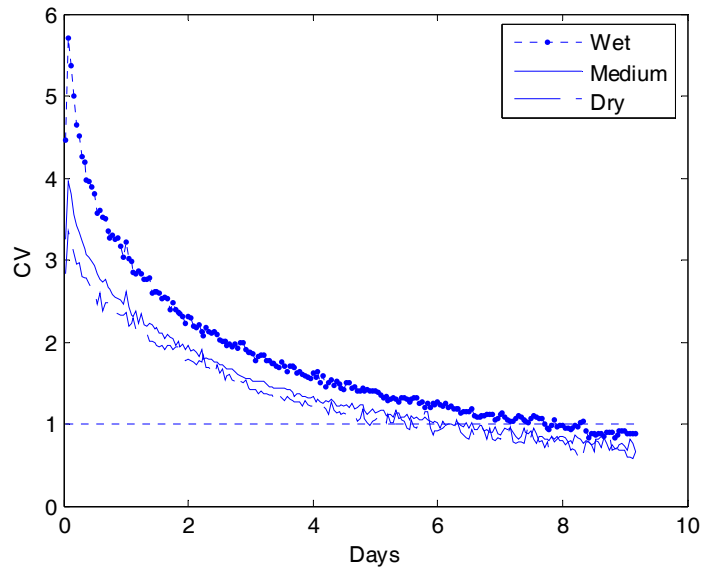


Figure B-5: the same as B-4 but for the winter wet, medium, and dry years.

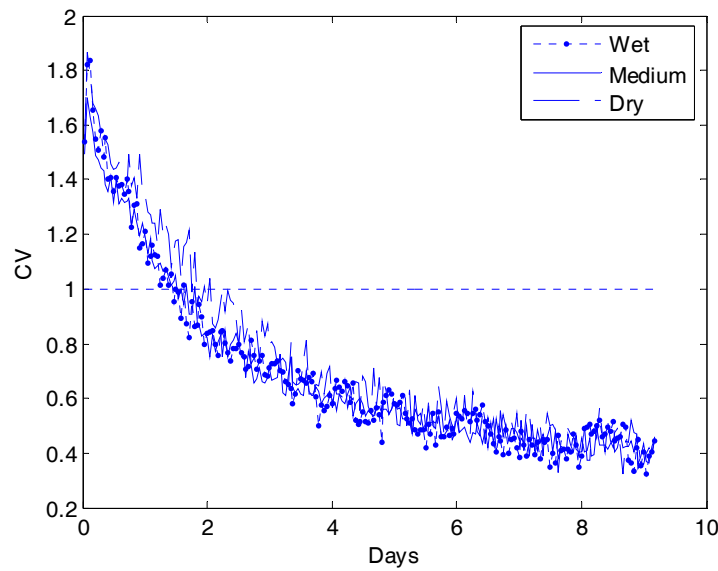


Figure B-6: The same as B-4 but for the summer wet, medium, and dry years.

Using this minimum inter-arrival time criterion it is feasible now to identify precipitation clusters in the different seasons. To develop the synthetic generation model for precipitation we derived frequency distributions from the precipitation time series for the following random variables: (a) the inter-arrival periods of a cluster (using the minimum inter-arrival time described above); (b) the time duration of a cluster; and (c) the magnitude of an hourly precipitation event. In addition, we estimated from the data the chance for precipitation to occur within a cluster. It is reasonable to assume that the indicated random variables (*a*, *b*, and *c*) are independent.

The seasonal sample histograms and box-plots of these three random variables (i.e., *a*, *b* and *c*) are presented in Figures B-7, B-8, and B-9, respectively. In these Figures the winter and summer results are presented as aggregates of the three categories (wet, medium and dry). In Figures B-10, B-11, and B-12 these sample histograms and box-plots are presented for each of the three categories of winter and in Figures B-13, B-14, and B-15 they are presented for the summer categories.

The histograms in these Figures were divided into equal-width bins and the number of bins is the integer that is equal or greater than the \log_2 of the sample size (as recommended by *Hirsch et al., 1993*). The box-plots provide information on the statistical characteristics of the sample in a concise manner. The box edges are the 25 and 75 percentiles and the median is signified by the line in the middle of the box. A median line that is not centered is indication of a skewed distribution. The whiskers are the lines that are extending from the box edges and they are an indication of the magnitudes in the rest of the sample. The rest of the sample is traditionally considered to be contained within the range defined by 1.5 times the inter-quartile (approximately the

box's length) range away from the box edges. The dots outside the whiskers' range are considered outliers.

In Table B-1 the sample sizes of the hourly precipitation occurrence and the number of cluster events are presented. The Table and the Figures help us to define the characteristics of these distributions. It can be seen that fall and spring have low occurrences of precipitation events compared with summer and winter. However, in fall and spring about 85% and 96% of the occurrences were identified as clusters, respectively. The short duration of most of the clusters can also be seen in Figure B-8. The magnitude of most of the events that occurred in the fall has very small values with low variability but it also has few extreme values. The data also indicated that in fall and spring the number of occasions in which more than a single cluster occur at a given year is very small (29 for fall and 80 for spring).

The above evaluation leads us to assume that the cluster analysis is not warranted for the fall and spring seasons as defined in this study. Therefore, for these seasons we simplify the precipitation generation scheme and resort to resampling from the distribution of inter-arrival periods of precipitation occurrences (vs. cluster occurrences) and the distribution of precipitation magnitudes.

Table B-1: Seasonal characteristics of the precipitation

	Precipitation Occurrences	Number of Clusters
Summer (Jul-Sep)	3160	379
Fall (Oct)	452	386
Winter(Nov-Mar)	2853	272
Spring(Mar-Jun)	431	415

Clearly, the derivation of the distributions reveals some of the summer and winter precipitation characteristics. In both seasons the number of clusters is about 10 percent of the occurrences; however, the summer has many more event occurrences with shorter durations.

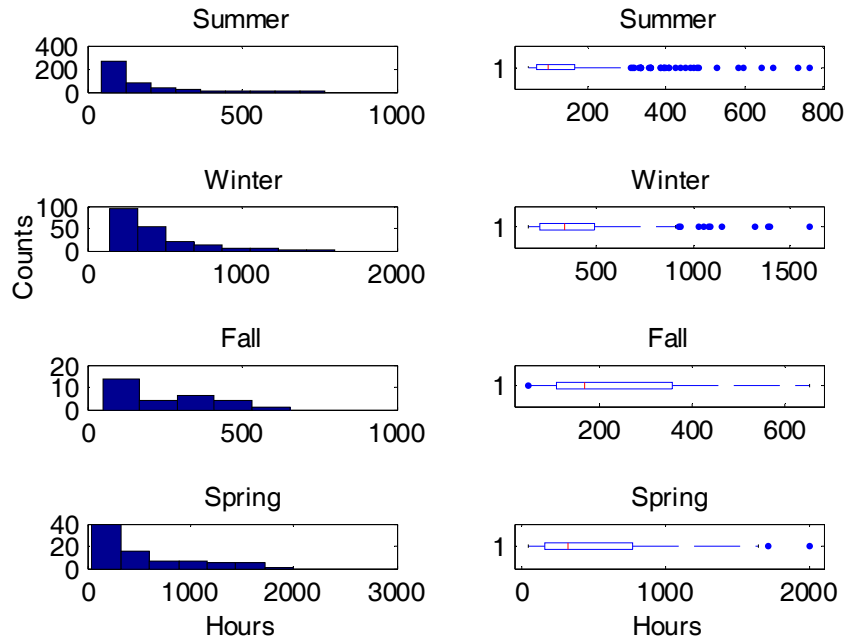


Figure B-7: Histograms of inter-arrival time (hours) of independent clusters.

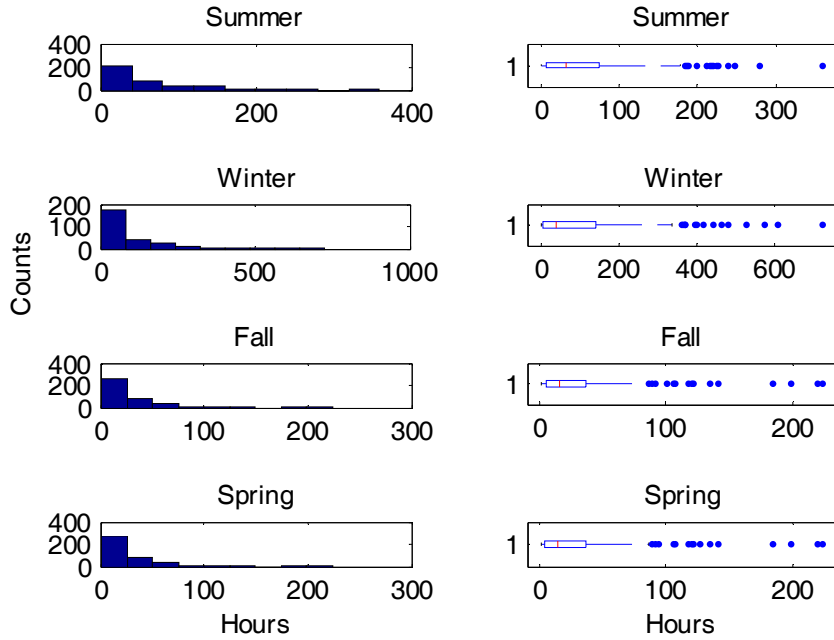


Figure B-8: Histograms of the durations (hours) of independent clusters.

In general all the distributions presented in Figures B-7 to B-15 are positively skewed and in general have a sharp frequency decline from the histogram mode. The box-plots show that even if we exclude the outliers the sample is still positively skewed. A first look at the histograms might yield a conclusion that these distributions can be fitted with parametric exponential distributions. However, in many of these histograms (e.g., summer and winter cluster inter-arrival time (Figure B-7)) there is a discontinuity between the low values and the few extremes. Such a discontinuity can be explained by a bimodal distribution, and fitting a single distribution would sample intermediate values that are not prevalent in the data sample. The large number of outliers in the box-plots also supports this. To maintain the large variability that was found in the sample we would like to maintain these outliers for the stochastic generation. As not enough sample points are available to support fitting a bimodal distribution, the stochastic generation scheme uses a univariate distribution with parameters estimated by including the outliers with the limitations outlined above.

We speculate that the only distribution for which the sampling of the extremes can be compromised is the distribution of the cluster length. In the analysis of the cluster length the few identified extreme long clusters have precipitation occurrences less than 25% of the time. These are probably some cases that the *Restrepo-Posada and Eagleson* test to define a threshold for the minimum inter-arrival time of clusters is not reasonable. For our purposes we assume that a cluster cannot exceed 14 days. Such a constraint is believed to improve the exponential distribution fit, as explained above.

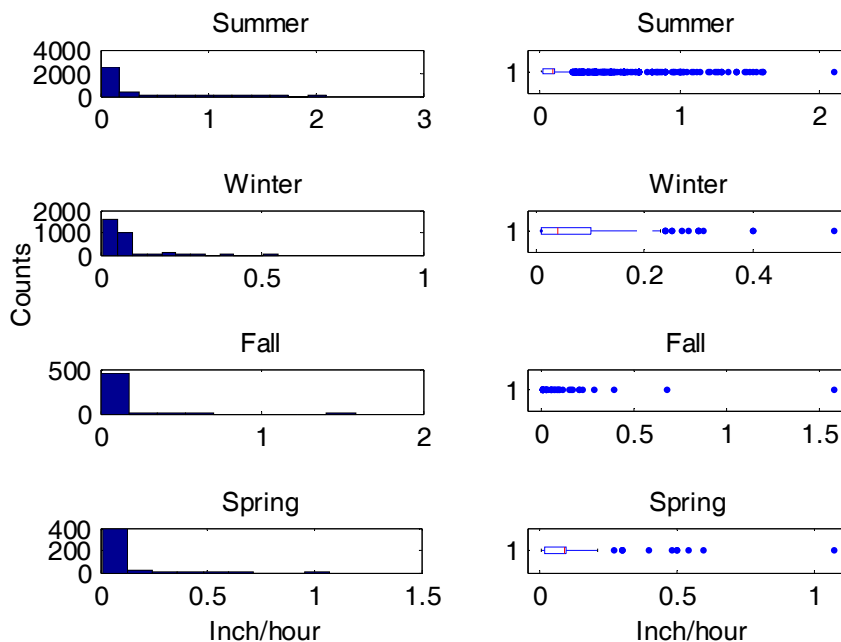


Figure B-9: Histograms of hourly precipitation magnitudes.

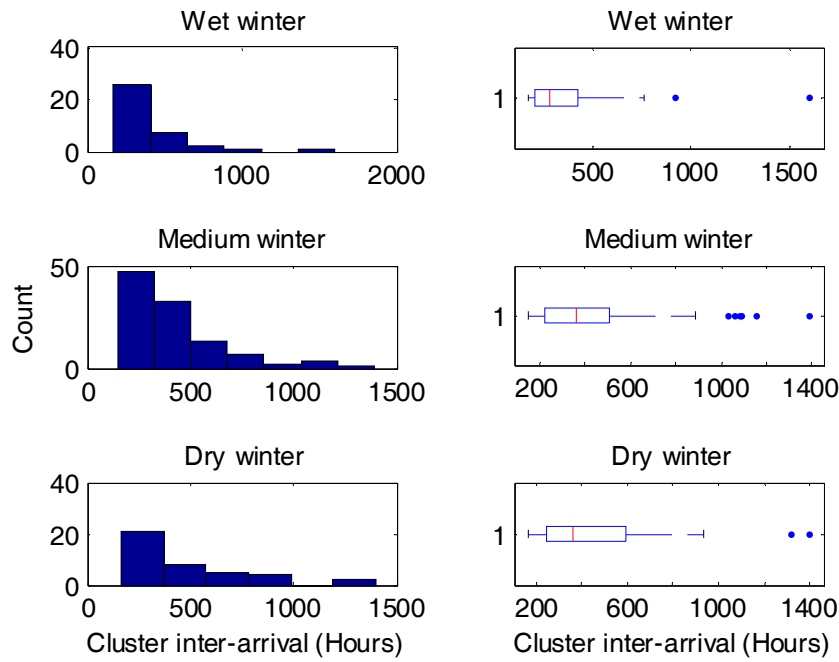


Figure B-10: Histograms of the wet, medium, and dry winter cluster inter-arrival times.

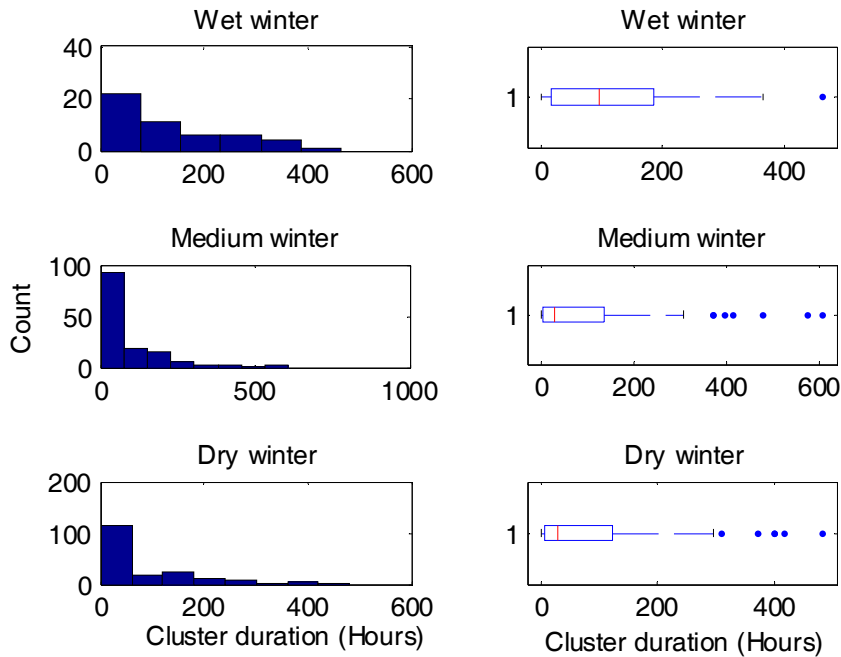


Figure B-11: Histograms of the wet, medium, and dry winter cluster durations.

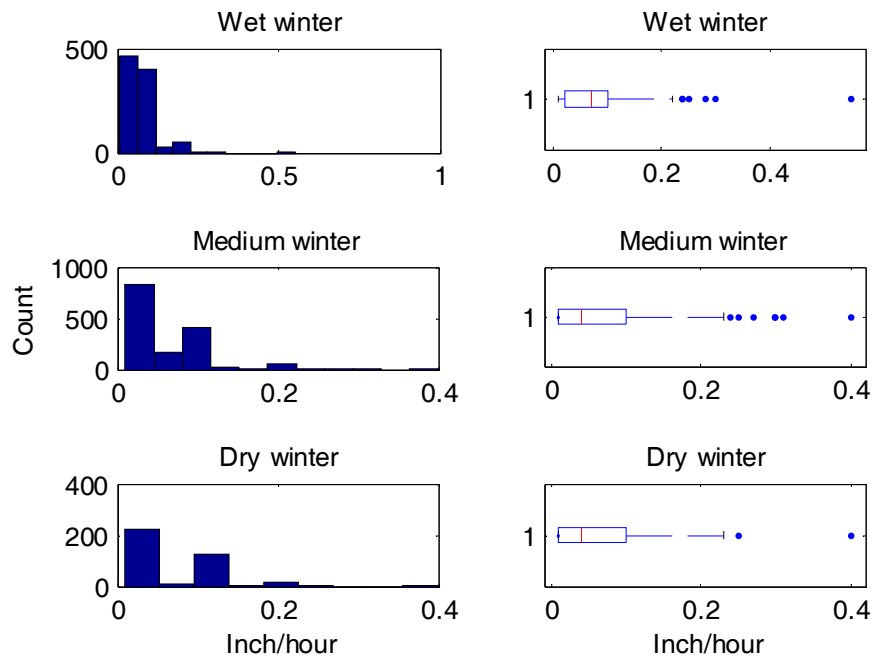


Figure B-12: Histograms of the wet, medium, and dry winter hourly magnitudes

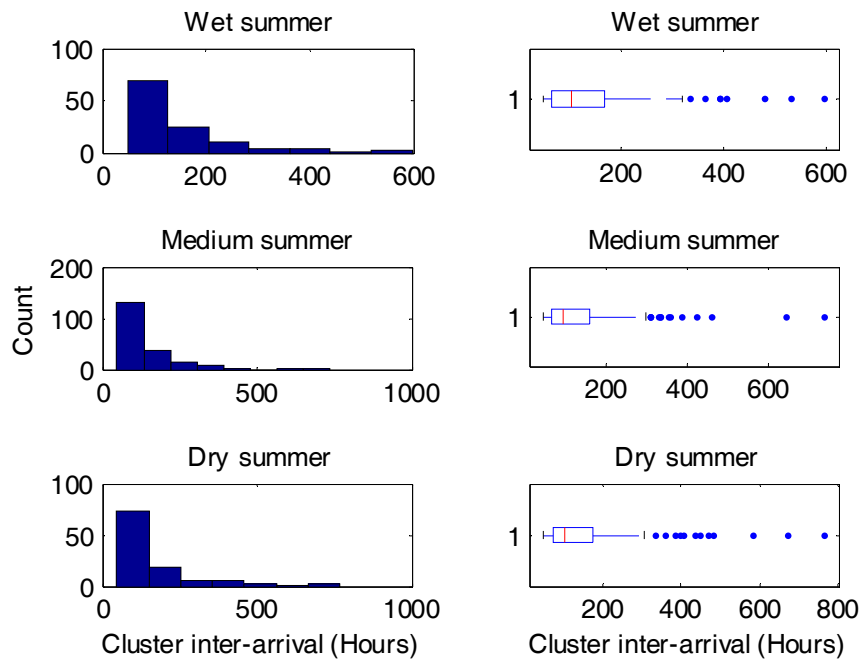


Figure B-13: Histograms of the wet, medium, and dry summer cluster inter-arrival times

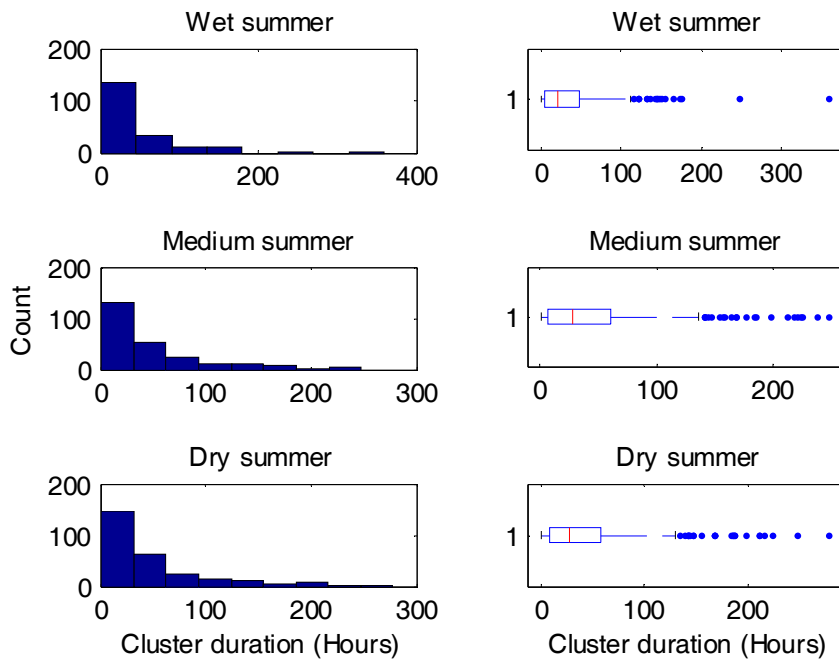


Figure B-14: Histograms of the wet, medium, and dry summer cluster durations.

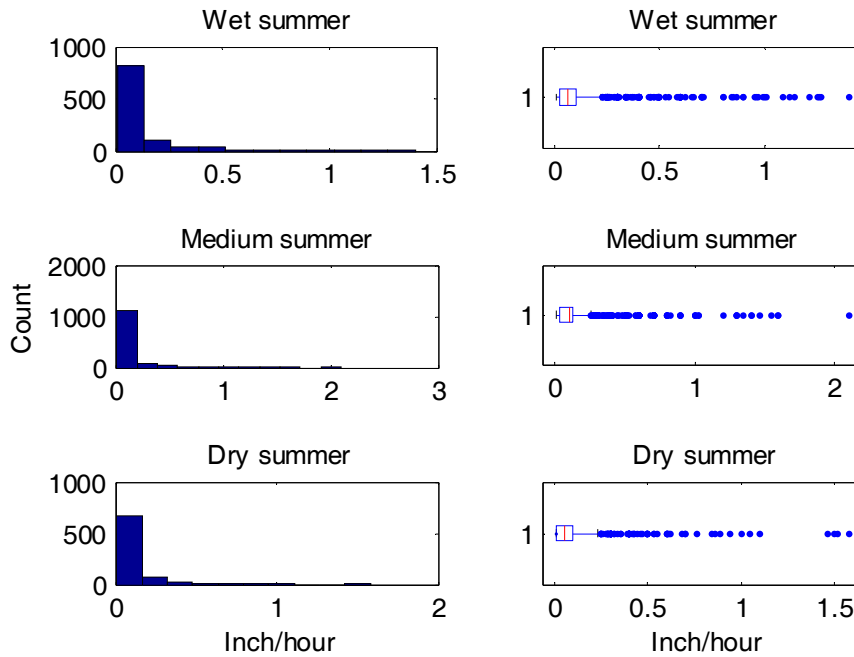


Figure B-15: Histograms of the wet, medium, and dry summer hourly magnitudes.

In order to represent the aforementioned distributions we fitted a two-parameter exponential distribution to the samples:

$$f_x = B^{-1} e^{-\frac{(A-x)}{B}}, \quad A \leq x, \text{ and } B > 0 \quad (1)$$

where, A and B are location and scale parameters, respectively. These parameters were initially estimated using the method of moments, with $B = \sigma_x$ and $A = E(x) - B$, and their values were refined with some manual tuning. In this context, σ_x is the standard deviation of the sample and $E(x)$ is the mean value of the sample.

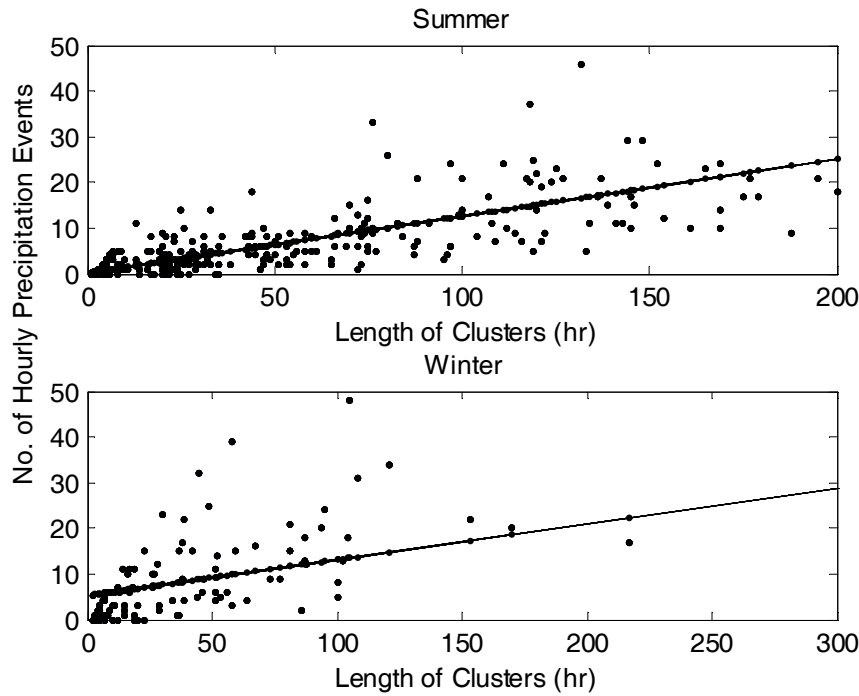


Figure B-16: The number of hourly precipitation occurrences as a function of the cluster duration for summer (upper panel) and winter (lower panel).

To complete the resampling scheme, the distribution of the inter-arrival time of precipitation within the cluster must be specified. Such distribution is dependent on the cluster duration. This dependence implies that the longer the cluster length the higher the number of embedded precipitation events. In this context an event is an hour with non zero rainfall. However, since a cluster always starts and ends with a precipitation event, the chance for precipitation to occur in short clusters is higher than in longer clusters. This dependence is demonstrated in Figure B-16, in which the number of precipitation events within a cluster is plotted as a function of the cluster duration. This result holds true for both summer and winter with different functional relationships, and with higher variability during winter. To sample the inter-arrival periods of precipitation events, we

developed a probabilistic method that maintains dependence on cluster length. For this method the following steps are used:

1. Select the length of the cluster
2. From the observed sample for the season of interest, find the cluster with the smallest absolute difference in cluster length from the selected cluster length. In case that few clusters are identified, randomly select one.
3. Estimate the chance for precipitation to occur (independently) on a given hour within the cluster using data from the observed cluster and the associated duration of its precipitation. For example, if a cluster of length 29 hours is selected and it contains 10 precipitation events (10 wet hours), the chance of precipitation on a given hour in the cluster is estimated as $10/29$.

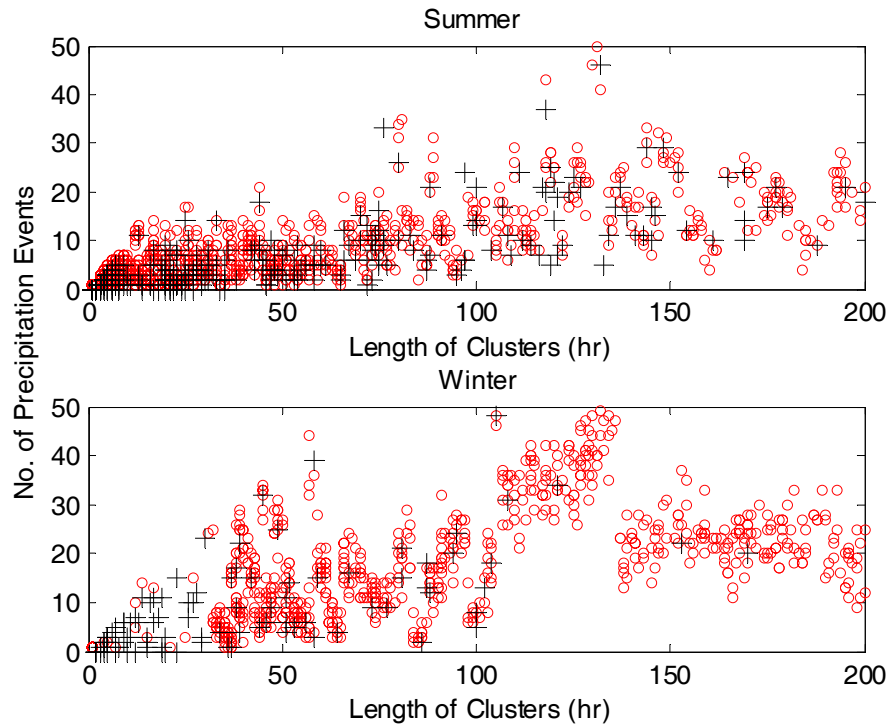


Figure B-17: The relationship between the cluster length and hourly precipitation events in the observations (black plus signs) and the simulations (red circles) for summer (upper panel) and winter (lower panel).

In Figure B-17 the generated number of precipitation events within clusters is shown together with the corresponding observed values for summer (upper panel) and winter (lower panel). It can be seen that the sample characteristics and variability were well preserved in both cases.

In Figure B-18 we provide a summary of the algorithmic steps used for the generation of the synthetic annual hourly precipitation.

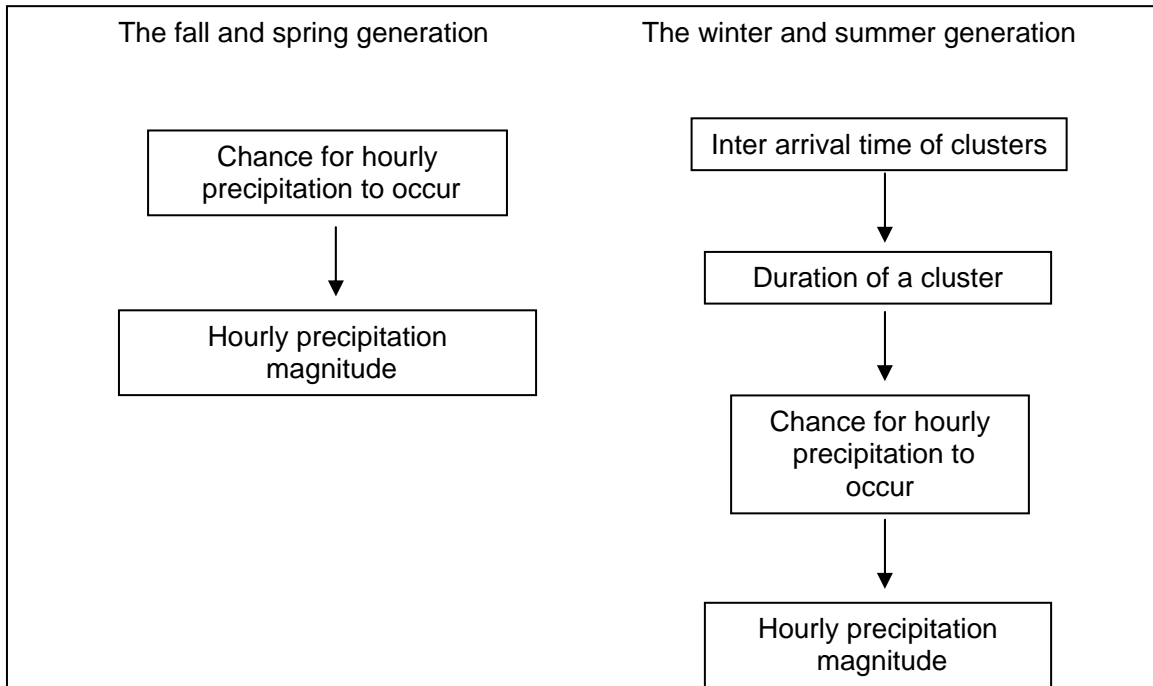


Figure B-18: Steps in the hourly synthetic precipitation generation scheme.

B.3 Synthetic Precipitation Model Performance

In this section we evaluate the performance of the above developed precipitation model by comparing the synthetic model output to the observed precipitation. An indication of the model performance is in the next eight Figures (Figures B-19 to B-26) for the three categories (wet, medium and dry) and for summer, winter, spring and fall. In these Figures, the time series of the observed annual statistics (red) for each year are plotted against simulated annual statistics of hourly precipitation (blue). Both observation and simulation statistics were computed from the same length of record. The following variables are considered: (a) the total annual precipitation volume (inches per year); (b) number of hourly precipitation records per year; (c) number of hourly precipitation amounts that are greater than the trace amount of 0.1 (inch/hour); (d) number of hourly precipitation amounts that are smaller than the trace amount of 0.1 (inch/hour); (e) average hourly rain from rainy days; and (f) average hourly rain of the season (including dry days).

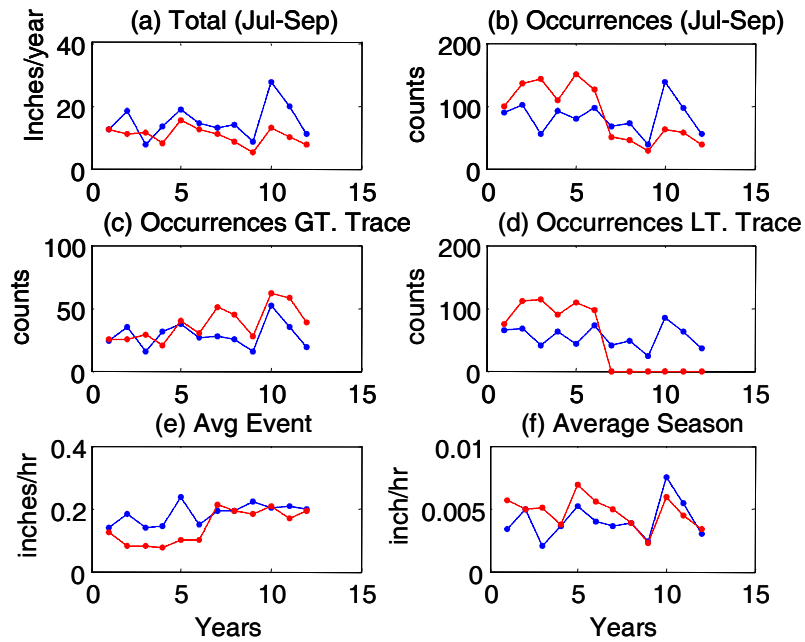


Figure B-19: Comparison of wet summer statistics between observed (red) and generated (blue) values of (a) annual total precipitation, (b) number of hourly precipitation events, (c) number of hourly precipitation events greater than 0.1 inches/hour, (d) number of hourly precipitation events less than 0.1 (inches/hour), (e) average hourly precipitation of events, and (f) average hourly precipitation of season.

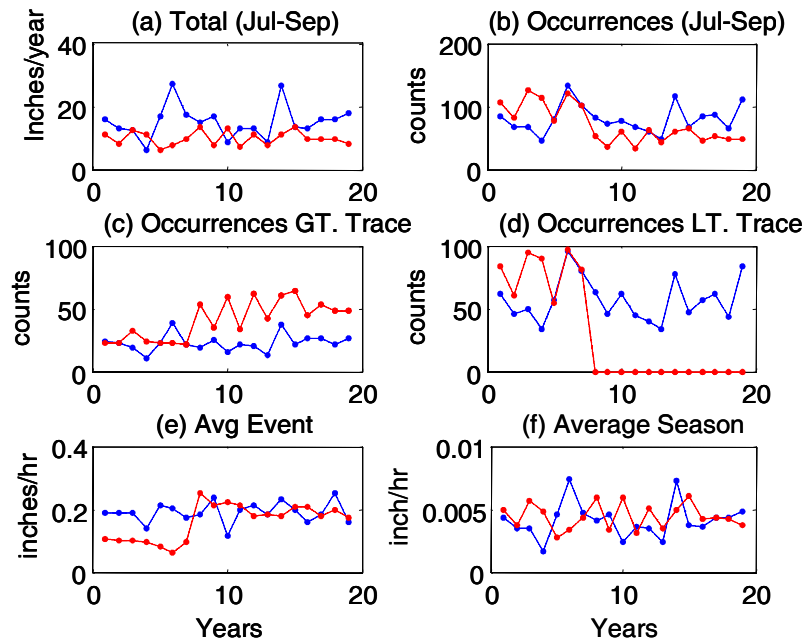


Figure B-20: As Figure B-19 but for medium summer.

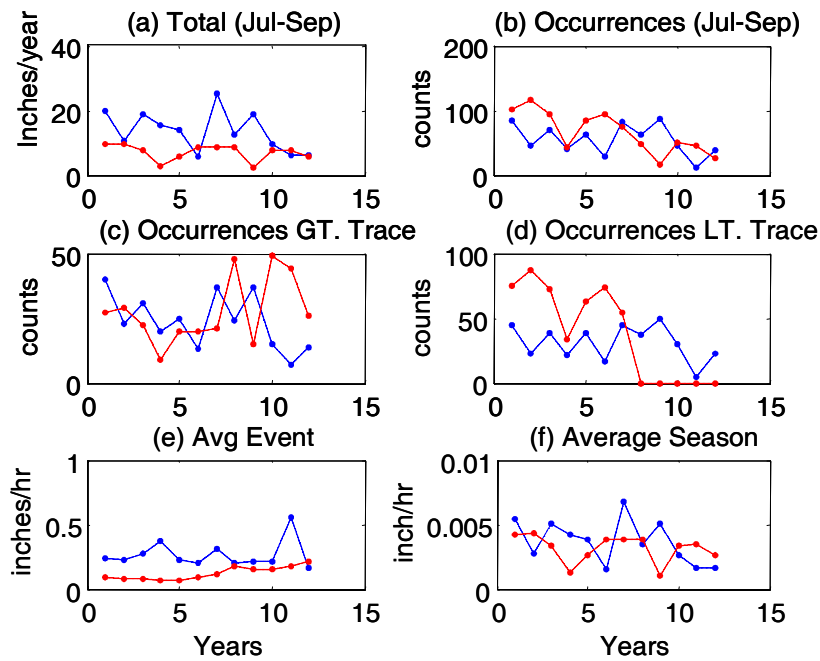


Figure B-21: As in Figure B-19 but for dry summer.

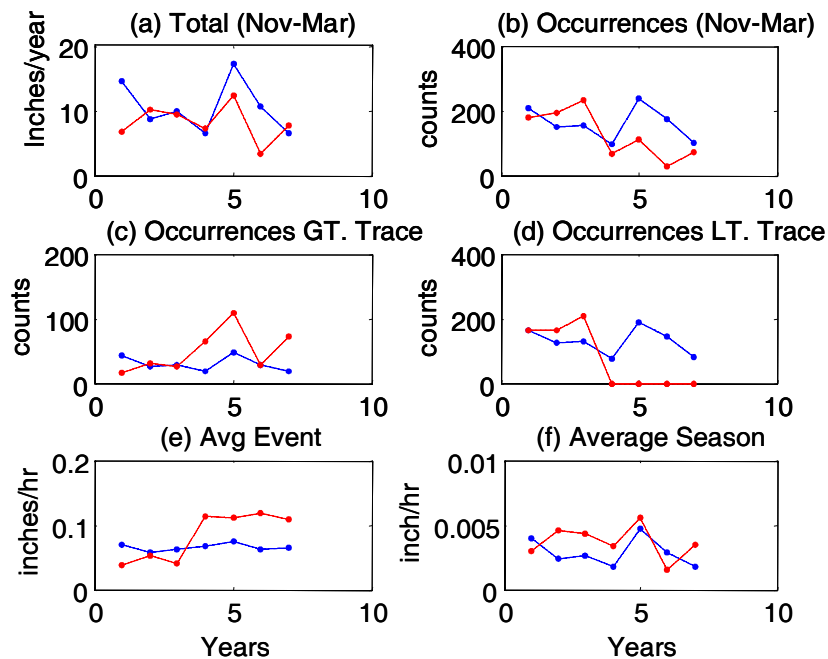


Figure B-22: As in Figure B-19 but for wet winter.

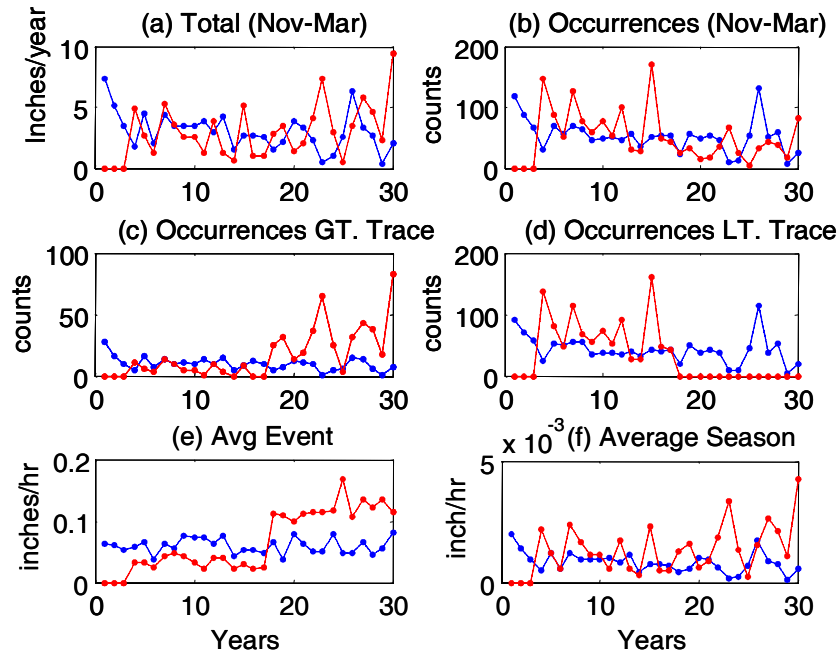


Figure B-23: As in Figure B-19 but for medium winter.

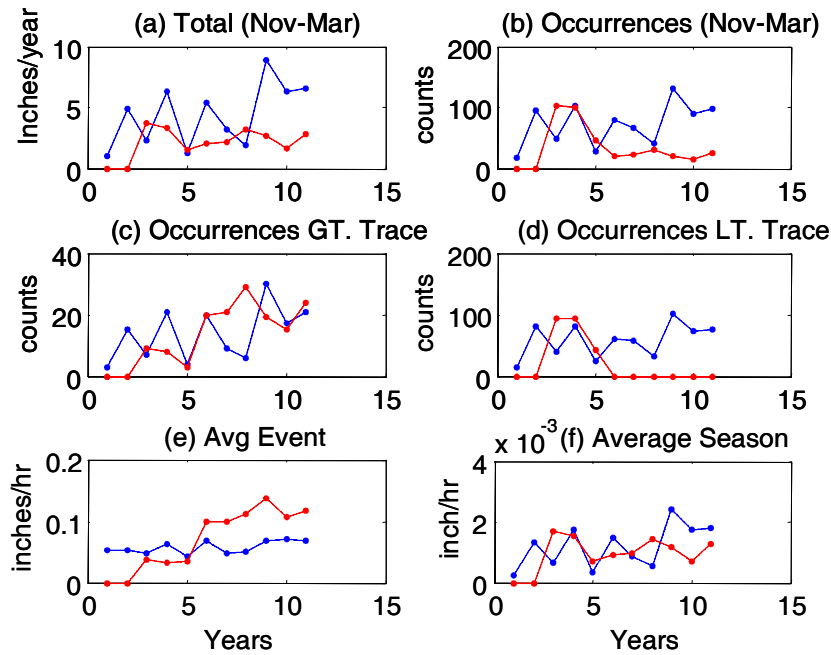


Figure B-24: As in Figure B-19 but for dry winter.

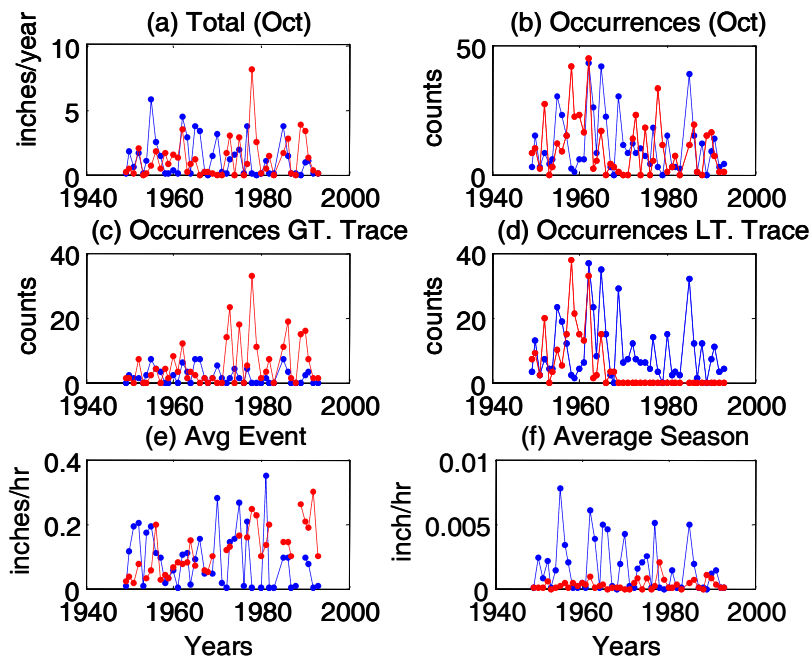


Figure B-25: As in Figure B-19 but for fall (all size events).

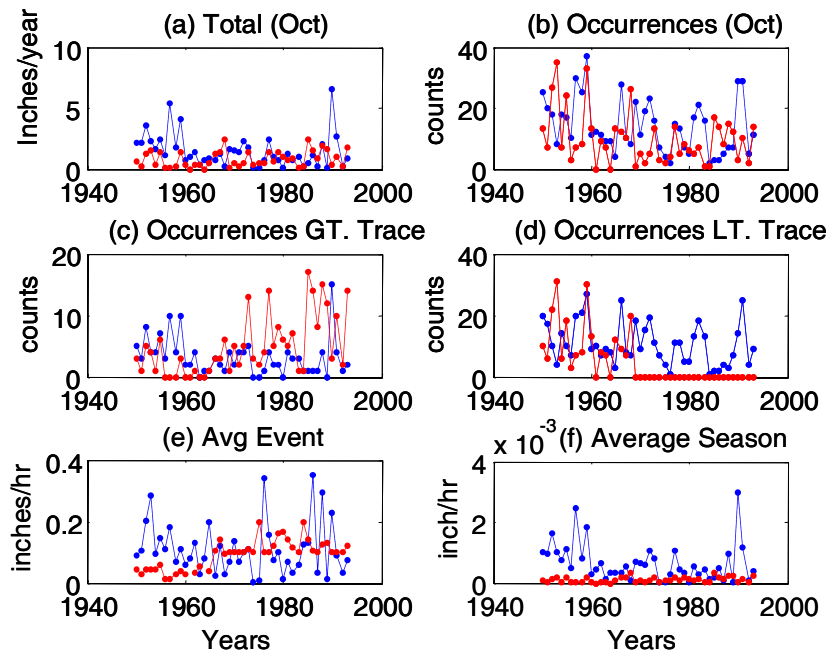


Figure B-26: As in Figure B-19 but for spring (all size events).

These Figures indicate a shift in the observed frequency of occurrence of events in the early seventies (panel *b*). In panels *c* and *d*, it appears that the number of events greater than 0.1 inches/hour increases, and the number of events smaller than 0.1 inch/hour decreases with time in all the seasons. Moreover, it can be seen that this corresponds with an increase in the average magnitude of the events (panel *e*). This is likely the result of changes in the recording increments and the calibration of the gauge. The simulation of precipitation is built based on parametric analysis of the entire time series and this shift is part of the variability in the record. Overall the annual magnitude is preserved as shown in panels (*a* and *f*), with the frequency of occurrence of summer hourly precipitation events also preserved (panel *b*).

The estimated parameter values of the exponential distribution for all cases are presented in Table B-2.

Table B-2: Parameter values of the exponential distributions that are used to simulate the hourly precipitation at Nogales. In parenthesis are the fitted parameters that are used to match the flow.

	Cluster inter-arrival period		Duration of cluster		Hourly precipitation magnitude	
	A	B	A	B	A	B
Winter: Wet	0.06	0.17	0.02	0.26	0.02	0.1 (0.5)
Medium	0.11	0.4	-0.05	0.1	0.008	0.14
Dry	0.12	0.3	-0.04	0.1	0.08	0.12
Summer: Wet	0.06	0.4 (0.1)	0.02	0.17	-0.04	0.13 (0.5)
Medium	0.04	0.5 (0.15)	-0.01	0.3 (0.2)	-0.03	0.1
Dry	0.02	0.45 (0.4)	-0.015	0.2	-0.04	0.15 (0.1)
	Hourly precipitation chance				Magnitude	
Fall	-0.03	0.2 (0.05)			-.009	0.04 (0.015)
Spring	0.04	0.24			-0.01	0.087 (0.01)

B.4 Conceptual Hydrologic Model

In order to convert the rainfall point process into a sequence of flow hydrographs, a conceptual hydrologic model was developed. The model represents an infiltration excess runoff production process that varies dynamically as a function of the basin antecedent moisture conditions. Such model is believed to be representative of the arid environment in which infiltration excess is the dominant runoff production process. The infiltration rate is formulated as follows:

$$f(t) = f_{\min} + (f_{\max} - f_{\min}) \left(\frac{S_{\max} - S(t)}{S_{\max}} \right)^p \quad (2)$$

where, $t=1, \dots, n$ is the time step, f is the infiltration rate (inch/hour), f_{\min} and f_{\max} are the minimum and maximum infiltration rates respectively, $S(t)$ represents the soil water storage (inches) at time t with capacity S_{\max} , and p is an exponent parameter nominally dependent on soil characteristics.

Surface flow (Q_s) (inches/hour) is generated as follows:

$$Q_s(t) = P(t) - f(t) \quad , \quad P(t) > f(t) \quad (3a)$$

$$Q_s(t) = 0 \quad , \quad P(t) \leq f(t) \text{ \& } S(t) + P(t) \leq S_{\max} \quad (3b)$$

$$Q_s(t) = S(t) + P(t) - S_{\max} \quad , \quad P(t) \leq f(t) \text{ \& } S(t) + P(t) > S_{\max} \quad (3c)$$

where $P(t)$ is the precipitation (inch/hour) measured at the gauge at time t . The model also generates a baseflow component (Q_b), which is linearly proportional to the soil water storage with a coefficient k (hour^{-1}):

$$Q_b(t) = kS(t) \quad (4)$$

Such model formulation requires estimation of four parameters (S_{\max} , f_{\max} , p , and k), while, in order to maintain conservation of mass, $f_{\min} = kS_{\max}$. A schematic representation of the model is in Figure B-27. It is noted that an additional abstraction may be added for the storage element to simulate anthropogenic use of water. For this development we examine model behavior without such an abstraction.

The only state variable in such model is the storage (S). We assigned for each year a random storage initial condition as a fraction of S_{\max} to account for the often observed baseflow which is carried from a previous season.

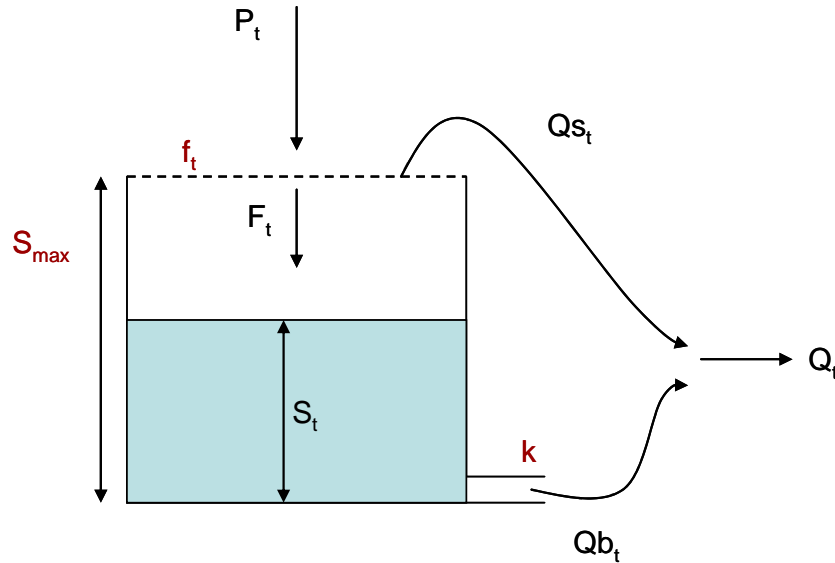


Figure B-27: Schematic representation of the conceptual hydrologic model. In black letters are the precipitation (P), infiltrated volume (F), soil water storage (S), surface flow (Q_s), baseflow (Q_b) and total flow (Q) fluxes at a given time (t). In red are the flux control parameters that include the infiltration rate (f), the maximum storage capacity (S_{max}), and the soil water depletion coefficient (k).

B.5 Parameter Estimation of the Hydrologic Model

Clearly precipitation rates at the precipitation gauge at Nogales do not solely force the flow observed at the USGS Nogales stream gauge site. However, it is reasonable to assume that most identified precipitation clusters are the results of the larger scale weather occurrences that generate the precipitation forcing of streamflow at the USGS Nogales gauge site. Comparing the observed summer and winter clusters of hourly precipitation with the observed flow events, we identified 80 and 40 summer and winter flow events, respectively, that correspond to that precipitation forcing. The identification of these matched events was done manually by selecting flow hydrographs within the USGS Nogales gauge record that have rising limbs which are within the time duration of a precipitation cluster. The estimation of the values of the conceptual hydrologic model parameters is done by comparing (a) the frequency distribution of the daily flow model simulations that resulted from forcing the model with the precipitation clusters, with (b) the frequency distribution of the observed daily flows that were identified as having a cluster association. We emphasize that the association of precipitation and flow is statistical in nature and not direct (one-to-one), and thus, it is appropriate to calibrate the model on the flow statistics rather than the flow itself.

A synthetic time series of 300 hourly precipitation clusters was generated. Each generated cluster was added a dry period of 2 and 6 days for the summer and winter respectively. We note that for this calibration, mean cluster inter-arrival periods were used for the winter and summer. The hydrologic model ran with hourly time steps, which

ensures numerical stability, to generate hourly total flow (inch/hour). The precipitation rate at the gauge site generates runoff in units of precipitation, which is subsequently converted to mean daily flow for comparability with the observed mean daily flow. For this conversion, an effective spatial scale coefficient (A) is introduced.

The frequency distribution of the observed flow events (red dots in Figures B-28 and B-29 for summer and winter, respectively) exhibits a steep change in slope for the higher magnitude flow events (with a frequency of occurrence greater than 90%). Such a steep change requires an A factor that is magnitude dependent. The implication of a variable coefficient implies that higher intensity events have a larger scale of effective area. We defined a precipitation threshold parameter (Tp) in which precipitation greater than Tp is multiplied by a coefficient (m) (see Table B-3 for the Tp and m values). These parameters were determined by trial and error.

Table B-3: Optimal hydrologic model parameter values.

	K $hour^{-1}$	S_{max} (inch)	f_{max} (inch/hr)	p	A ($ft^2/12$)	Tp (inch/hr)	m
Winter	0.08	4	0.8	1.3	22000000	0.52	20
Summer	0.13	22	0.4	3.1	11000000	1.85	5
Fall	0.02	24.5	0.2	1.8	21000000	0.5	2
Spring	0.02	24.5	0.2	1.8	2000000	0	0

In Figures B-26 and B-27, the black lines show the range of flow obtained from a generated sample of 100 realizations using a Monte Carlo simulation with varied parameters (but with fixed precipitation input). The green line is the simulation of flow that is closest to the observed red dots. The measure of fit is the root mean square error between the observed and simulated frequency distribution of the Box-Cox transformed flows. Table B-3 shows the values of the optimal parameters and the root mean square error of the Box-Cox transformed flows. For the fall and the spring for which we do not have a sufficient number of clusters we estimated the parameters using trial and error.

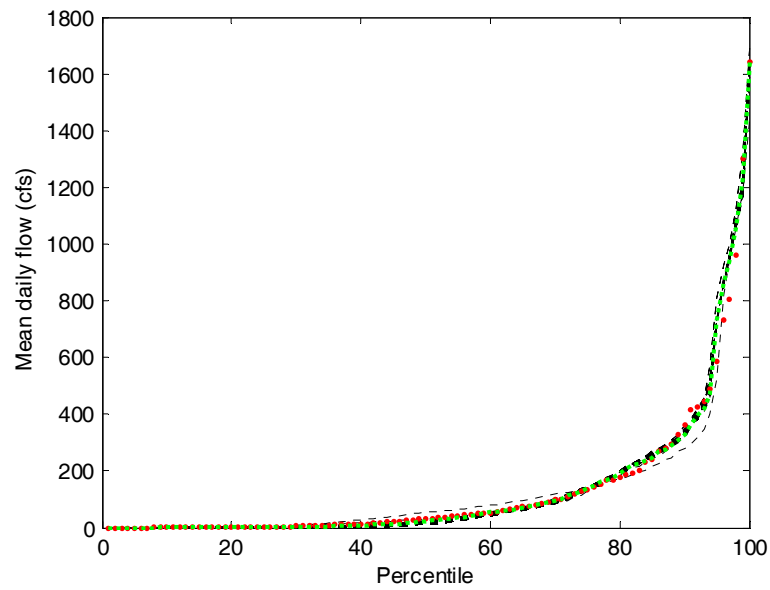


Figure B-28: Frequency distribution of summer daily flow: summer observed (red dots), range of Monte Carlo simulated (dashed black lines), and simulated with optimal parameter sets (green line). All generated flows are forced by observed precipitation clusters.

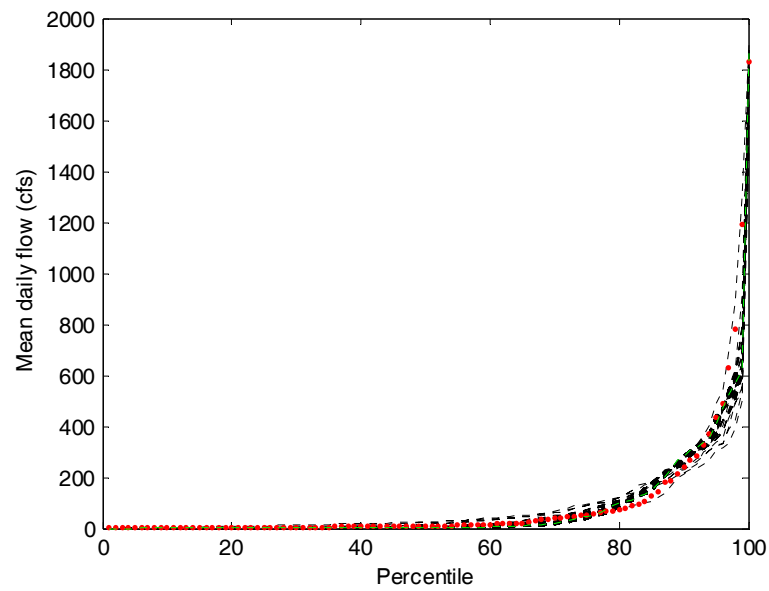


Figure B-29: As in Figure B-28 but for winter.

B.6 Performance of the Flow Generation Model

Up to this point we first developed a model that generates hourly precipitation for four seasons which preserves the intermittent nature of the precipitation process. We then transformed this precipitation with a simple conceptual hydrologic model to flow, with model parameters calibrated on the basis of statistics derived from a set of matched precipitation clusters and flow events. In this section we further evaluate the generated flow time series by comparing it to the flow observations at the USGS Nogales gauge site. The performance evaluation was conducted for the four seasons and includes performance evaluation of the daily, seasonal, and annual time scales.

In order to perform well in the generation of flow some of the distributions of the precipitation resampling scheme had to be tuned for ‘what would have been’ the effective hourly mean areal precipitation as opposed to the statistical properties of point precipitation determined from the observation gauge. Moreover, to account for scaling of the precipitation events, the effective area factor is varied based on precipitation magnitude.

Both of these are diagnostic activities that help understand the information content of the precipitation gauge record with regard to the flow generated in the Nogales gauge. The tuned values of the exponential distribution parameters are presented in parenthesis in Table B-2. In general, increase in the value of parameter B yields a distribution that approaches uniform distribution, while, a decrease in the value of B results in sharper decline of the distribution of precipitation amount.

The major changes were for the summer season. For the three summer categories, the B value was decreased for the inter-arrival time of cluster distributions. Such tuning implies that the inter-arrival time between clusters is shorter and more clusters are generated per season than observed at the precipitation gauge. Such correction is necessitated by the deficiency of having only a single point with precipitation data and by the localized convective type of storms in summer. That is, flow generating precipitation events may have occurred on other parts of the watershed and were not recorded by the Nogales precipitation gauge, but have contributed to the flow record.

Other corrections were made for the summer season precipitation magnitude distributions to increase the difference between the dry and wet summer magnitudes. These changes created more gradual and sharper magnitude distributions for the wet and dry summer periods, respectively. This tuning implies that the summer categories are observed to be more distinct in the gauge flow than the precipitation record from the single gauge. A correction similar to the wet summer magnitude distribution was also made to the wet winter magnitude distribution. During the drier seasons (i.e., fall and spring) both the magnitude and the chance of precipitation occurrence had to be tuned to produce sharper exponential distributions. Such corrections imply fewer flow events and decrease the chance of large-event occurrence.

It can be seen that the daily flow simulation tends to preserve the behavior of the observed flow frequencies.

In Figure B-30 to B-32 the synthetic-flow reliability is evaluated for the daily, seasonal, and annual time scales, respectively. Descriptive statistics (i.e., mean standard deviation etc.) are not sufficient in describing variables with such large variability. Therefore we conduct a more rigorous analysis that is based on comparing the frequency distributions between the observations and simulations. This is done by constructing exceedance plots. Such curves can be interpreted as the percent of daily flow events (x-axis) with magnitude that is larger than a given flow value (y-axis). Such comparisons between the curves provide a visual tool for comparisons of the distribution of magnitude in the flow records. In Figure B-30 performance of the daily flow is evaluated by comparing the exceedance plots of the daily Box-Cox transformed flow of the observation and simulation. The simulated exceedance plot is generated from 100 model realizations, each of 68 years long. In Figure B-31 the total seasonal volumes are compared between the 68 observed years and 100 realizations of 68 years. Figure B-32 compares the annual flow volumes of the observed time series with that of the 100 realizations.

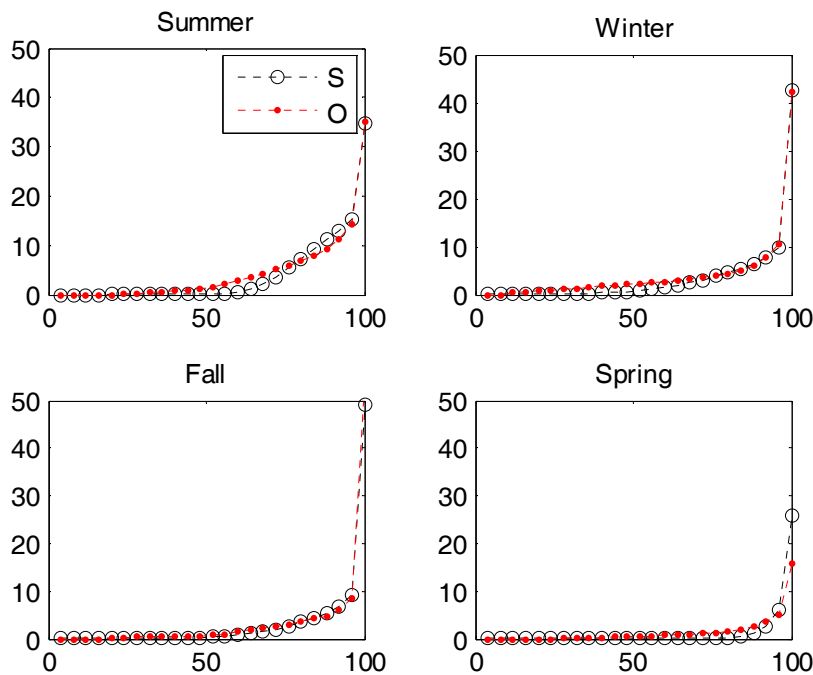


Figure B-30: Exceedance plots of the daily Box-Cox transformed flow of 68 years of observation (black circles), and 100 realizations of generated flow, each with a duration of 68 years of synthetic flow (red dots).

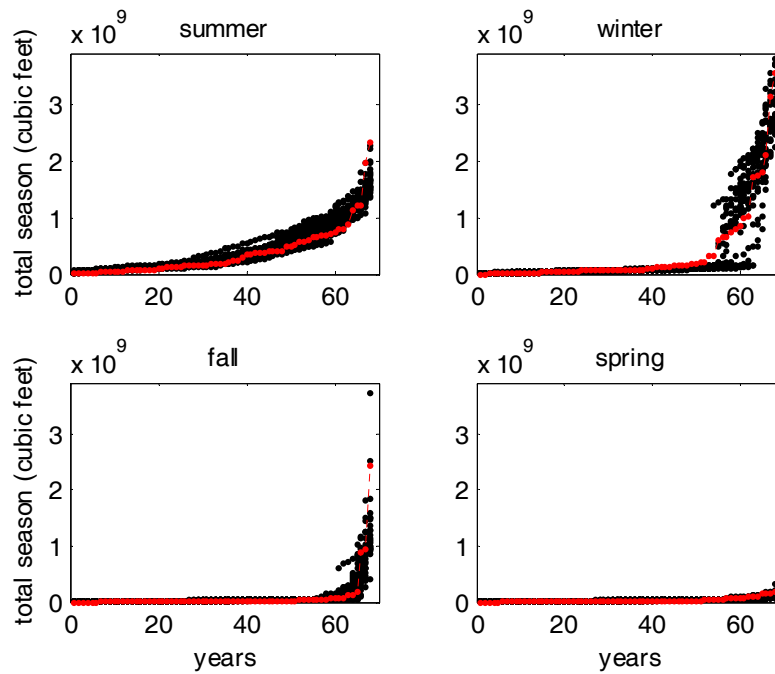


Figure B-31: Exceedance plots of the total seasonal observed flow volumes in $\text{ft}^3 \cdot 10^9$ for 68 years (red) and 100 realizations of generated flow, each with a duration of 68 years (black dots). (Conversion: 1 AF = 43,560.25 ft^3 .)

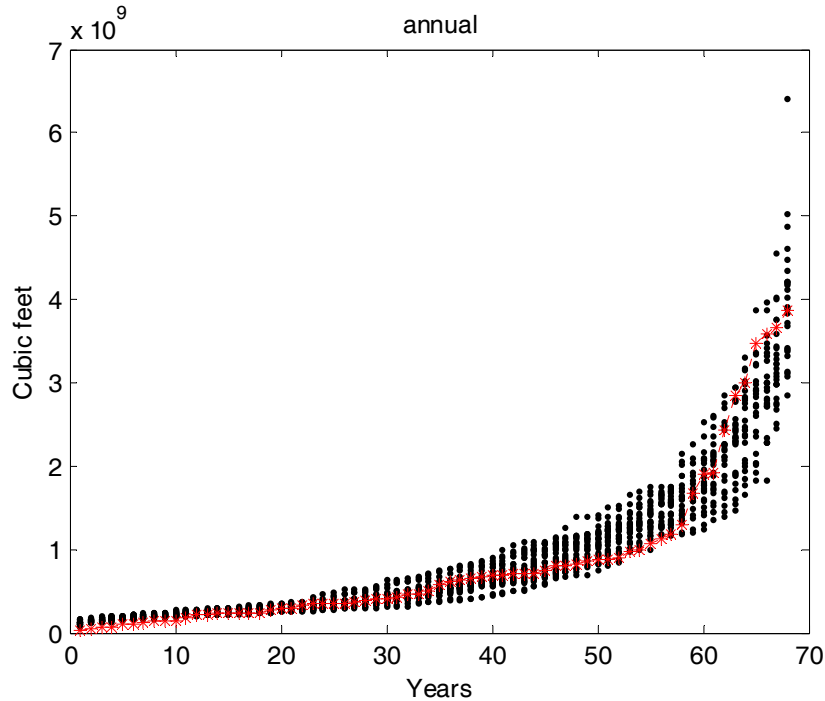


Figure B-32: Exceedance plots of the annual observed volumes in $\text{ft}^3 \cdot 10^9$ for 68 years (red) and 100 realizations of generated flow, each with a duration of 68 years (black dots). (Conversion: 1 AF = 43,560.25 ft^3 .)

It can be seen from these Figures that for three relevant time scales the simulations and observations compare reasonably well. Next, in Figures B-33 and B-34, ten winter and summer generated and observed hydrographs were plotted for visualization purposes. As discussed above, the hydrologic response in winter is different from that in summer. Visual inspection of Figures B-33 and B-34 indicates that the large inter-annual variability is reproduced and the overall appearance of the observed and generated hydrographs is similar in shape and frequency of occurrences.

B.7 Summary

In this section we developed daily flow simulation at the Nogales Gauge that is based on synthetic generation of hourly precipitation. The synthetic flow generation was developed using statistical features of hourly observations from a gauge that is located downstream of the Nogales streamflow gauge. We divided the time series into 4 seasons and the summer and winter were further categorized into wet, medium and dry seasons. A generation scheme of these seasonal categories was developed by matching exponential distributions to sample populations of the inter-arrival time of clusters, cluster durations, and magnitude of hourly precipitation. The chance for precipitation to occur within a cluster is sampled as a variable that is dependent on the cluster duration.

Transformation of the precipitation into flow was done by using a simple conceptual hydrologic model suitable for semi-arid and arid regions. Using matching clusters between observed precipitation and flow, and, assuming that the same statistics that were found in the gauge precipitation record are representative of the mean areal precipitation that is forcing the Nogales flow, we estimated the hydrologic model parameters for winter and summer.

The model is evaluated both by comparing key statistics of the observed rain and flow to analogous statistics of generated rain and flow. The results indicate good reproduction of the flow exceedance frequencies for the daily, seasonal and annual time scales.

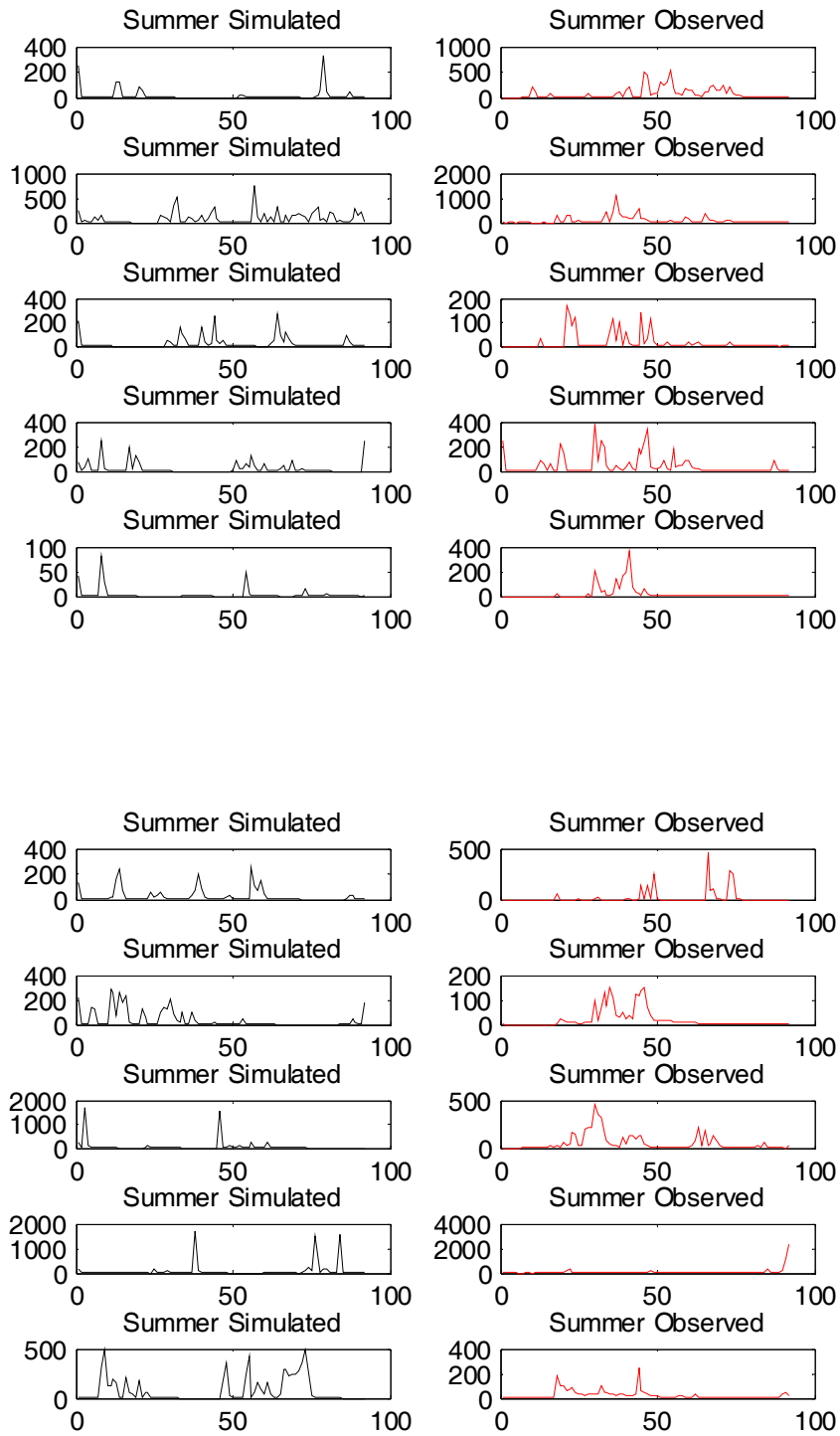


Figure B-34 Summer simulation of daily hydrographs (left panels) and observed hydrographs (right panels).

Chapter C

Synthetic Flow Model ARMA(1,1)

C.1 Generation of synthetic monthly flow at the Nogales gauge

As seen in Chapter A, the monthly total flow at the Nogales stream gauge might be perceived as perennial flow with no extended and frequent periods of no-flow and, therefore, we can resort to traditional autoregressive moving-average methods for the generation of synthetic flow. To produce synthetic time series any significant non-stationary evidence (trends, seasonality shifts) should be identified and removed from the data prior to the definition of the statistics to be used in the generation. In addition, we transform the data in an attempt to derive a time series with properties that resemble the characteristics of a normal distribution.

The monthly time series at the Nogales gauge is positively skewed (skewness coefficient = 6) with exponential distribution appearance (Figure C-4, upper left panel). Subsequent to experimenting with a variety of transformation methods to approximate normal distribution for the transformed Nogales monthly flow, we used the following transformation steps: (1) The monthly volumes were transformed using the Box-Cox transformation ($\lambda = 0.1$). We experimented with different coefficient values and the selected value appears optimal for reducing the transformed time series coefficient of skewness. (2) The seasonality in the mean and variance of the transformed flow was removed using:

$$y_{i,j} = \frac{x_{i,j} - \bar{x}_j}{s_j}$$

where i and j are indices for year and month, respectively, and x , \bar{x} , and s are flow, mean, and standard variation of the Box-Cox transformed monthly flow.

In Figure C-1, the actual monthly flow time series is presented in the upper panel followed by the standardized and transformed monthly flow in the middle and lower panels, respectively. The descriptive moments of Transformed and Standardized Monthly Flow (hereinafter TSMF) are 0, 0.99, and 0.8 for the mean, standard deviation, and skewness coefficient, respectively.

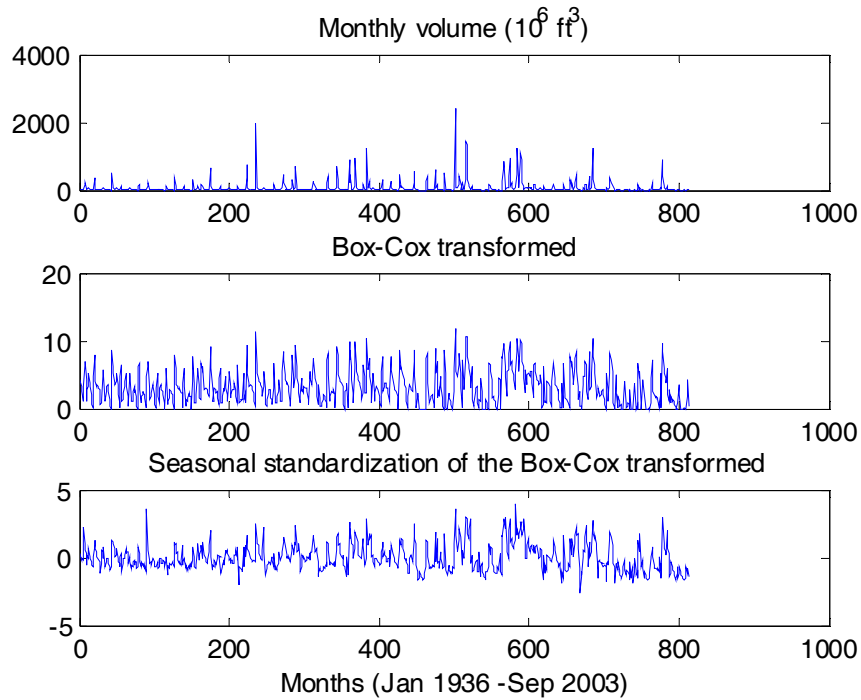


Figure C-1: Observed monthly flow (upper panel), Box-Cox transformed monthly flow (middle panel), and standardized and transformed flow (lower panel).

In Figure C-2, the 24-month moving average of the mean and standard deviation of the TSMF is plotted. It reveals that the mean is practically constant, i.e., stationary, while the standard deviation is increasing with time. The source of the trend in the variance is not clear and further investigation is needed on the hydro-climatologic properties that shaped this trend. In Figure C-3, we propose to treat this trend in the variance as a shift that occurred in the mid 60s. In Figure C-3, the moving average of standard deviation is divided into two groups 1936-1961 and 1962-2002. It can be seen in the figure that the S.D. for these groups appears stationary. It has to be acknowledged that such trends are difficult to confirm because of the high amplitude of the variability. Therefore, although treating the dataset for the shift reduces the apparent non-stationary, the shift itself might not be a physical characteristic of the system.

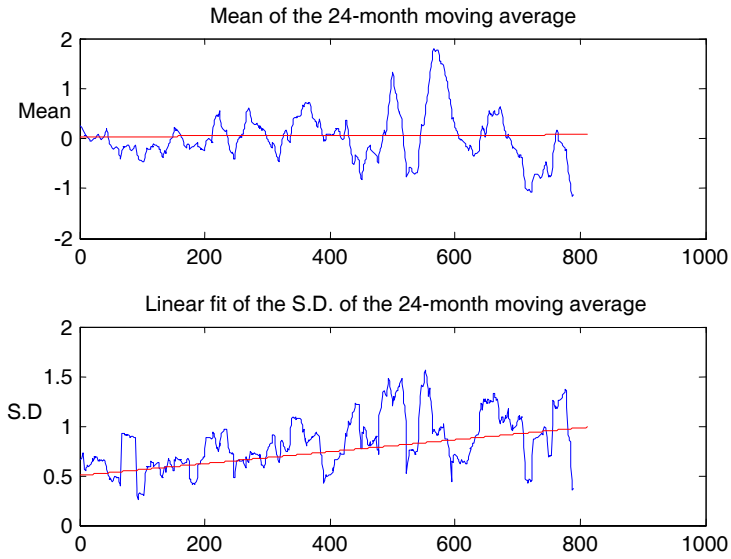


Figure C-2: Moving average of 24-months duration for the mean and stadard deviation of the transformed and standardized time series.

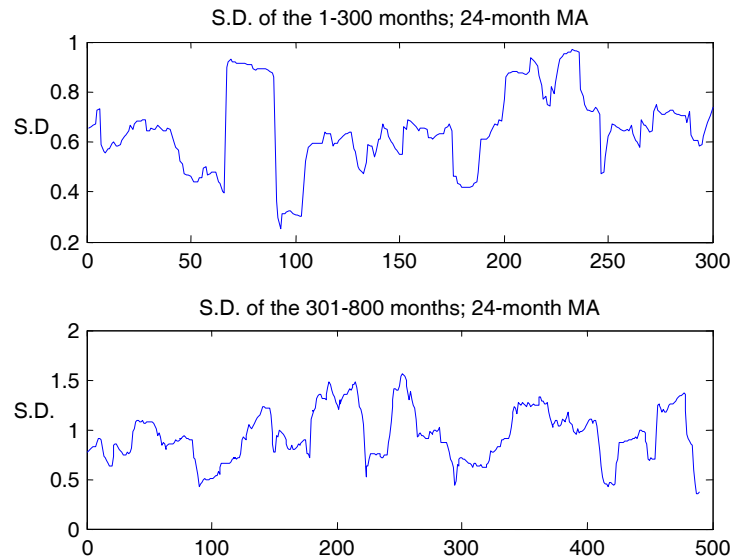


Figure C-3: Moving average of 24-months duration for the standard deviation of the transformed and standardized time series for the first 300 months (upper panel) and the remaining months of the time series (lower panel)

It is noted that the transformation and standardization provides a time series that has a positive skew (albeit much smaller than that of the untransformed flows). In Figure C-4, the frequency distribution of TSMF (Figure C-4b) is presented and compared to the frequency of the normal $N(0,1)$ distribution (Figure C-4c). In Figure C-4d, we present the frequency distribution resulting from a resampling scheme that is based on the normal distribution and which generates a distribution that appears similar to the TSMF distribution. The conditioning implied for that consists of 1) draws that are either smaller than -2.5 or greater than 4, respectively, are discarded and replaced by a another draw; 2) all the valid draws are rescaled using a multiplier (0.85). These steps of truncation and scaling are used to create a symmetric distribution with variance of about 1.

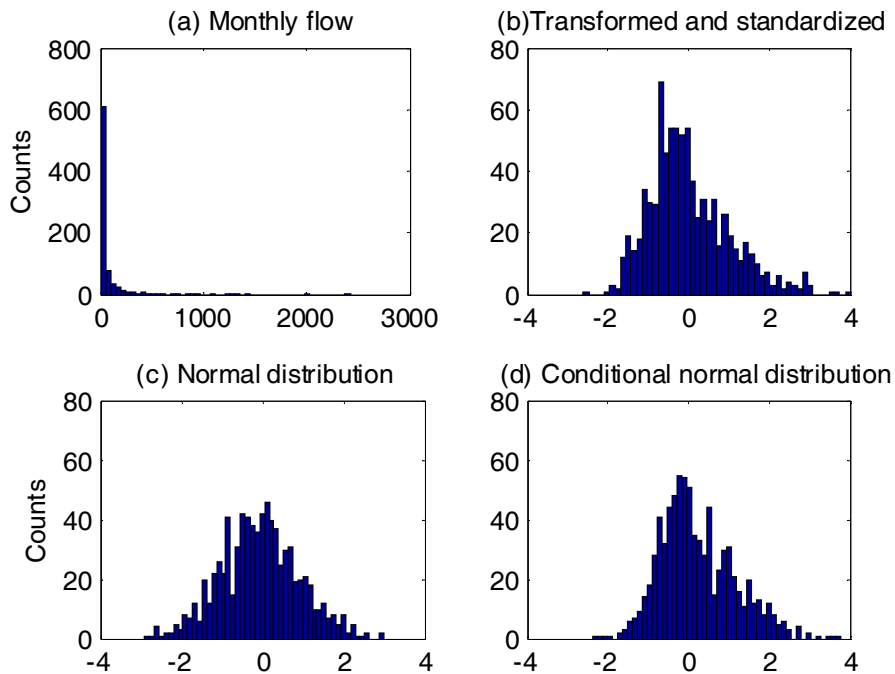


Figure C-4: Probability density functions of a) the monthly flow volume; b) the TSMF time series; c) resampled normal distribution $N(0,1)$; and d) conditionally resampled normal distribution.

C.2 ARMA(1,1) model

In this section we develop a stochastic model that generates synthetic monthly flow values. We evaluate the model for three cases (1) on the entire time series; (2) 1936-1961 and 3) 1961-2003.

The gradual exponential decline of the TSMF correlogram (Figure C-5) with the increase of lag time is an indication that the time series can be simulated using a Markovian model. Such a model is built upon the assumption that the entire influence of the past can be summarized by the previous flow value.

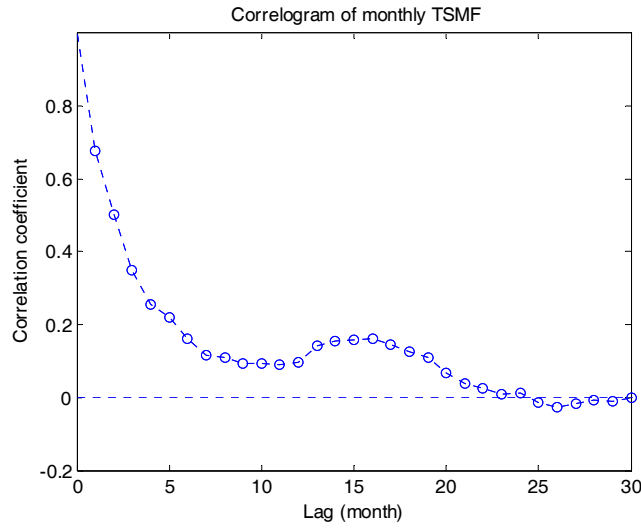


Figure C-5: Correlogram of the monthly TSFM.

Therefore, we decided to use the lag-1 auto-regressive moving-average model (ARMA (1,1)). A synthetic model contains deterministic and random components, and selecting the ARMA model implies that there is temporal persistence in both components.

The ARMA model is formulated as follows:

$$y_t = \alpha y_{t-1} + \beta z_t + \gamma z_{t-1} \quad (\text{C-1})$$

where, y is the synthetic flow prediction, z is the random error term and α , β , and γ , are the ARMA(1,1) parameters. The subscript t indicates the time step. The model parameters are estimated using the method of moments (*Salas 1993*):

$$\alpha = \frac{r_2}{r_1} \quad (\text{C-2})$$

where, r is the sample autocorrelation and the subscript is an indicator of the lag time.

$$\beta = -\frac{b \pm \sqrt{b^2 - 4(r_1 - \alpha)^2}}{2(r_1 - \alpha)} \quad (\text{C-3})$$

where,

$$b = 1 - 2\alpha r_1 + \alpha^2 \quad (\text{C-4})$$

and

$$\gamma = \frac{s^2(1 - \alpha^2)}{(1 - 2\alpha\beta + \beta^2)} \quad (\text{C-5})$$

where s^2 is the sample variance.

This ARMA formulation was constructed to preserve the statistics and properties of the monthly time series. However, such model does not ensure that other important characteristics of the time series will be maintained. Two important characteristics that should be maintained are the 1) annual flow volumes, and 2) inter-annual monthly distribution. Adding these conditions as constraints on the model requires fine tuning of the ARMA parameters from the estimates obtained using the method of moments. In Table C-1 the ARMA(1,1) parameter values are provided.

Table C-1: The ARMA parameter values. The multiplier is a coefficient that is used to scale the normal distribution.

	Parameters			Multiplier
	α	β	γ	
Method of moments	0.74	0.53	0.12	
Tuned	0.85	0.64	0.18	1.35
1935-64	0.7	0.64	0.19	0.5
1965-2002	0.85	0.5	0.16	1.85

The ARMA model is a synthetic model that is built to maintain the persistence of the time series. However it has to be understood that the time series persistence is flow magnitude dependent and commonly stronger in the low flow. We also note that the statistical model developed is a valid representation of the monthly flows only (not the daily flows, as is the model in Chapter B).

C.3 Model results

In the following section we evaluate the ARMA simulations using the observed flow time series. In Figure C-6, the differences in the mean, standard deviation, skew coefficient and lag-1 correlation coefficient between the observed and 1000 simulations with the same record length (i.e. 67 years) are plotted. Differences are expressed as percentages of the observed values. Good performance of the model is signified by the cloud of points being centered on the zero value and having a small spread. We are most satisfied by the performance of the model with respect to the mean and lag-1 correlations. During the tuning process it became apparent that there is a tradeoff relationship between performance with respect to the standard deviation and the skew. Improvement in the standard deviation deteriorates skew coefficient performance. The selected parameters are thought to be a compromise, which slightly underestimates the standard deviation and the skew.

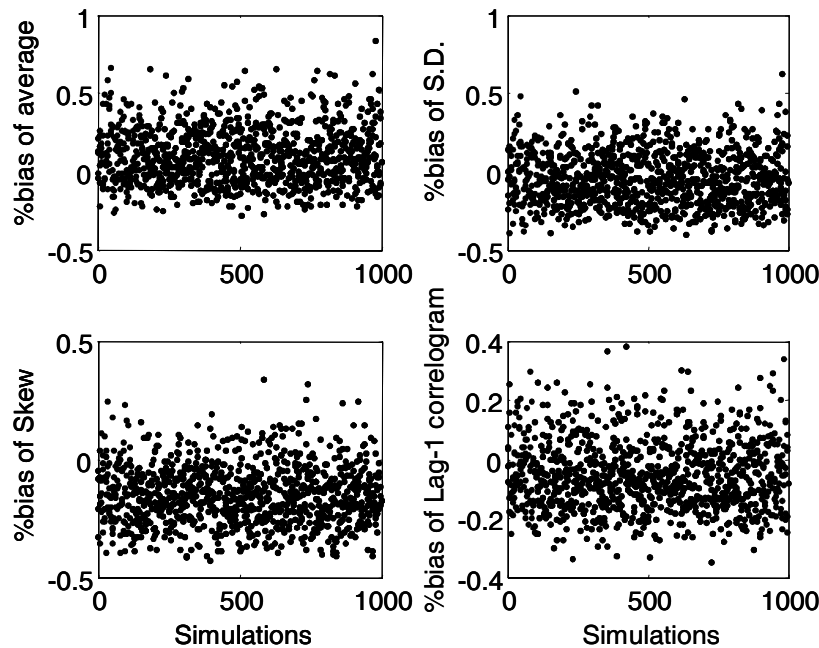


Figure C-6: Performance of the ARMA(1,1) simulations, Differences between the mean, standard deviation, skew coefficient and lag-1 correlation of the observed and 67-year long 1000 simulations. Differences are expressed as a percent of the observed values.

The synthetic hydrographs can be seen in Figure C-7. In this figure the upper panel is the observed and the other panels are selected synthetic simulations. Additional evaluation is provided in Figure C-8, in which we compare the distributions of 100 simulations of 67 annual flows to the annual flow distribution of the observation record. It can be seen that the simulation provides an envelope of uncertainty as well as some extreme values of

annual flow. An evaluation of the inter-annual distribution of the monthly total flow is provided in Figure C-9 for all 12 months of the year. Again, 100 simulations each with a length equal to that of the observed record are used to produce these plots.

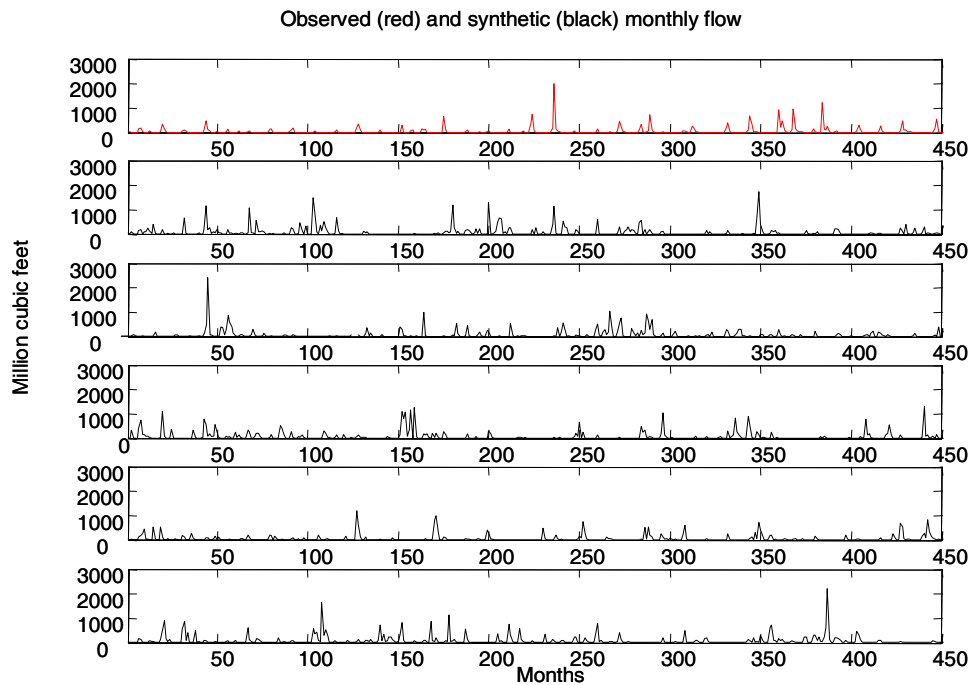


Figure C-7: Hydrographs of the observed (upper panel red) and synthetic (lower panels black) hydrographs. (Conversion: 1 AF = 43,560.25 ft³.)

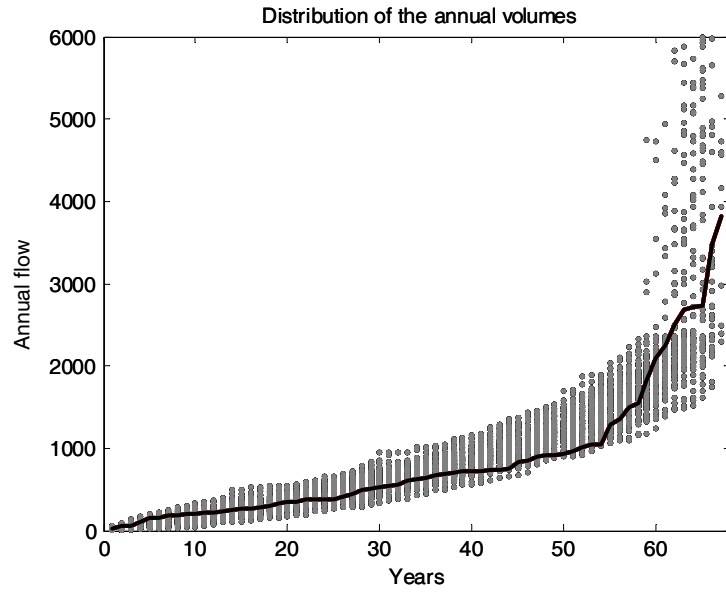


Figure C-8: The distribution of the observed (black) annual flow versus the annual flows of 100 synthetic simulations (gray dots).

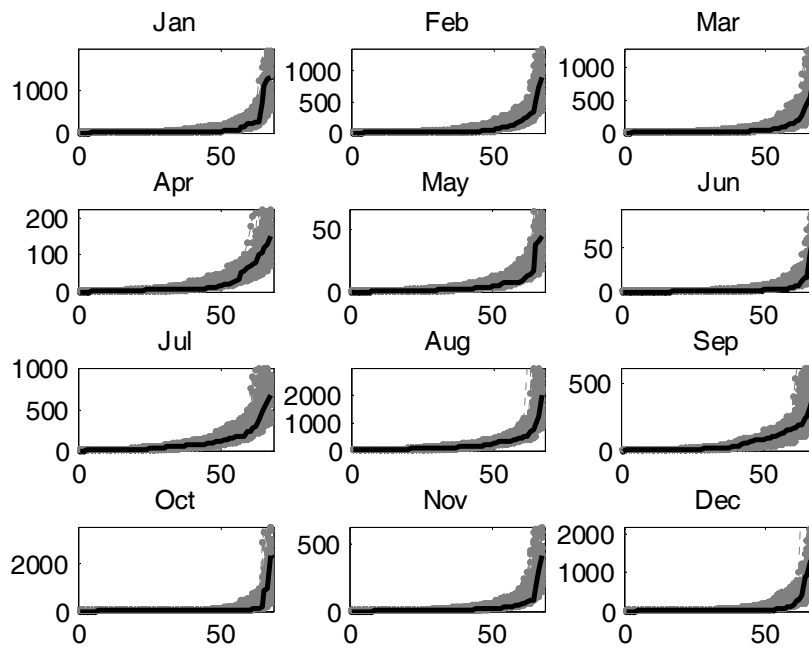


Figure C-9: Monthly inter-annual distribution of the observed flow (black) and 100 simulations (gray) of flow. Simulation record length is equal to the length of the observed record.

An analogous set of Figures is shown next for the ARMA model constructed for the part of the record with observed lower variability (1936-1964) and the part with larger variability (1965-2002). Model performance for the first part is presented in figures C-10 to C-13 and for the second part in Figures C-14 to C-17.

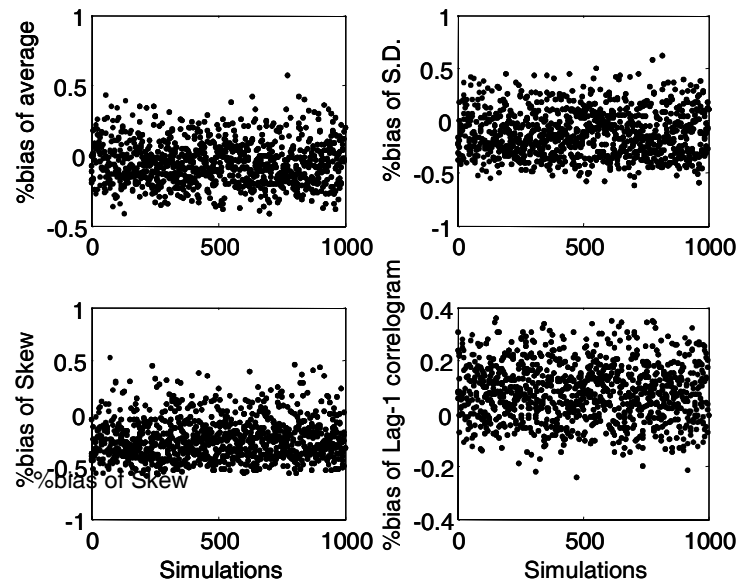


Figure C-10: As in Figure C-6 but for 1936-1964.

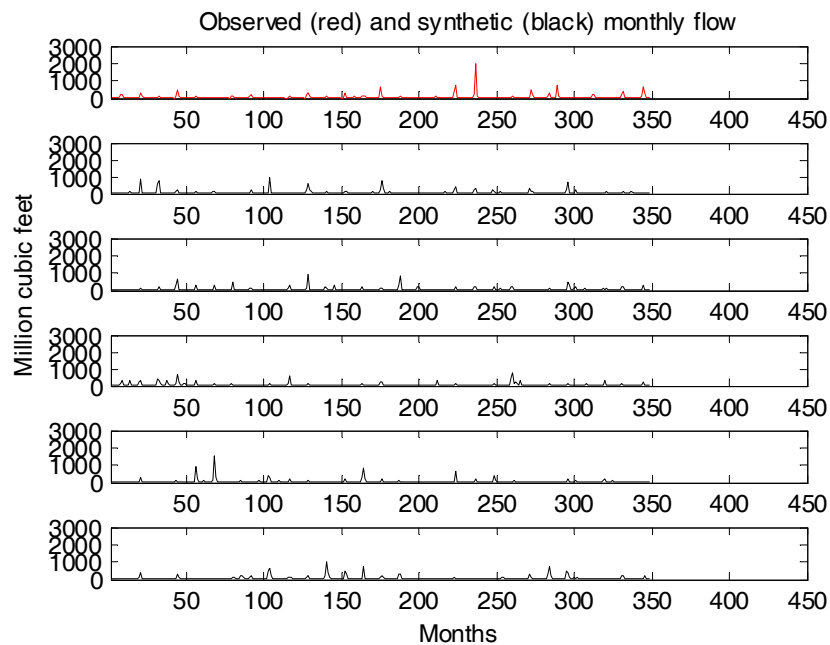


Figure C-11: As in Figure C-7 but for 1936-1964.

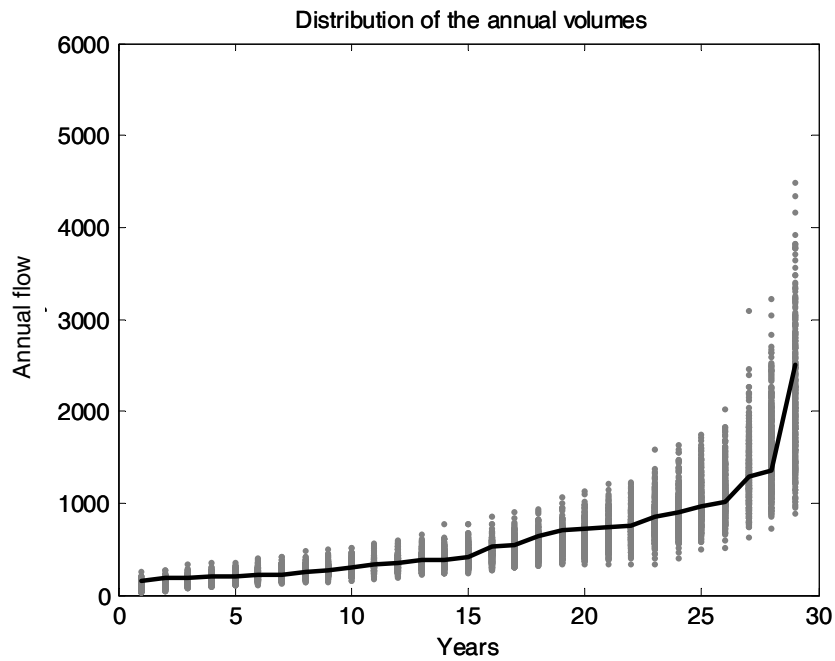


Figure C-12: As Figure in C-8 but for 1936-1964.

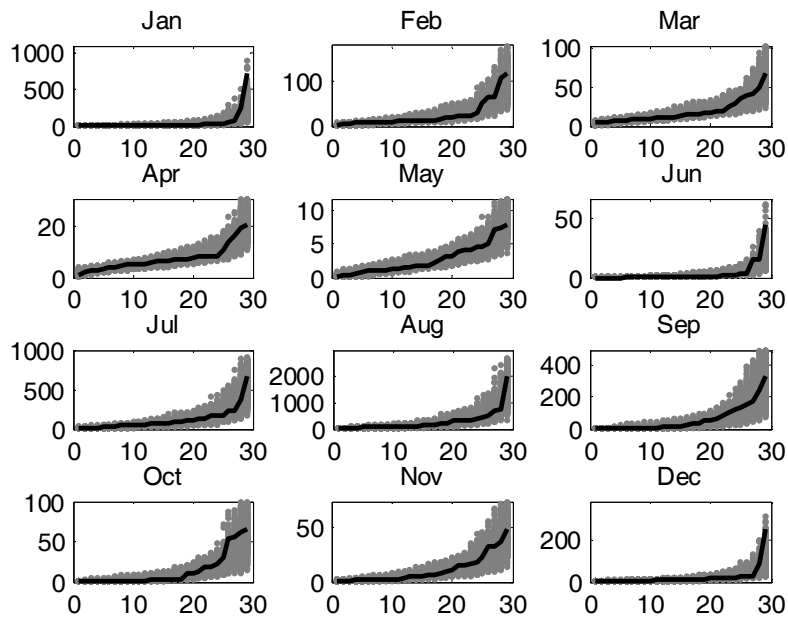


Figure C-13: As in Figure C-9 but for 1936-1964.

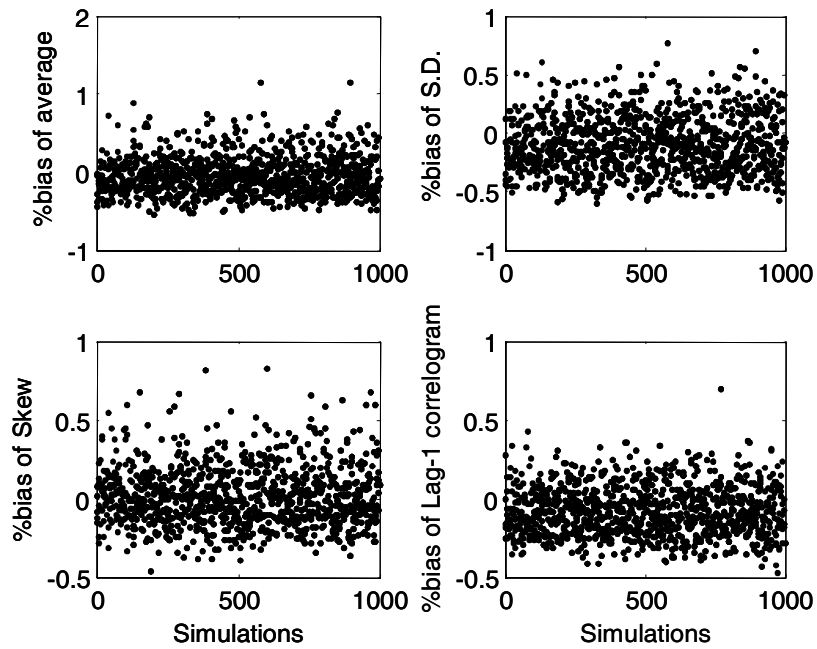


Figure C-14: As in Figure C-6 but for 1965-2002.

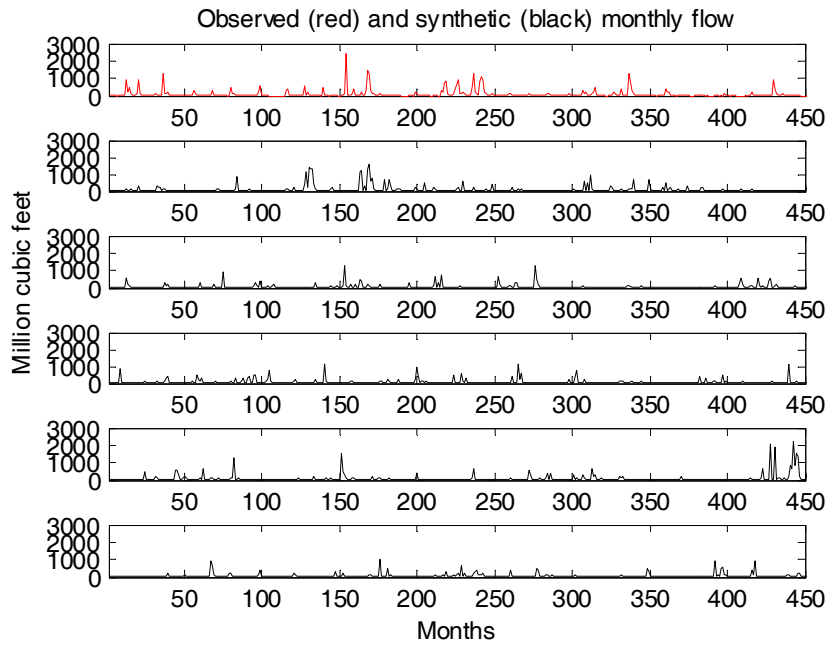


Figure C-15: As in Figure C-7 but for 1965-2002.

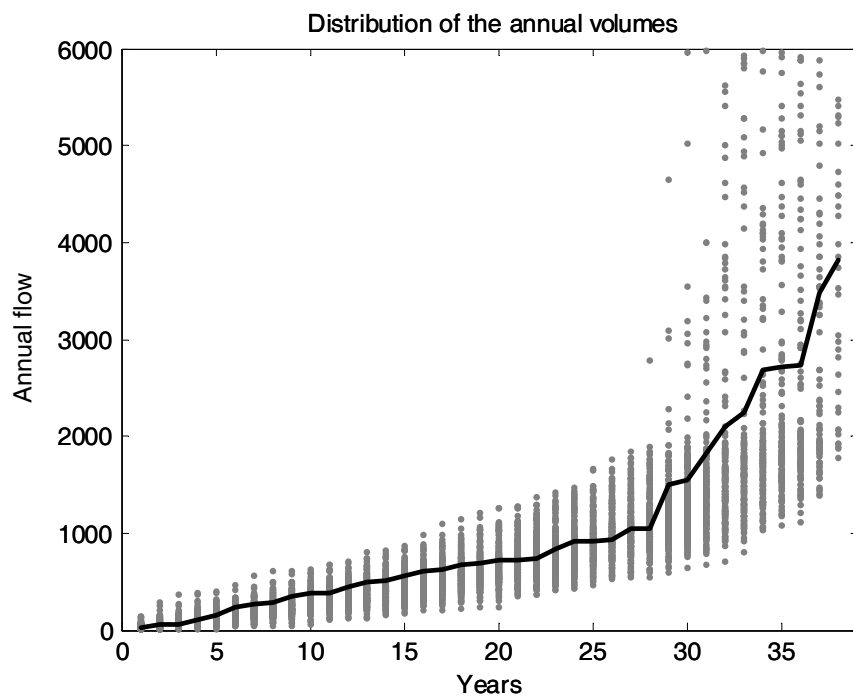


Figure C-16: As in Figure C-8 but for 1965-2002.

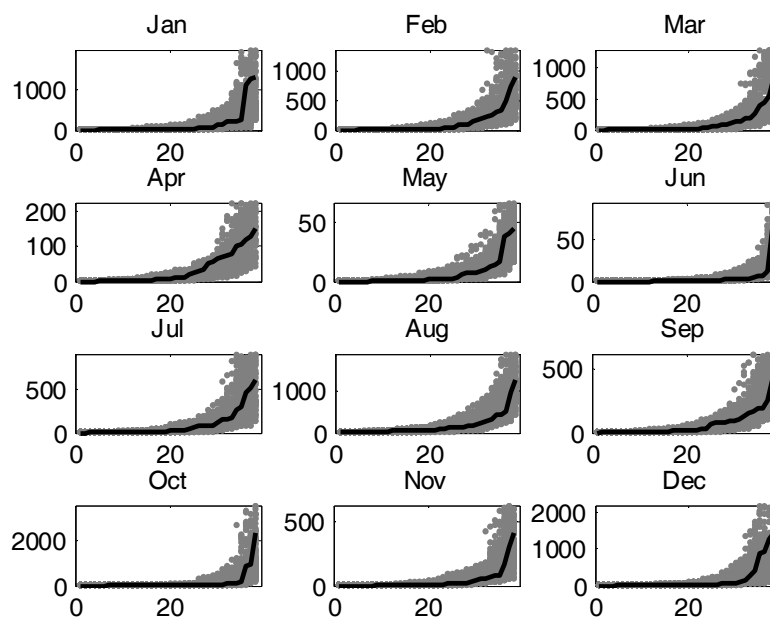


Figure C-17: As in Figure C-9 but for 1965-2002.

C.4 Relation between Volumes and ARMA Parameters

In order to relate the ARMA parameters to flow volumes that may be estimated for future periods on the basis of paleo-hydrologic or climate model data, in this section we determine relationships between the ARMA parameters, as estimated by the method of moments, and the average monthly flow. These relationships are shown in Figure C-18 using a 10-year moving average of flow. It can be seen that for the α and γ parameters (Eq. C-2 and C-6) there are apparent functional relationships that can be estimated by linear relationships. For parameter β a weaker relationship is observed but there is still a positive correlation with a correlation coefficient of 0.47.

The values of the linear regression coefficient (i.e., slope and intercept) and regression correlation coefficient for these flow-volumes versus ARMA-parameter relationships are provided in Table C-2.

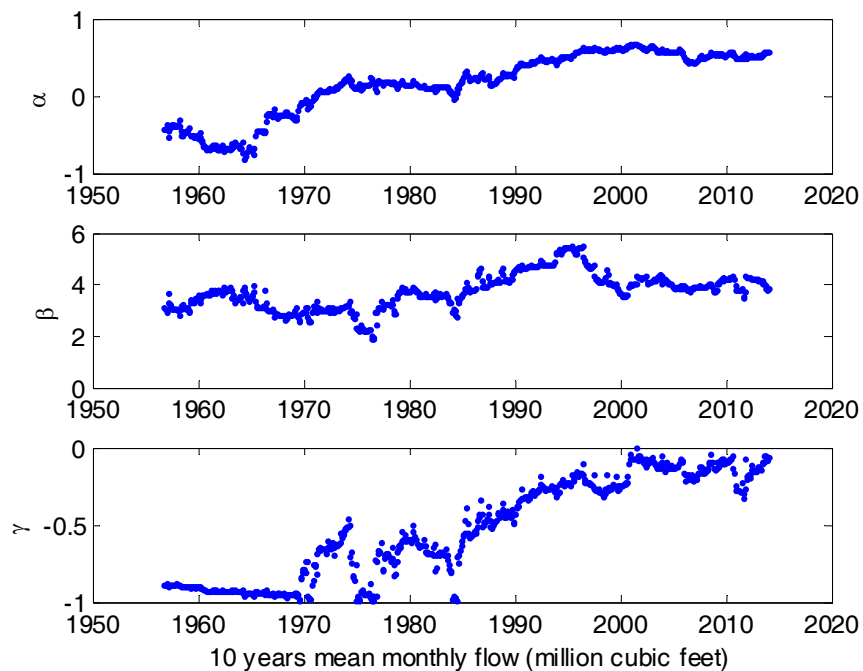


Figure C-18: ARMA parameters as functions of the mean monthly flow of a 10-year moving average for the observed record duration. (Conversion: 1 AF = 43,560.25 ft³.)

Table C-2: Linear regression parameters (slope and intercept) and the correlation coefficient of the estimation of the ARMA parameters from mean monthly flow volumes for a 10-year moving average.

	slope	Intercept	R
α	0.02	-44	0.90
β	0.002	3	0.47
γ	0.0015	-1	0.84

C.5 Inter comparison of the stochastic flow models

Statistics from the two stochastic models (i.e., the flow-based ARMA(1,1) and the precipitation-based model documented in Chapter B) are compared next. The models that were constructed from data having different time scales are compared on the seasonal and annual time scales. In Figures C-19 and C-20 we summarize the statistics of 100 realizations with record length 42 years for the precipitation and 68 years for the flow as Box plots (see Chapter B for the interpretation of Box plots). The observations are presented as the left most boxes, the ARMA(1,1) as at the right most boxes and the center boxes are for the precipitation-based model.

The features to note in these Figures are: 1) the models' median seasonal flow and the width of the boxes agree reasonably well with those of the observations; 2) the ARMA model, except from the Fall, generates extreme wet seasonal flows that are beyond the observed range; 3) on the annual time scale the model reproduce the median flow and extreme outlier values well but the models' boxes are wider than the observation box which indicates larger skew in the simulations.

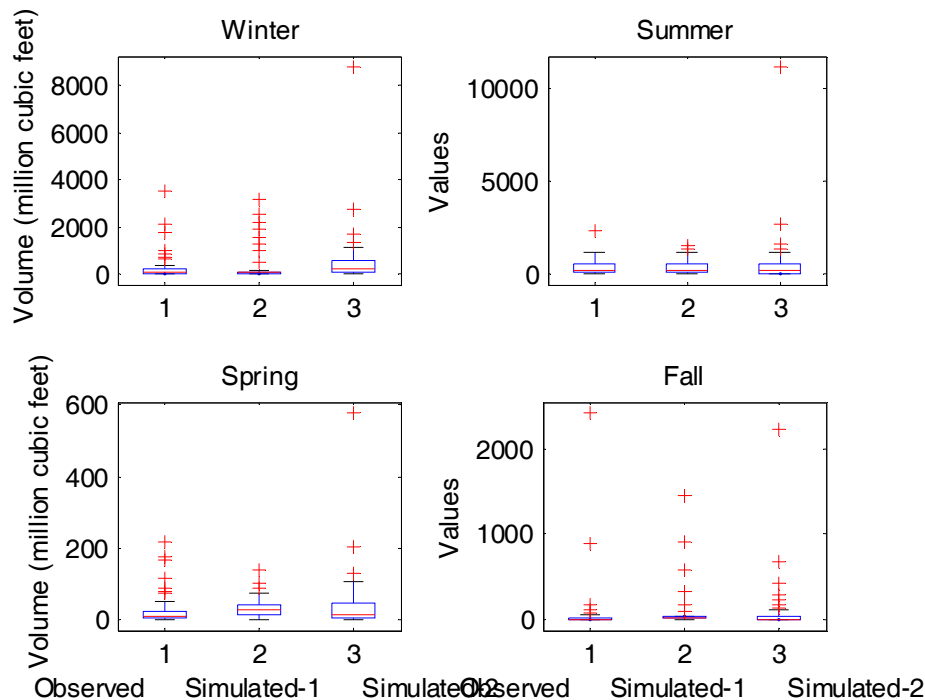


Figure C-19: Box plots that summarizes the seasonal statistics of the observed flow (left boxes), 100 realizations of precipitation-based model simulations (middle boxes) and 100 realizations of flow-based ARMA(1,1) model simulations (right boxes).

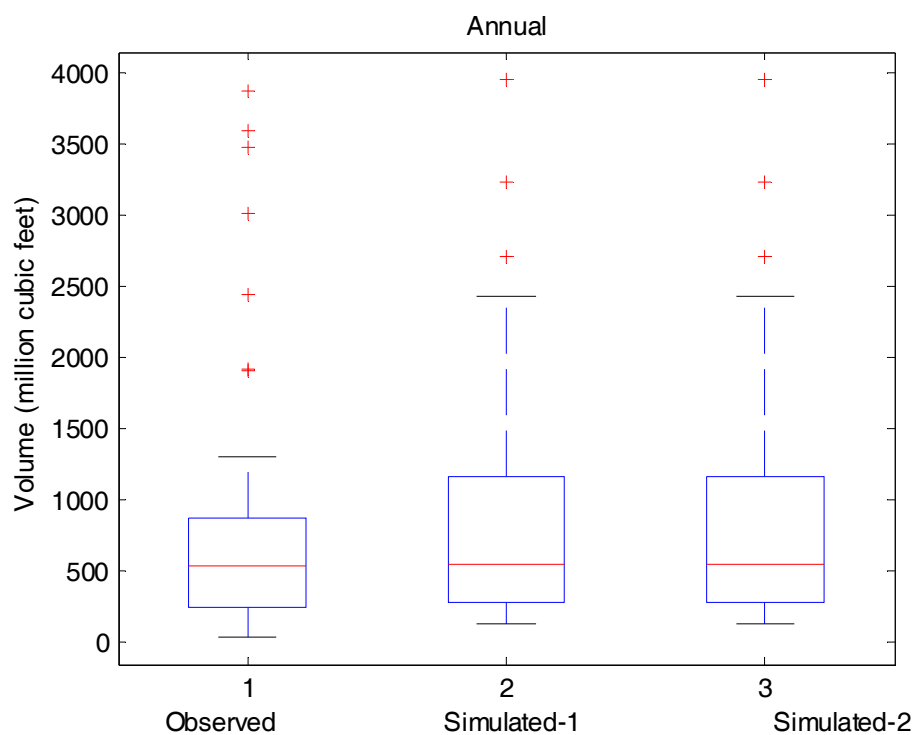


Figure C-20: The same as in Figure C-19, but for the annual time scale.

Chapter D

Streamflow Scenarios with Dendrochronology Information

In this Chapter we discuss the use of the stochastic precipitation model with inter-annual variability information derived from the dendrochronology reconstructed precipitation record. In this case, runs of the precipitation-flow model of Chapter B provide likely flow scenarios that maintain the intra-annual flow variability as observed in the streamflow-gauge record and the inter-annual variability of the dendrochronology reconstructed record. The results may be used to examine likely long-term flow trends and the time scales of drought in the region.

In practice the reconstructed precipitation which is valid only for the winter season is used to determine the winter categories of wet, medium, or dry. Since these winter categories were determined based on the annual flow (not precipitation), a statistical relationship between the annual precipitation and annual flow was established. The winter record of the tree-ring reconstructed precipitation was divided into quartiles and for each quartile the frequency of occurrence of a wet, medium or dry winter flow season was determined. These frequencies of occurrence for the different winter categories are presented in Table D-1. It can be seen that there are clear relationships between the categories and the total precipitation from the reconstructed record. For example, the wet winter flow category occurs only when the precipitation is in the fourth (highest) quartile and the dry winter flow category does not occur when the precipitation is in the fourth quartile. Moreover, the chance for a dry winter flow category to occur decreases with increasing precipitation quartiles. The dominant flow regime is in the medium winter flow category and occurs at about 56% of the years followed by the dry (27%) and the wet (16%) winter flow categories.

Table D-1: Winter flow categories and tree-ring reconstructed precipitation quartiles.

Winter flow categories	Precipitation quartiles from tree-ring record			
	1 st	2 nd	3 rd	4 th
Wet	0	0	0	0.625
Medium	0.5	0.69	0.75	0.375
Dry	0.5	0.31	0.25	0

One hundred realizations of the model, each 317 years long (length of tree ring reconstructed precipitation record) were generated. For each year the selection of the winter categories was made by Monte-Carlo sampling that used the frequencies of Table D-1.

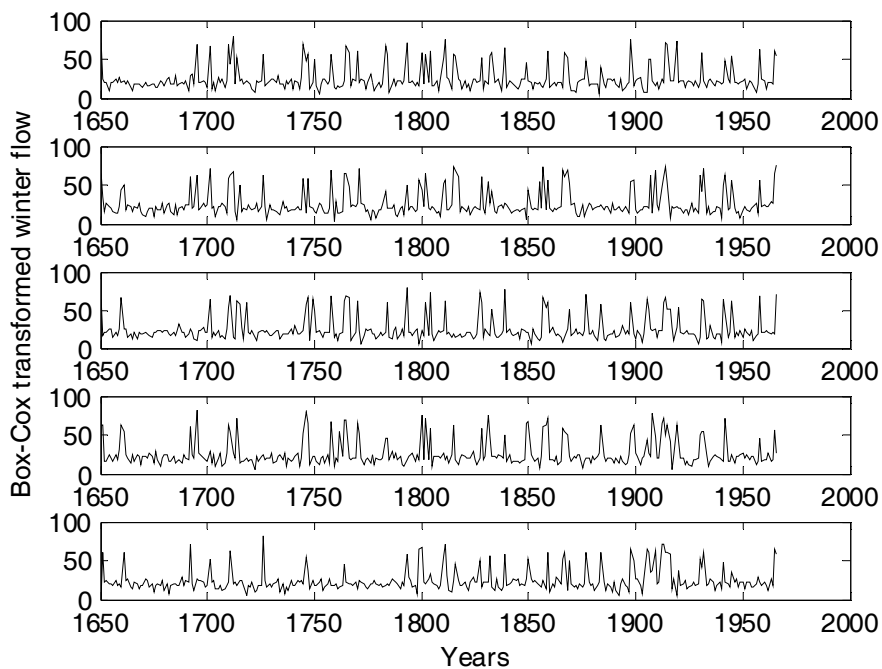


Figure D-1: Sample of 5 realizations of winter total flow for the duration of the tree ring record

Examples of generated winter flow (total season) are shown in Figure D-1. The flow values in this Figure were transformed using the Box-Cox transformation for clarity in low and high flow representation. These plots show that there are long (even centennial) periods with relatively low flow variability followed by frequent high flow years. A good example is in the upper panel. The first 50 years show low flows with very low variability while even the first 100 years only show about 4 periods of higher flows. After the first hundred years, the flow variability increases significantly with frequent periods of high flows to decrease again near the end of this generated record. This type of behavior suggests caution when inferences are only derived from the historical gauge record (record length of less than 100 years).

The effect of the long term memory of the flow wet, medium and dry categories is exemplified in Figure D-2. In this Figure, the cumulative departure of each realization from the realization's mean annual total flow (upper panel) and winter flow (lower panel) are plotted. The 5, 50 and 95 percentiles are marked in red. Negative gradients in this figure mean that the deficit from a given reference point is increasing while a positive gradient indicates that the surplus relative to the reference point is forming. Visual inspection indicates that in general the negative gradient of the median has longer stretches than the positive gradient. The periods of stress and deviation from the base reference are longer than the period of replenishments.

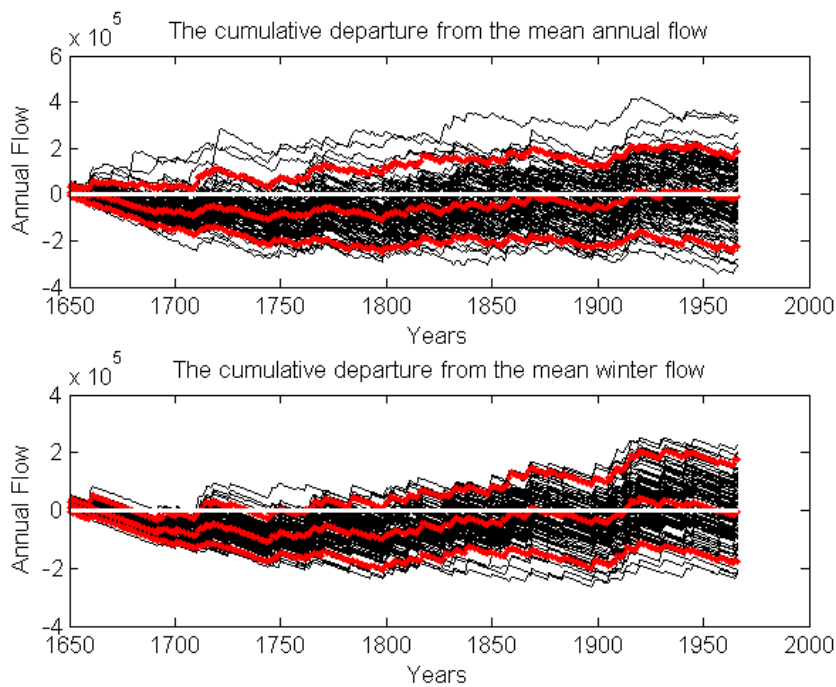


Figure D-2: Ensemble of 100 cumulative flow departures from the annual (upper panel) and winter (lower panel) flow means. The ensemble flows maintain the inter-annual variability in the dendrochronology reconstructed precipitation record. Red is for the 5, 50 and 95 percentiles of the ensemble.

The relationships between the PDO and El Nino – Southern Oscillation (ENSO) climatic indices and the winter flow categories were found weaker than the tree-ring reconstructed precipitation. The same method as described above for the winter precipitation was used to find the quartiles of total precipitation for the paleo-climatic record. The quartiles were then related to the flow record in a manner analogous to that in Table D-1. It was found that the dry and the wet total winter flow records are not strongly related to the first and fourth quartile, respectively. The dominant flow regime for all the quartiles is found to be the medium flow category. Therefore, there is not a strong signal for the extremes (wet and dry) that can be preserved by the stochastic simulation.

Chapter E

Cost-Loss Analysis for Santa Cruz Flows at Nogales

E.1 Introduction

The economic value methodology in this context is designed to associate user decisions that are based on ensemble streamflow forecasts with probabilities of occurrence of certain flow volumes replenishing the groundwater aquifers, and with expected costs and losses associated with actual streamflows and user actions. In this chapter we discuss a particular simple example of application for illustration purposes. For this application, define the event of interest, E , to be the occurrence of average annual streamflow at Nogales less than a given minimum target Q_T , which assures groundwater levels maintaining mandated values. If the average annual streamflow at Nogales is above this minimum target level, then no economic loss is incurred by the Santa Cruz Active Management Area (SCAMA). If on the contrary, the average annual flow at Nogales falls below Q_T , for the same pumping rates the groundwater mandated levels cannot be maintained and an annualized loss (L) is assumed to be incurred. The action that may be taken by SCAMA to prevent this loss is the control of the real estate development and associated pumping in the region at an annualized cost (C). These annualized costs and losses are estimated over a set decision horizon, which, in this example, is equal to 100 years.

The economic analysis of the example of this section is significantly simplified to illustrate the cost-loss methodology, and the results obtained are more qualitative than quantitative. For instance, a regional ground water model may be used, forced by the generated ensemble streamflow sequences at Nogales to produce generated groundwater levels anywhere within the SCAMA region. In such case, the event of interest would involve the groundwater levels themselves. Also, annualized losses and costs are used for simplicity. The feasibility of computation of such simple economic measures is a significant assumption of this analysis and further work is needed to define appropriate economic indicators associated with the costs and losses of preventing or allowing development in the region. In spite of these caveats, the following analysis may be useful to assign a measure of utility to the generated likely future streamflow scenarios, and to examine the degree of sensitivity to the target streamflow level Q_T .

E.2 Formulation

Based on the ensemble annual average flow, the probability of occurrence of the event E , p , may be computed as the relative frequency of the ensemble members for which the event E occurs. In this manner, so far, the user has utilized the ensemble simulations of inflow produced by the stochastic model of the previous chapters to obtain estimates of

the probability of occurrence of the potentially costly event E . The next step in the formulation is to develop a user rule for deciding whether to act or not on the basis of the ensemble streamflow simulations. “Act” in this example pertains to allowing further exploitation of regional groundwater resources, which inevitably comes with new development. The user rule may be obtained in a simple manner through the use of a threshold of probability p_o , so that the user decides to act (not allow further development) when $p > p_o$. For a given p_o , we may then define the user decisions and actions. Furthermore, and following well established cross validation practice (e.g., *Räisänen and Palmer 2001*) for ensemble simulations, we may also define the relative frequency of correct and incorrect decisions/actions for each case as shown in the contingency Table E-1.

Table E-1: Contingency Table for Decisions/Actions versus Observations.

Decisions/Actions		YES	NO
Observations	YES:	Hit ($h(p_o)$); Cost (C)	Miss ($m(p_o)$); Loss (L)
	NO:	False Alarm ($f(p_o)$); Cost (C)	Correct Rejection ($r(p_o)$)

The relative frequency of a correct decision to not allow further exploitation of groundwater resources when in fact the event E occurs (a hit) is denoted by $h(p_o)$, that of an incorrect decision to allow further exploitation when in fact the event occurs (a miss) is denoted by $m(p_o)$, that of an incorrect decision to not allow further exploitation of groundwater resources when in fact the event does not occur (a false alarm) is denoted by $f(p_o)$, and that of a correct decision to allow exploitation when in fact the event does not occur (a correct rejection) is denoted by $r(p_o)$. Each of these cases has an associated cost or loss as shown in the Table. A hit and a false alarm have a cost associated with the act to not allow exploitation of groundwater resources (C), while a miss has a loss associated with significant revenue reduction (L). No cost or loss is associated with a correct rejection. It is noted that in this work for simplicity of the formulation we do not take into consideration a mitigated loss when the exploitation is not allowed and it is warranted by the observed inflow deficit condition, under the presumption that not allowing exploitation prevents the loss of revenue completely. A formulation suitable for problems for which mitigated loss is necessary is given in *Zhu et al. (2002)*. It is true by definition that the sum of the four relative frequencies h , f , m , and r is equal to 1, and that the sum of h and m is equal to the climatological frequency (o) of the annual average streamflow being less than Q_T .

For the aforementioned definitions and the nomenclature of Table E-1, we may now obtain expressions for the expected expenses of the user under natural annual average streamflow variability and for a given decision threshold probability p_o . The expected expense, $M_{ens}(p_o)$, of a user of the ensemble average annual streamflow simulations is:

$$M_{ens}(p_o) = h(p_o)C + f(p_o)C + m(p_o)L \quad (\text{E-1})$$

where the annualized costs (C) and losses (L) are used.

It is natural to compare the expected expense of using the generated ensemble information with that of using climate information on the basis of the historical record alone. The user of climatological information regarding annual average streamflow has the expected expense, M_{cli} :

$$M_{cli} = \min\{oL, C\} \quad (E-2)$$

where, between the two terms within angular brackets, the function $\min\{ \}$ selects the term with the lower value. Thus, the user of climatological information will opt to make a decision not to allow groundwater exploitation if the cost C is low compared to (oL). Estimation of the measures M_{ens} and M_{cli} for the generated ensemble of 100 100-year streamflow realizations and for several values of Q_T indicated that the value of the expected expense (M_{ens}) of the generated ensemble is equal to that theoretically estimated in Equation (E.2), when the value of p_o is selected in an optimal manner (see discussion below).

The expected expense, M_{per} , associated with a perfect streamflow forecast over the decision horizon is:

$$M_{per} = oC \quad (E-3)$$

It provides a lower bound on the expected expense and comparison of other expected expenses (e.g., by using ensemble simulations) indicates available room for improvement.

Using these expected expenses, a relative measure, $V(p_o)$, of economic value for the user of the ensemble streamflow simulation information may be obtained as:

$$V(p_o) = \frac{M_{ens}(p_o) - M_{per}}{M_{per}} \quad (E-4)$$

and it describes the relative increase in expected expense over and above the least possible such expense attained with perfect information. The ratio $V(p_o)$ is positive and it is equal to zero only if the ensemble contains perfect information.

The relative economic measure V of Equation (E-4) is a function of the decision threshold probability p_o . It is in the best interest of the user of the ensemble streamflow simulations to select the value of p_o that *minimizes* the relative economic value (i.e., $V = \min\{V(p_o)\}$ w.r.t. p_o). The optimal p_o may be found through optimization of the relative economic value V given by Equation (E-4). As the actual threshold probability that the user may use to convert relative frequencies of event occurrence to decisions may differ from the optimal choice, the relative economic value obtained by minimizing $V(p_o)$ is considered a

potential economic value index, achieved when the user of the operational forecasts makes an optimal choice for p_o .

The formulation presented allows the development of a formula for V that depends on the cost-loss ratio (C/L) rather than on C and L . Simple algebraic manipulations of Equation (E-4) on the basis of Equations (E-1) and (E-3) lead to:

$$V = \min_{p_o} \left\{ \frac{(h(p_o) + f(p_o) - o) \frac{C}{L} + m(p_o)}{o \frac{C}{L}} \right\} \quad (\text{E-5})$$

where now dependence is on the cost/loss ratio (C/L). Plotting V versus (C/L) allows the determination of a quantitative measure of the relative economic value of the generated streamflow simulations as a function of a range of values of C/L (dimensionless cost/loss ratio) and for various values of the target annual average streamflow Q_T .

E.3 Results

At first we select a range of target annual average streamflow values for Nogales on the basis of the observed distribution of annual average streamflow and the degree to which the generated ensemble reproduces this distribution. Figure E-1 shows the sample cumulative frequency distribution function of observed annual average streamflow (red line) estimated from 67 years of data. The Figure also shows the 100 sample cumulative frequency distribution functions of generated annual average streamflow (blue lines) estimated from 67 years of data. It is apparent that the observed and generated distributions are very similar, with the observed curve contained within the ensemble of generated streamflow curves for all the annual average flow values but for the range 5 – 20 cfs, for which the generated flows have higher cumulative frequencies than the observed flow. To use values of the target streamflow from the regions of overestimation and matching of cumulative frequencies of observed and generated flows, the cost-loss analysis was performed for the following Q_T values: 10, 20, 30, 40 cfs. The sample cumulative frequency values for these flows are given in Table E-2.

Table E-2: Sample Cumulative Frequencies for Q_T values

$Q_T(\text{cfs})$	Observed CF	Range of Generated CF
10	0.27	[0.3 – 0.4]
20	0.48	[0.5 – 0.65]
30	0.73	[0.65 – 0.85]
40	0.81	[0.7 – 0.9]

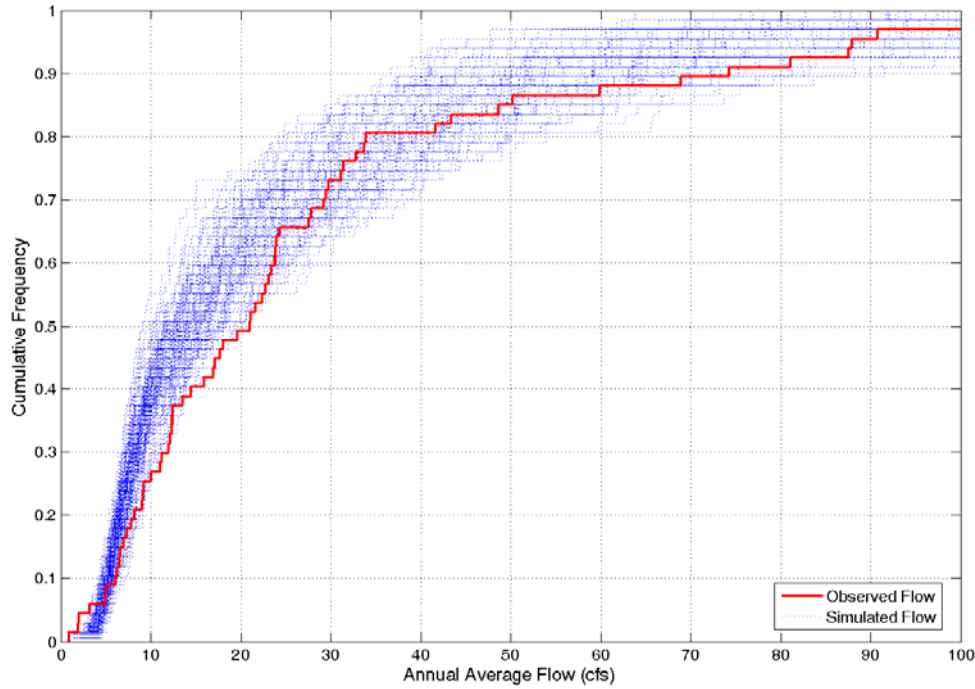


Figure E-1: Sample cumulative distribution functions of observed (red) and an ensemble of 100 generated (blue) annual average streamflows at Nogales, Arizona. Sample size is 67 years.

The results of the cost-loss analysis are shown in Figure E-2. The upper panel shows the expected value of the M_{ens} (see Equation (E-1)) over all the ensembles and over the 100-year decision horizon and the expected value of M_{per} (see Equation (E-3)) computed using each generated ensemble member of annual average flow time series in turn as truth. Both values are normalized by the annualized loss L . These computations are made for a range of values of the cost-loss ratio (C/L) from 0.1 to 0.9 and for the four selected values of Q_T . The results indicate that for low (C/L) ratios the expected expense of a user of the generated ensemble that uses an optimal p_o to make decisions is in absolute value small compared to that corresponding to higher ratios. It is also interesting to note that the least possible expense due to perfect information (M_{per} normalized by L) increases as Q_T increases because of the increasing frequency of occurrence of the event E .

The lower panel in Figure E.2 shows the potential relative economic value index V (expressed in %) for an optimal choice of p_o and for various values of Q_T . The potential relative economic value of the generated ensemble is higher (index V is lower) for higher Q_T values and for higher (C/L) ratios. For instance, the results indicate that the percent increase from the perfect information expense is 50% for $Q_T = 30$ cfs and for ratios (C/L) from 0.1 to 0.68.

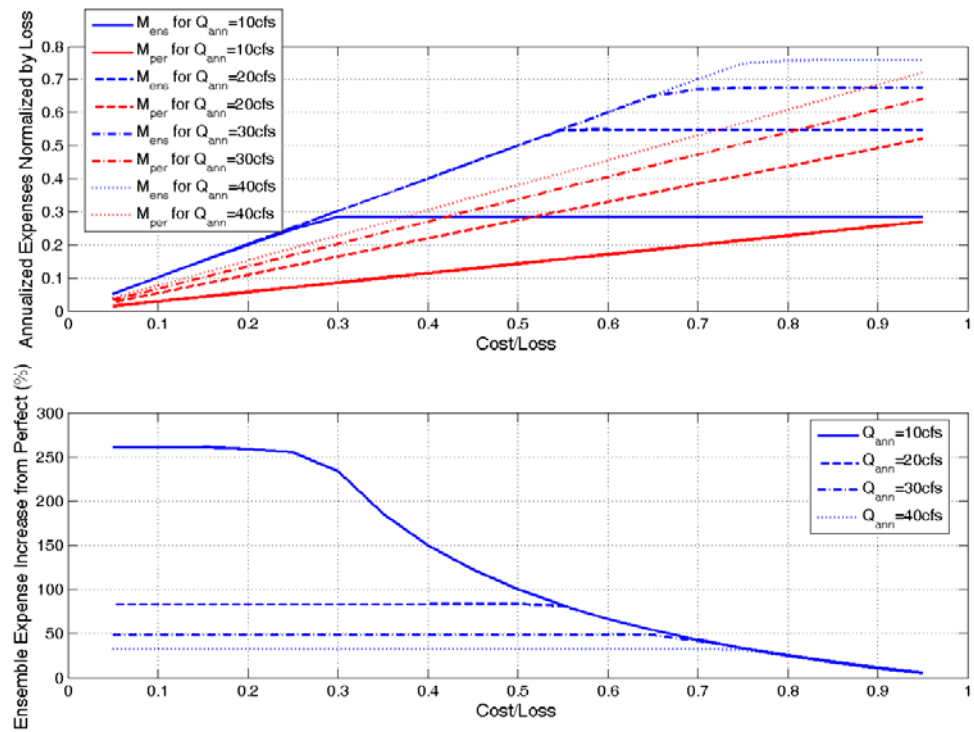


Figure E-2: Expected annualized expenses M_{ens} (blue) and M_{per} (red) for various target Q_T levels for a 100-year decision horizon (upper panel) and relative economic measure V for optimal choices of p_o and for various Q_T thresholds (lower panel).

Chapter F

Simplified Conceptual Groundwater Model for Santa Cruz River Microbasins

F.1 Introduction

The Arizona Department of Water Resources (AZDWR) implemented and runs a detailed groundwater model that simulates changes in groundwater levels for the southern four microbasins (i.e., Buena Vista, Kino Springs, Highway 82 and Guevavi). This model is referred to (hereinafter) as the AZDWR-Microbasins Groundwater Model (AZDWR-MGM). The AZDWR-MGM performance was validated using index wells that are located in the microbasins for the period of October 1997 – September 2002 (Erwin, 2003). Figure F-1 shows the geographical configuration of the microbasins and the location of the index wells.

The execution of the AZDWR-MGM model requires extensive data preparation steps and long computer run times. Therefore, at present, the efficient processing of ensemble-type input of long durations presents significant challenges. In recognition of the AZDWR-MGM run-time limitations and to illustrate the use of the generated flow ensembles in groundwater studies, HRC developed a simplified groundwater flow microbasin model (SGMM) to simulate groundwater level response to recharge, pumping and evapotranspiration in the four microbasins. An important and valuable feature of the SGMM is that it allows for rapid groundwater evaluation of surface water flow realizations without the long run times or potential numerical instability associated with running the AZDWR-MGM. The SGMM provides for the rapid evaluation of hundreds (or even thousands) of realizations and lends itself readily to initial assessments of risk and reliability analysis. However, because the SGMM is not explicitly a physically-based model constrained to Darcy's Law, the model's potential to evaluate certain aspects of the system will obviously be more limited and less flexible than the AZDWR-MGM.

In this chapter, we describe the SGMM, which was developed to mimic the volumetric microbasin response of the AZDWR-MGM and to be used in conjunction with simulations from the surface water model in ensemble mode and for long periods. The SGMM was created with input from AZDWR personnel who provided the fluxes and parameters from a five year simulation produced by the AZDWR-MGM.

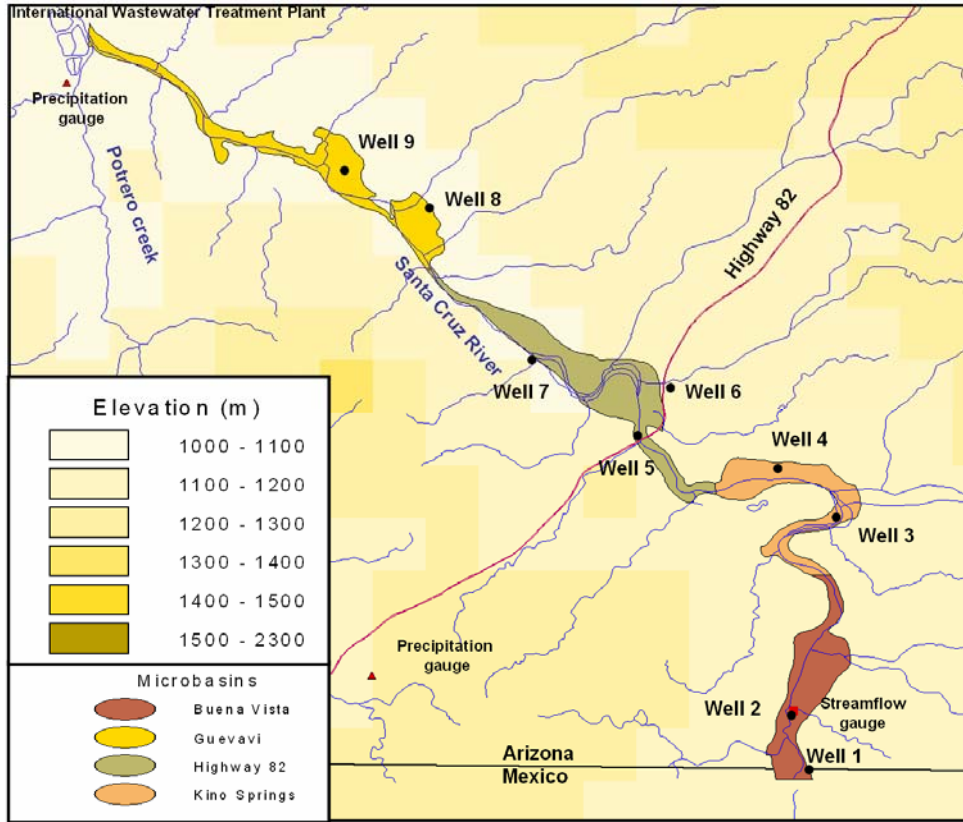


Figure F-1: Geographical locations of the microbasins and the index wells used in this study. The delineation of the microbasins is estimated by the areal extent of the younger alluvium formation.

F.2 Model Formulation

The SGMM uses a monthly time step and four reservoirs to simulate the four microbasins (Figure F-1) in a spatially-lumped manner. These conceptual reservoirs are assigned effective parameter values and are defined in series receiving recharge from the flow of the Santa Cruz River. For these reservoirs a mass balance equation is posited,

$$S_{i,j} = S_{i-1,j} + I_{i,j} - P_{i,j} - ET_{i,j} \quad (F-1)$$

where the subscript i represents the time step, and j is the reservoir number ($j = 1, \dots, 4$), $S_{i,j}$ is the reservoir content (state of model) j at the end of time step i , I is the infiltration replenishment from the stream into the reservoirs, P is the pumpage withdrawal from the reservoirs, and ET represents losses due to evapotranspiration over the surface area of the microbasins. It is noted that subscript i for fluxes indicates fluxes during time step i .

The infiltration (I) in Equation (F-1) is estimated as a function of the river flow (Q). It is done by relating the flow discharges to the average wetted width (B) of the stream within the river channel, as follows:

$$B_{i,j} = \alpha_j \exp(Q_{i,j}) + \beta_j \quad (\text{F-2})$$

where α and β are estimated coefficients. The potential infiltration capacity into the reservoirs (Ip) is estimated as:

$$Ip_{i,j} = B_{i,j} Kz L_j \quad (\text{F-3})$$

where Kz is the potential infiltration rate which is set equal to 2 feet per day for the relevant river segment, and the L is the channel length in each microbasin. In cases that $Ip_{i,j}$ is smaller than the difference between the capacity ($S_{o,j}$) of the reservoir and the storage of the reservoir after losses have been subtracted ($S_{i-1} - P_i - ET_i$), then,

$$I_{i,j} = Ip_{i,j} \quad (\text{F-4})$$

otherwise,

$$I_{i,j} = S_{o,j} - S_{i,j} + P_{i,j} + ET_{i,j} \quad (\text{F-5})$$

The flow at the inlet of the downstream channel that overlays the next reservoir is,

$$Q_{i,j+1} = Q_{i,j} - I_{i,j} \quad (\text{F-6})$$

The ET flux in Equation (F-1), is calculated as a function of the Depth to Water (DTW). The DTW was obtained as a linear function of the relative saturation of the reservoirs ($S_{i,j}/S_{o,j}$). The intercept and coefficient of this linear relationship are determined as special cases of the DTW when the relative storage is 0 or 1.

The ET is determined as:

$$ET_{i,j} = ETp_{i,j} (1 - DTW_{i,j} / DTW_{o,j}) \quad (\text{F-7})$$

where the ETp are potential monthly ET values and DTW_o is the maximum DTW for which there is ET .

F.3 Parameter Estimation

The estimated parameters for the model and other basin characteristics are provided in Table F-1. We calibrated the model to match the AZDWR-MGM model output for the period 1997-2002. The SGMM parameters were estimated for a monthly time step and, probably, need to be adjusted if simulations at different time steps are conducted. It was also apparent that during this simulation period changes in the reservoir volumetric contents do not represent the full range of the reservoir capacity for all four reservoirs. For example, for Buena Vista's reservoir the relative storage was higher than 80% throughout the simulation period. Therefore, we must acknowledge that such a limited record introduces large uncertainty into the estimated parameters.

The potential capacities of the reservoirs ($S_{o,j}$) are estimated as the maximum storage capacity of the four microbasins $[(area) \times (basin\ depth) \times (specific\ yield)]$. These values were obtained as averages of the younger alluvium and the combined younger and older alluvium as calculated by the AZDWR-MGM for October 2000. During this period, there were about 15 days of flow in the river and the groundwater levels at the microbasins were the highest among those obtained during the simulation period. It is noted that the estimated reservoirs capacities are likely on the low side as they do not include water that may be extracted by plant roots.

In Figure F-2 the SGMM output of relative changes in the reservoirs is compared to AZDWR-MGM output. The fluxes (I , P , and ET) that were used in the SGMM were calculated by the AZDWR-MGM. This comparison is done for the period of October 1997 - September 2002. It can be seen that the simplified model is doing well in replicating the changes in the relative storage as compared with the AZDWR-MGM.

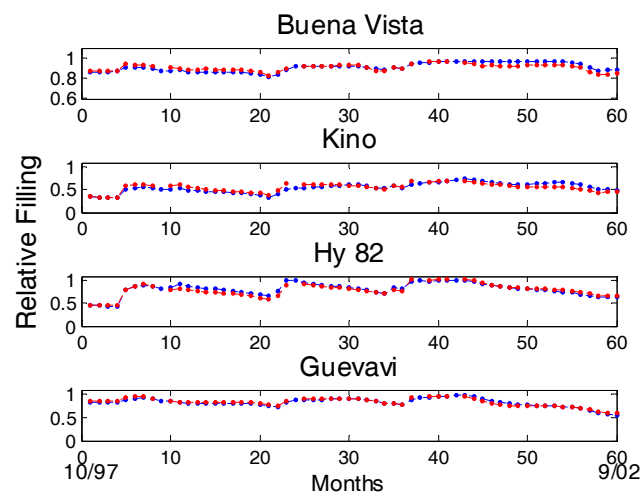


Figure F-2: Comparison of the relative volumetric content of the microbasins between the AZDWR-MGM (red) and the SGMM model (blue). The fluxes (infiltration, ET and pumpage) for the simulation period for both models are from the AZDWR-MGM.

Table F-1: Basin characteristics and parameters

	Buena Vista	Kino Springs	Hy 82	Guevavi
Basin area (acre)	1172	852	1573	1473
Basin storage (acre / ft)	2737	4018	5912	7948
Channel length (ft)	13507	20423	26353	15229
	Infiltration parameters			
α	0.5	1.4	3.7	3.45
β	-0.57	-7.6	-3.35	-4.3
	Storage to DTW			
Slope	-59.7	-74.2	-46.1	-58.8
	Potential ET (ft/month)			
April	0.01	0.008	0.009	0.016
May	0.083	0.07	0.08	0.12
June	0.18	0.15	0.15	0.24
July	0.17	0.14	0.15	0.24
August	0.15	0.12	0.14	0.21
September	0.085	0.07	0.08	0.12
October	0.02	0.016	0.02	0.03
November	0.002	0.0015	0.002	0.003

The potential monthly rates of *ET* were obtained from AZDWR-MGM and are dependent on land cover classifications. For the application of the SGMM, the potential rates of *ET* were calculated as a weighted arithmetic mean of the distributed potential *ET* values. These values represent the entire surface area of the basin and not only the riparian zones along the alluvial channel. To get the potential *ET* the rate is multiplied by the basin surface area, which was also retrieved from the AZDWR-MGM setup.

Estimates for the model depth to water (*DTW*) are obtained from linear regression equations that relate the *DTW* to the relative volumetric content in the reservoirs. In Figure F-3, the relationships between the *DTW* and the relative reservoir storages as calculated by the AZDWR-MGM are presented. The *DTW* in this figure is an average of the pixels in the inlet and outlet of the reservoirs.

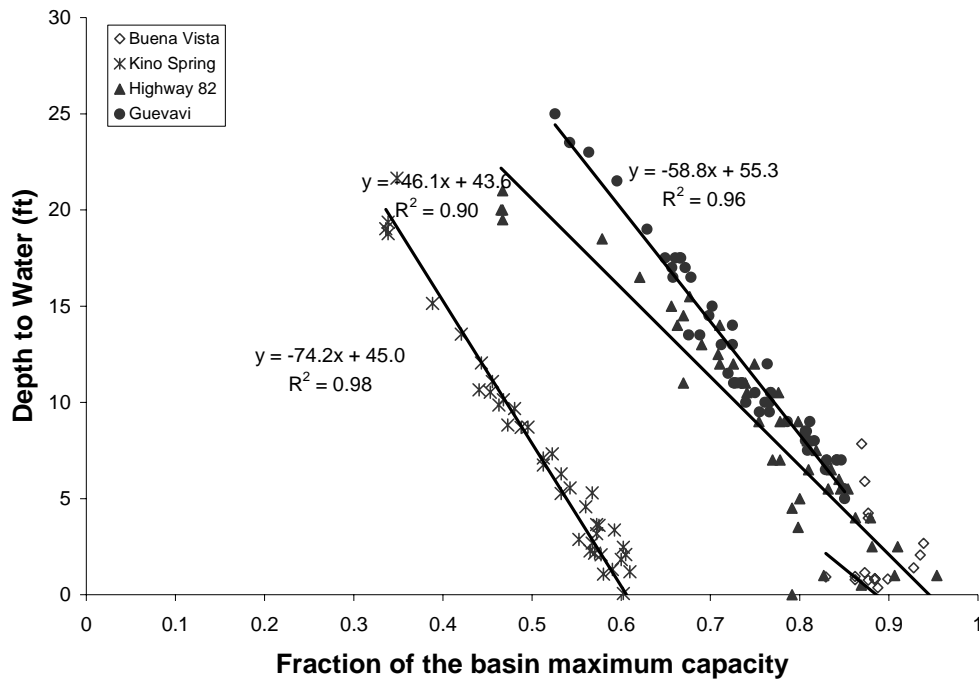


Figure F-3: The mean reservoir Depth to Water (*DTW*) as a function of relative volumetric water content computed by the AZDWR-MGM.

The Figure shows the clear linear relationships between depth to water and the average storage in the basins for all the basins except from the Buena Vista basin. For this basin during the simulation period, the water level and storage remain high, which does not provide enough spread for the development of the regression equation. The regression used for this basin utilizes the mean of the other-basin regression slopes. For the other basins and because the simulation period has not exploited the full range of their water storage, we are posing the assumption that the relationship between storage and water level holds for the whole range of water levels. The DTW_0 is the *DTW* for which the reservoir content is 30% of the capacity.

In Figure F-4, again, we used the fluxes from the AZDWR-MGM to force the SGMM, except from the *ET* flux, which was dynamically calculated as explained above (see Equation (F-7)). It can be seen that the proposed procedure produces results in good agreement to those produced by the AZDWR-MGM.

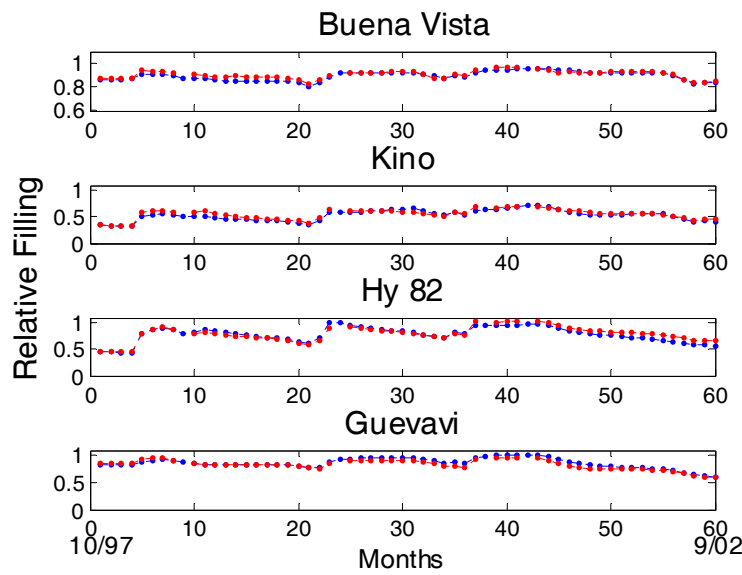


Figure F-4: Comparison of the relative volumetric content of the microbasins estimated by the AZDWR-MGM (red) and the SGMM models (blue). The *ET* in the SGMM was calculated dynamically as explained in the text.

The infiltration coefficients were estimated by trial and error for these 5 years using the fluxes from the AZDWR-MGM and the dynamic estimate of the infiltration from the observed flow at the Nogales gauge. In Figure F-5, a comparison of changes in storages between the two models is presented. It can be seen that there is good overall agreement between the models. Disagreement between the models exists in Kino Springs and Highway 82 during the winter of 2000/2001 (start at step # 36). During this period, high flow exists in the channel (Figure F-6), and the water content for SGMM is increasing while the water content for the AZDWR-MGM is decreasing. This difference is the result of the water content state difference between the two models in Kino Springs during the 2000/2001 winter. In the SGMM the water content is below the assigned reservoir capacity and in the AZDWR-MGM the model cells that correspond to Kino Springs are saturated. Therefore infiltration is observed in the SGMM and not in the AZDWR-MGM during the flow events of 2000/2001 winter. This might be a case in which the simplified areal lumped modeling approach cannot capture the high resolution spatial processes. The reservoir capacity in this basin based on the specific yield as described above is a dynamic variable that depends on the dynamics of flow within the basin's boundaries and not a static parameter as used in SGMM.

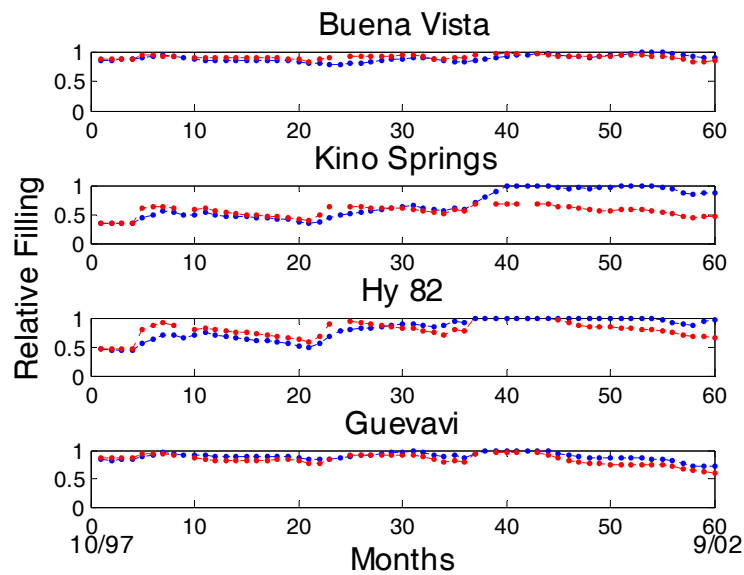


Figure F-5: Comparison of the relative volumetric content of the microbasins estimated by the AZDWR-MGM (red) and the SGMM models (blue). The infiltration at the SGMM was calculated dynamically as explained in the text.

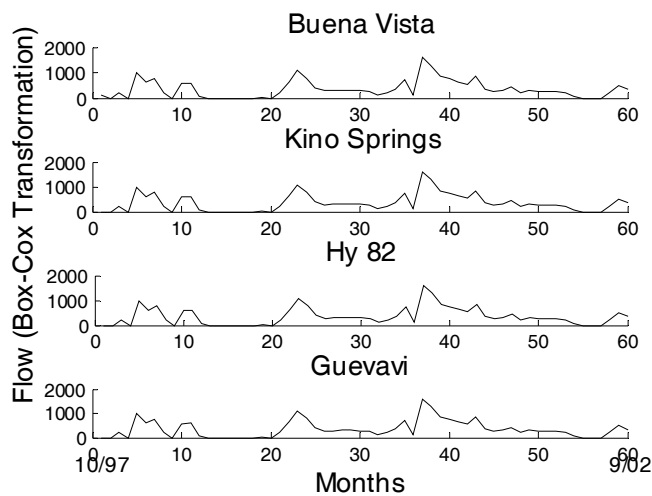


Figure F-6: Monthly Box-Cox transformed flow at the inlet of the microbasins. Note the high flow values that start at time step 36 (October 2000).

Last, we evaluate the SGMM model performance using dynamic estimates of both *ET* and infiltration fluxes (Figure F-7). This condition is used when SGMM runs with forcing

of future likely streamflow scenarios. The SGMM in this simulation maintains good agreement with the AZDWR-MGM. One notable mismatch between the models is again in Kino Springs during the winter of 2000/2001. In this period the full reservoir conditions in the SGMM created high *ET* rate that corresponds to small DTW.

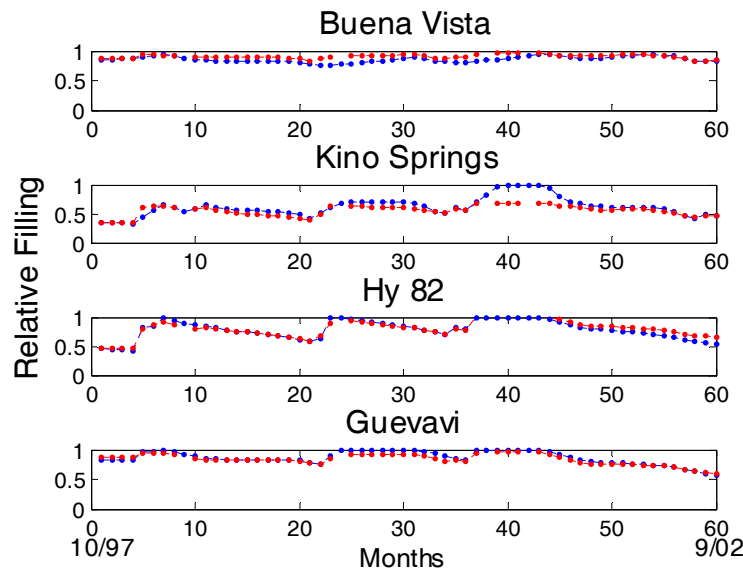


Figure F-7: Comparison of the relative capacity of the microbasins estimated by the AZDWR-MGM (red) and the SGMM models (blue), using dynamic infiltration and ET calculations as explained in the text.

F-4 Comparison with Index-wells

In Figure F-8 we compare the monthly simulation of DTW between the SGMM and index wells in the microbasins (see locations in Figure F-1). For the present development, the SGMM parameter values were selected to match the performance of the AZDWR-MGM model. Note that the DTW calculated by the SGMM represents an effective groundwater level of the entire surface area of the basin. Therefore, the comparison that is presented here is between areal and point values. In addition, the presentation of the data as continuous lines, although convenient for visual purpose, is misleading. This is because at this time scale (monthly) the data is discrete and the connection between two points may be other than linear. In Figure F-8 it can be seen that in most cases the model and the wells follow a similar trend. In all cases but for Buena Vista there is a well that matches model simulations very well. For Buena Vista there is a consistent deference between the DTW of the single available well and the model simulation. Due to the

relatively small capacity of that basin the point to areal estimate differences are accentuated.

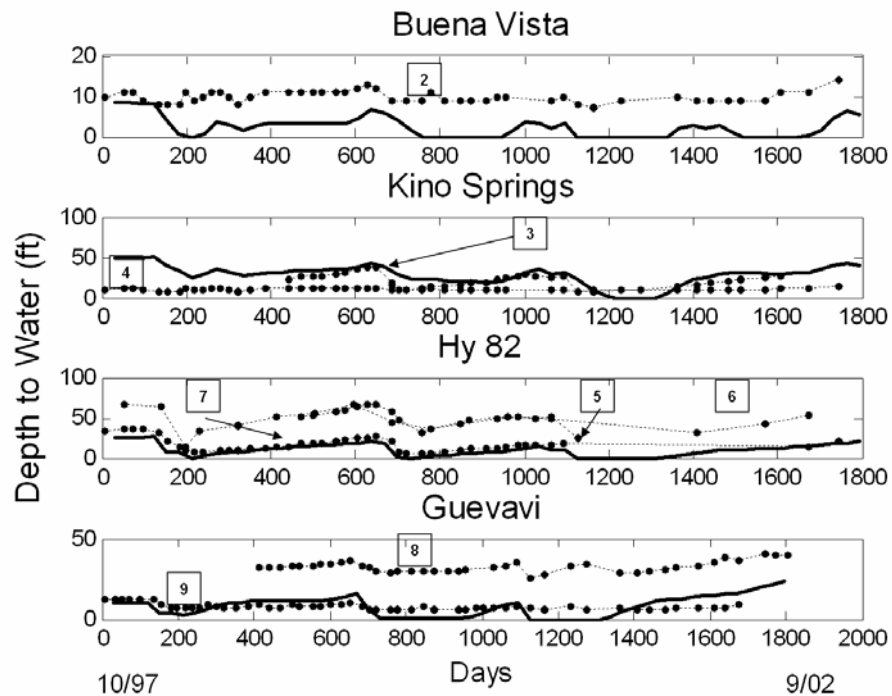


Figure F-8: Comparison between the SGMM monthly simulations of DTW and index wells in the microbasins. The numbers are associated with the well's location as indicated in Figure F-1. Data from Well-1 are not used because of insufficient record.

Chapter G

Use of Modeling for Risk Analysis - Examples

G.1 Introduction

In the previous sections we present the development of models that describe the hydrologic natural system. These models pertain to stochastic precipitation generation, transformation of precipitation into river flow, and changes in groundwater storage in the microbasins along the Santa Cruz River, downstream of the USGS gauge at Nogales, Arizona. In this section we present a case study that utilizes the aforementioned modeling system and demonstrates the utility of modeling for watershed management and planning. The results are for illustration purposes only as the parameters and the assumptions used in these case studies should be fine tuned to reflect the concerns and the objectives of the region prior to the use of the results in decision making.

G.2 Examples of Risk Analysis

In the first case study, the SGMM (Simplified Groundwater Model for the Microbasins, see Chapter F) was forced by a monthly ensemble of 100 realizations, each 100-years long, to produce an ensemble of groundwater storages and levels in the four microbasins. Different annual pumping rates from the conceptual reservoirs (simulating the microbasins) were assigned as a percentage of the reservoir capacity. The ranges of the pumpage withdrawals are from no pumping to 50% of the reservoir capacity. The annual pumpage withdrawals were distributed equally among the months.

For each ensemble, the conceptual reservoir initial storage condition was assigned randomly from the whole range of possible reservoir storages using a uniform distribution. The first year was discarded for the analysis to follow. In Figure G-1 the fraction of time in which the reservoir storage is below a set threshold is presented as a function of the pumpage rate. The thresholds in this case were defined as 25 50 and 75% (upper, middle and lower panels, respectively) of the reservoir capacity. Many of the reservoir response characteristics can be discerned from this figure. It can be seen for example, that the Buena Vista and Guevavi are more sensitive reservoirs and for large pumpage values the storage of these reservoirs is below the thresholds most of the time. However these reservoirs are different one from the other in their response and sensitivity to increasing pumpage. The Buena Vista reservoir has a small pumpage range tolerance for different thresholds, in that the reservoir storage moves sharply from being above the threshold to being below it most of the time. The Guevavi reservoir shows a more gradual change in going below the storage threshold with increasing pumpage. The Kino Springs and Highway 82 reservoirs also show a gradual increase in the frequency of going below the thresholds with increasing pumpage, although, much smaller than that of Guevavi. No apparent differences were observed between the results of Figure G-1 and those

created using the above described analysis for an ensemble that includes 1000 realizations.

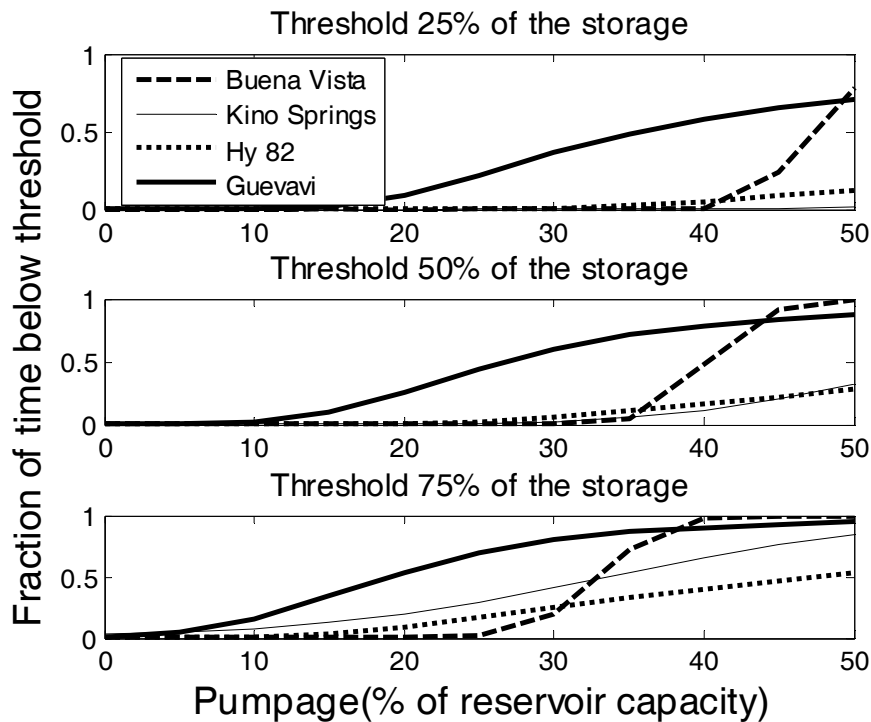


Figure G-1: The fraction of the time during 100 years that the monthly water storage in the microbasins is below 25, 50 and 75% (upper, middle and lower panels, respectively) of capacity, as a function of the annual pumpage from the reservoirs. A total of 100 realizations of storage sequences are used.

In Figure G-2 we explore the uncertainty in groundwater content that is associated with the variability of the streamflow prediction. In this Figure, the median, 5, and 95 percentiles of the 100 realizations are shown, but this time only for the 50% reservoir storage threshold. The uncertainty in this Figure is fairly constant and can be estimated at about $\pm 10\%$. It implies that by representing the variability in the observed precipitation and streamflow as discerned from the gauge record, the uncertainty in predicting the fraction of the time that the reservoirs will be below 50% of their storage capacity is within 10%. This uncertainty bound is established for an 100-year simulation. Again no apparent differences were observed in the uncertainty bound for an ensemble that has 1000 realizations.

An additional management and planning concern is the duration of the potential reservoir stress. In other words, a persistent stress of the aquifer might be a larger concern than the occasional stresses.

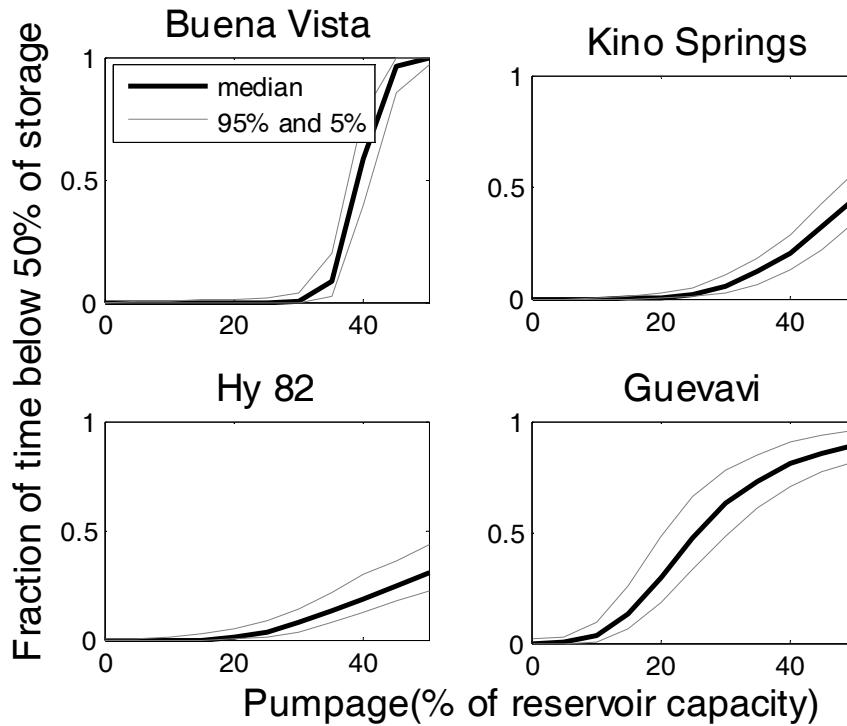


Figure G-2: The fraction of the time during 100 years that the monthly water storage in the microbasins is below 50% as a function of the annual pumpage from the reservoirs. The black solid line is the median and the gray lines are the 5 and 95 percentiles as determined from 100 realizations.

In Figure G-3, we analyze a single realization of 100 years for the number of occurrences in which the reservoirs have shown consecutive monthly stresses. These stresses are ranged from 1 to 20 consecutive months (x-axis). The stress in this example is defined as reservoir storage being below 50% of its capacity. These consecutive stress periods were exploited with different levels of pumpage rates. The Figure again presents the difference in the response of the four microbasins to different rates of withdrawals. The Buena Vista and Guevavi reservoirs have a critical pumpage value that, if exceeded, puts the reservoirs in persistent stress. The other two reservoirs are more sensitive to the climate variability and can recover more easily after a stress period.

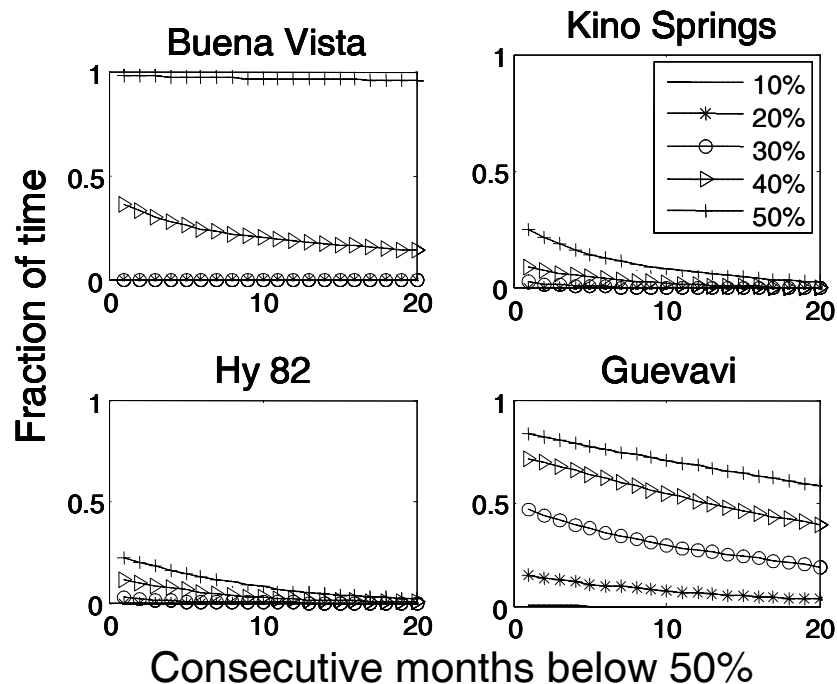


Figure G-3: The number of consecutive months with microbasin storage below 50% of capacity determined from a single realization of 100 years. The different lines represent different pumpage schemes.

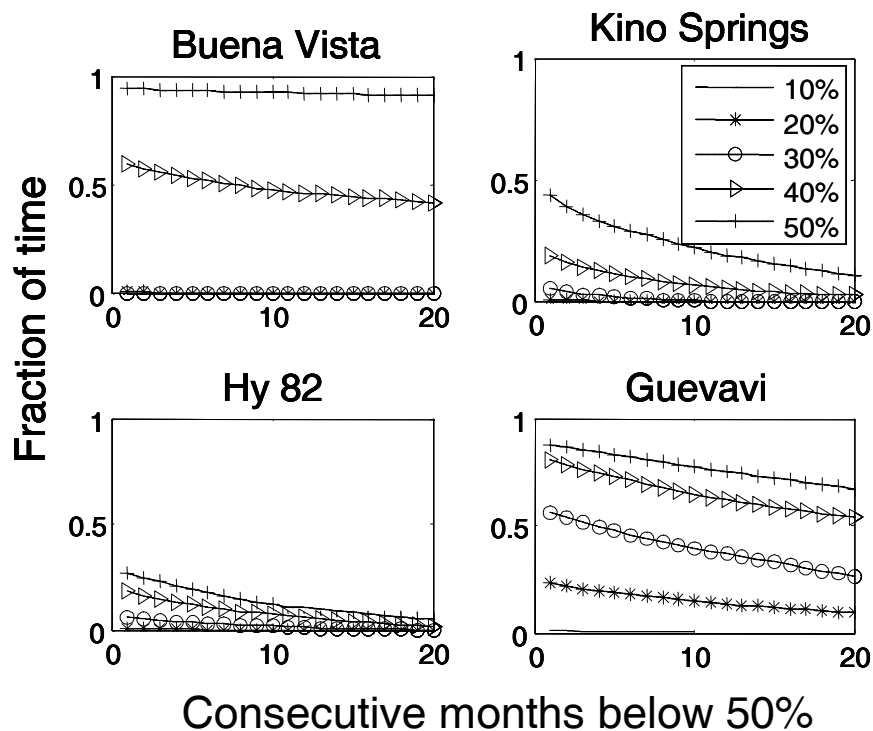


Figure G-4: As in Figure G-3, but created from an ensemble that has 1000 realizations, 100-years long each.

In Figure G-4 the same analysis is repeated for an ensemble of 1000 realizations. We note that the occurrence of the consecutive stresses in all microbasins appear more frequent in the 1000 members ensemble.

In Figure G-5 the ensemble is analyzed to provide uncertainty bounds for the consecutive occurrence of stressed microbasins (storage less than 50% of the capacity) for a pumpage scheme of 40% of the capacity. This estimate of uncertainty is a result of precipitation variability. It can be seen that the microbasins show a range of different uncertainty bounds. In general it can be said that the higher the probability to have consecutive stresses the wider the uncertainty bound.

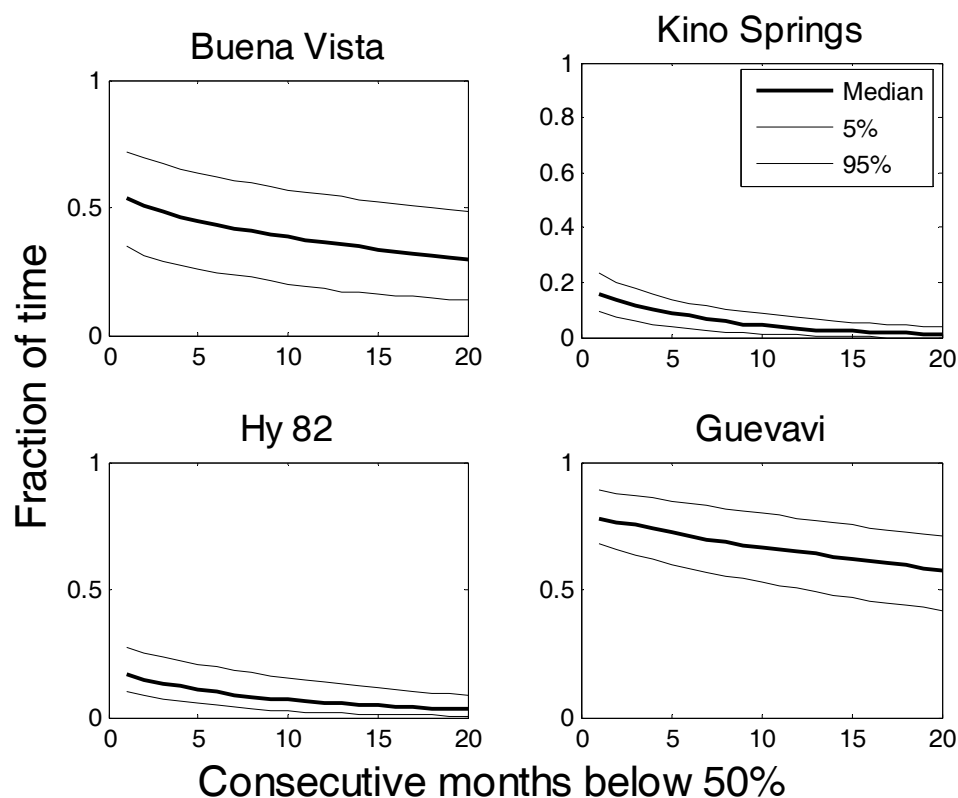


Figure G-5: Median, 5 and 95 percentiles of the number of consecutive months with microbasin storage that is below 50% of capacity as determined from a 100 realizations of 100 years each, and for annual pumpage that is 40% of the microbasin capacity.

The above analysis was also conducted with the ensemble of streamflow that is based on the paleo-climatic precipitation estimates from tree-ring records. This ensemble has a record duration of 317 years. The production of this ensemble is described in Chapter D of this report. The results of the stress frequency of occurrence when the entire paleo-climatic record was analyzed appear very similar to those of the analysis presented above. In a second experiment with results shown in Figure G-6, the entire ensemble record of

317 years was divided into 14 different ensembles, each ensemble of a 100-year duration. The collection of the ensembles has starts that span the entire paleo-climatic record with 200-month intervals. The spread among the realizations in the Figure represents the uncertainty that is associated with both intra- and the inter-annual variability in different 100-year sections, as discerned from the paleo-climatic precipitation estimates. Comparing Figures G-6 and G-2 makes the difference in uncertainty in the groundwater content results apparent for the two cases: (a) when only the historical record is used, and (b) when the paleo-climatic record is used. The breadth of the 5-95 percentile band around the median is significantly higher when paleo-climatic information is used for all cases. Suggesting that the historical record cannot in itself lead to reliable risk definitions due to significant additional long-term variability

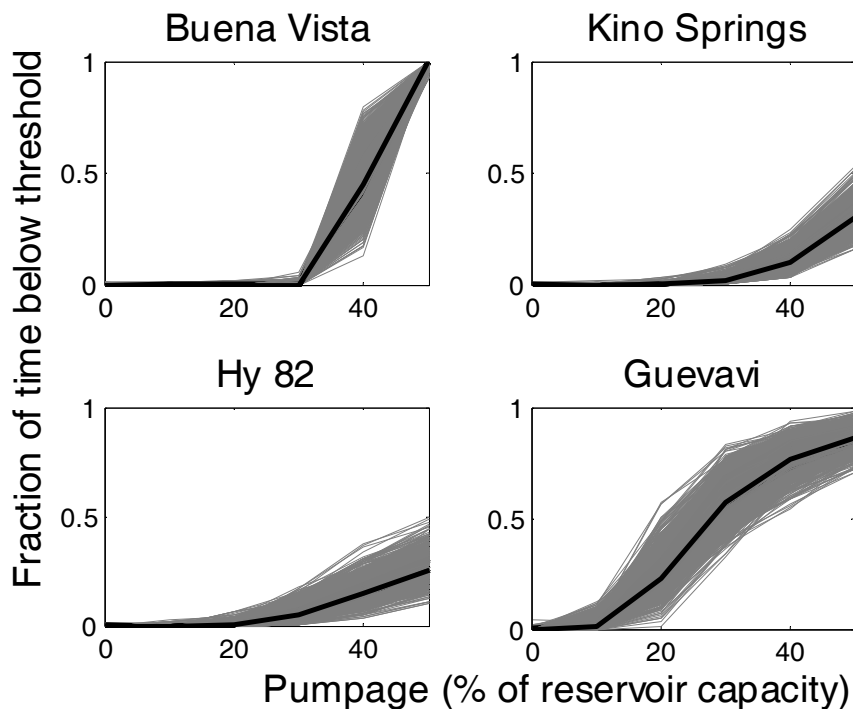


Figure G-6: The fraction of the time during 100 years that the monthly water storages in the reservoirs are below 50% of capacity as a function of the annual pumpage from the reservoirs. The gray lines represent the ensemble members derived from 14 ensembles that represent the long-term variability that corresponds to the paleo-climatic record. Each of the 14 ensembles is 100 years long. These ensembles start in 200-month intervals and span the paleo-climatic record of 317 years.

Chapter H

Conclusions and Recommendations

This chapter summarizes the major findings and conclusions of this study. It also puts forth recommendations for using the results and tools developed and for extending the analysis in directions perceived to be useful.

H.1 Findings and Conclusions

Chapter A includes data analysis of the historical precipitation and streamflow records. The main findings and conclusions follow:

1. Observed daily record at the Nogales gauge shows large variability, extended periods of no flow, high positive skewness, and moderate lag-1 autocorrelation. Mean daily flows exhibits pronounced seasonality with most flow events occurring in August while least occurs in May and June. Due to tropical storm contributions, October stands out as a month few events but of highest flow. Winter and summer are the wetter seasons in the region.
2. The daily flow record shows a decline trend of the number and monthly volume of flow peaks above a given threshold for summer and for the period of record (1935 – 2003). This is corroborated by a similar trend found for the Lochiel gauge in the headwaters of the Santa Cruz River and with trends found down stream and reported in other studies. Analogous winter analysis did not reveal such a trend for that season. The precipitation record at the nearby gauge site also indicated a similar decline trend in the number of daily precipitation events but it showed no trend in the magnitude of the seasonal precipitation amount. Changes in the precipitation recording parameters in the mid 70s may have contributed to these precipitation results.
3. Wavelet analysis of the mean daily flow at the Nogales gauge showed a pronounced decadal of variability from the 50s to the 90s, with a variety of scales of variability (from monthly to biennial) during several segments of the record. Indication for self similarity of the time series signal was also found from the scale versus time plot of the wavelet coefficient values.
4. Correlative analysis of seasonal precipitation at Nogales with Equatorial Pacific sea surface temperature signals pertaining to the El Niño Southern Oscillation (ENSO) phenomenon and with the Pacific Decadal Oscillation (PDO) index showed a relationship to ENSO of moderate strength for winter. The short period of record and the similar behavior of the ENSO and PDO indices for the period of record did not allow the development of definitive analyses results for the PDO. Seasonal precipitation at Nogales correlates very well with concurrent seasonal precipitation averaged over Arizona Climate Division 7 during winter; a result of the large spatial and temporal storm character during winter. Analogous correlations for summer are much more modest.

Chapter B contains the stochastic hourly precipitation model development. Main findings and conclusions follow:

1. Stochastic precipitation and flow generation models were calibrated on the basis of relevant statistics obtained from the available observed long-term records of the Nogales stream gauge (of daily flow) and a nearby precipitation gauge (of hourly precipitation). The precipitation gauge is the only one available in this region.
2. Intercomparison of Nogales precipitation gauge records with corresponding atmospheric mesoscale model simulated basin average precipitation records for a relatively wet, a medium and a relatively dry winter month, showed that the point records adequately represent the frequency of occurrence of significant precipitation amounts and the precipitation regime in the contributing area of the Nogales stream gauge.
3. The point process character of hourly observed precipitation is manifested by exponential distributions of precipitation clusters with mean durations of 2 and 6 days in summer and winter, respectively. Both seasonal and category (wet, medium dry) dependence of the sample frequency distributions of the duration of precipitation clusters and of the hourly precipitation amounts was found, with longer cluster lengths supporting a higher number of hourly precipitation events.
4. The performance of the point process model in reproducing observed seasonal precipitation volumes, total number of precipitation events per season, and number of greater than trace hourly precipitation amounts was satisfactory for all categories (wet, medium and dry), especially for summer.
5. A conceptual infiltration excess rain-to-flow model with dependence on antecedent soil water conditions was found adequate to reproduce the exceedance frequency statistics of the observed flow record on daily, seasonal and annual scales at the Nogales stream gauge, when forced with the generated precipitation record.

Chapter C describes the development of a stochastic ARMA(1,1) model for monthly flow. Main findings and conclusions follow:

1. An ARMA (1,1) model of the transformed and standardized monthly flows generates likely monthly flow scenarios that resemble the observed ones on that temporal scale, with the simulated flows overestimating the extreme high flows somewhat. The parameters of the ARMA(1,1) model are temporal-scale specific and they cannot be used to produce flows on different temporal scales (e.g., daily flows).

Chapter D (see also Annex A) describes the use of the paleo-climatic seasonal and annual precipitation reconstructions for flow generation by the hydrologic models developed in previous chapters. Main findings and conclusions follow:

1. Seasonal and annual precipitation was reconstructed from all available tree-ring data in the region. Winter is the only season with more than 50% of seasonal precipitation variability explained by tree-ring data. The winter reconstruction covers the period from 1647 through 1966 and tracks the observed precipitation closely during the 1915 – 1966 calibration period. The paleo-climatic record development is described in Annex A.
2. The paleo-climatic reconstruction of winter precipitation records was used with the precipitation-based flow generation model of Chapter B. The resultant generated flows indicate several periods of drought that span several decades over a time period of more than 300 years of record. This finding suggests caution when using the historical observed record (duration of continuous record is less than 70 years) to characterize and simulate the behavior of daily flows.

Chapter E describes a method for estimating the value of the generated ensemble of streamflow in economic terms (cost/loss ratio analysis). Main findings and conclusions follow:

1. A measure of the value of the generated ensembles for decision making was estimated using cost-loss ratio analysis. The analysis considered annual flows and minimum flow targets, and was cast in the context of decisions to allow (or not) groundwater exploitation in the region. Decisions are associated with hypothetical annualized costs and losses. It was found that the potential relative economic value of the generated ensemble increases as the cost to loss ratio increases and as the minimum flow target increases.

Chapter F describes the development of a simplified groundwater model for four micro-basin aquifers located downstream of the Nogales stream gauge. Main findings and conclusions follow:

1. A simplified groundwater response model was developed to mimic the detailed spatially distributed model that the Arizona Department of Water Resources runs for the microbasins fed by the Santa Cruz River near the Mexico border and downstream of the Nogales stream gauge. The model is based on a series of conceptual reservoirs with parameterized recharge and evapotranspiration functions. The parameters are defined to match the simulations of the detailed model over a five year period. Comparison of the simplified model simulations with those of the detailed model simulations yielded excellent results, except in some cases of high flows when the distributed nature of the processes could not be reproduced well by the simplified model. Comparison with observed depth-to-groundwater level data obtained from wells in the region also indicated good performance. This simplified model was used to illustrate the utility of the generated flow ensembles for groundwater risk analysis in the region.

Chapter G illustrates a methodology for risk assessment that utilizes the modeling system developed in this work. Main findings and conclusions follow:

1. The system of flow generation and groundwater content models developed in this work was used to illustrate risk analysis for the regional groundwater resources for the four microbasins downstream of the Nogales stream gauge. The risk analysis evaluates the frequency associated with groundwater content decline in the reservoir (microbasins) below an assigned volume threshold value, under various hypothesized withdrawal rates (pumping). In addition the probability of consecutive periods of groundwater stress was evaluated. The results indicate different microbasin sensitivities of the frequency of occurrence of groundwater contents below given thresholds to individual microbasin characteristics and envisioned pumpage scenarios. More importantly, the results also show that the generation of likely future flows on the basis of the historical (67 years) record alone will underestimate the actual risk of groundwater basin stress, as estimated from the use of the historical record and paleo-climatic information from dendrochronology.

H.2 Recommendations

The analysis and findings of the work reported herein lead to the following recommendations:

1. The modeling system developed in Chapters A and B, including the simplified groundwater response model for the four microbasins of Chapter F, should be used with the risk analysis methodology of Chapter G in a screening analysis for determining possible strategies for regional development in the microbasin area associated with acceptable risk levels. In addition, and for judiciously selected streamflow ensemble members, runs of the AZDWR detailed groundwater model should also be made to establish base scenarios of likely groundwater evolution. These then may be augmented with uncertainty estimated from the screening runs to establish refined risk levels. Interaction with regional officials and agencies to determine appropriate levels of risk to consider in the screening analysis, type of groundwater stress (volume and/or level; single violation of standards or repeated consecutive violations of standards), and locations of particular interest would be necessary.
2. Once some experience with the use of the models and methodologies has been acquired for the Santa Cruz River region of this work, application in other semiarid areas of varying data availability should produce useful results. The establishment of larger-area groundwater risk maps may also then be possible.
3. The present analysis uses paleoclimatic reconstructions to probe long-range variability that cannot be inferred from the short-duration historical record of streamflow. However, published research studies indicate that recent climatic changes may be attributed to anthropogenic causes and these changes may introduce variability in the hydrologic records that has not been observed so far. For this reason, it is recommended that the present analysis is extended to utilize the models developed with climate change scenarios produced by state-of-the-

science global climate models (GCMs) and downscaling procedures to develop additional groundwater risk analysis.

Chapter I

References

- Box G.E.P, and O. R. Cox. 1964: The analysis of transformation. *Journal of the Royal Statistical Society B*.26(2): 211-252.
- Bradley, R. S., M. Vuille, D. Hardy, and L. G. Thompson, 2003: Low latitude ice cores record Pacific sea surface temperatures, *Geophysical Research Letters*, 30(4), 1174,
- Cayan, D. R., M. D. Dettinger, H. F. Diaz, and N. E. Graham, 1998: Decadal variability of precipitation over western North America, *Journal of Climate*, 11, 3148-3166.
- Cook, E. R., 2000: Southwestern USA Drought Index Reconstruction, International Tree-Ring Data Bank. IGBP PAGES/World Data Center-A for Paleoclimatology, Data Contribution Series #2000-053, NOAA/NGDC Paleoclimatology Program, Boulder, CO, USA, <http://www.ngdc.noaa.gov>.
- Dudhia, J., A nonhydrostatic version of the Penn State/NCAR mesoscale model: Validation tests and simulation of an Atlantic cyclone and clod front, *Mon. Wea. Rev.* 121, 1493-1513, 1993.
- Graham, N. E., 2004: Late Holocene teleconnections between tropical Pacific climate variability and precipitation in the western USA: evidence from proxy records, *Holocene*, 14, 436-447.
- Erwin, G., 2003: Microbasins test recharge run, Draft Memorandum to Alejandro Barcenas, Arizona Department of Water Resources, Phoenix, AZ.
- Hirsch, R. M., D. R. Helsel, T. A. Cohn, and E. J. Gilroy. 1993: Hydrologic Statistics. Chapter 17. in *Handbook of Hydrology* editor D. R. Maidment McGraw Hill.
- Kaplan, A., M. A. Cane, Y. Kushnir, B. Blumenthal, and B. Rajagopalan, 1997: Analysis of global sea surface temperature 1856-1991, *Journal of Geophysical. Research*, **101**, 22599-22617.
- Kepner, B., 1999: San Pedro River – A landscape approach to community based environmental protection: U.S EPA fact sheet.
- Mantua, J. N., S. R. Hare, Y. Zhang, J. M. Wallace, and R. C. Francis, 1997: A Pacific interdecadal oscillation with impacts on salmon production, *Bulletin of American Meteorology Society*, 78, 1069-1080.
- Misrili, F., H.V. Gupta, S. Sorooshian. 2002: Bayesian recursive estimation of parameter and output uncertainty for watershed models, *In AGU Monograph: Advances in Model Calibration*, Duan QH. Gupta HV, Sorooshian S, Rousseau AN, Turcotte R. (eds.).
- Pool, D. R and Coes A. L. 1999: Hydrogeologic investigation of the Sierra Vista subwatershed of the upper San Pedro basin, Cochise county, Southeast Arizona. *USGS Water-Resources Investigation Report 99-4197*. United States Geological Survey, Tucson Arizona.
- Räisänen, J., and T.N. Palmer, 2001: A probability and decision-model analysis of a multi-model ensemble of climate change simulations. *Journal of Climate* 14, 3212-3226.

- Redmond, K. T. and R. W. Koch, 1991: Surface climate and streamflow variability in the western United States and their relation to large-scale circulation indices, *Water Resources Research*, 27, 2381-2399.
- Restrepo-Posada, P. J., and P. S. Eagleson, 1982: Identification of independent rainstorms. *Journal of Hydrology* 55, 303-319.
- Saco, P. and Kumar, P., 2000: Coherent modes in multiscale variability of streamflow over the United States. *Water Resources Research* 36(4), 1049-1067.
- Salas J. D Analysis and modeling of hydrologic time series Chapter 19. in *Handbook of Hydrology* editor D. R. Maidment McGraw Hill 1993.
- Thompson, L. G., E. Mosley-Thompson, and M. Arno, B., 1984: Major El Niño / Southern Oscillation events recorded in stratigraphy of the tropical Quelccaya Ice Cap, *Science*, 226, 50-52.
- Wang J. and K. P. Georgakakos, Validation and sensitivities of dynamic precipitation simulation for winter events over the Folsom Lake Watershed: 1964–99. *Mon. Wea. Rev.*, 133(1), 3–19, 2005.
- Webb, R., and J. L. Betancourt, 1990: Climatic variability and flood frequency of the Santa Cruz River, Pima County, Arizona. *USGS Open –File Report 90-553*. United States Geological Survey, Reston, Virginia.
- Zhang. Y., J. M. Wallace, and D. S. Battisti, 1997: ENSO-like Interdecadal variability: 1900-93, *Journal of Climate*, 10, 1004-1020.
- Zhu, Y., Toth, Z., Wobus, R., Richardson, D., and K. Mylne, 2002: The economic value of ensemble-based weather forecasts. *Bulletin of the American Meteorological Society*, 73-83.

Annex A

Tree-ring reconstruction of annual and seasonal precipitation at Nogales, Arizona

By

David M. Meko
618 N. Richey Blvd
Tucson, AZ
85716

Work conducted under contract for:
The Hydrologic Research Center
12780 High Bluff Drive, Suite 250
San Diego, CA 92130, USA

Table of Contents

INTRODUCTION.....	AA-3
TREE-RING SCREENING.....	AA-3
SEASONAL PRECIPITATION RECONSTRUCTIONS.....	AA-8
LOW FREQUENCY VARIATIONS IN RECONSTRUCTED PRECIPITATION	AA-10
CONSISTENCY WITH OTHER RECONSTRUCTIONS.....	AA-16
CONCLUSIONS.....	AA-18
REFERENCES.....	AA-19
APPENDIX A.....	AA-20
APPENDIX B.....	AA-25
APPENDIX C	AA-30
APPENDIX D	AA-35

INTRODUCTION

This report summarizes work on a contract titled “Tree-ring data analysis to estimate the baseline low-frequency variation in annual and seasonal precipitation in the headwaters region of the Santa Cruz River within the U.S.”. Early in the project, in accordance with hydrologic objectives of HRC, the target reconstruction area was shifted from the headwaters region to Nogales, Arizona. This report is organized by task as listed in the original work plan. The main objectives were: 1) reconstruction of seasonal-total precipitation for Nogales, Arizona, from tree-ring data, 2) analysis of the reconstructions for information on low-frequency variations in precipitation, and 3) evaluation of consistency of results with other existing dendrohydrologic reconstructions for the region. Tables with detailed summaries of reconstruction modeling are deferred to Appendixes A, B, and C. Appendix D contains a list of weights for Gaussian filters used in smoothing time series. The accompanying Excel spreadsheet, “Tree_Ring_Study.xls” contains data specified as deliverable under the contract. This includes the original tree-ring chronologies, the seasonal precipitation reconstructions for Nogales, and the other dendroclimatic reconstructions which the Nogales reconstructions are compared with in this report.

TREE-RING SCREENING

“Task 1. Assemble computer files of tree-ring chronologies in the southeastern corner of Arizona, and statistically screen the index chronologies for significant correlation with precipitation in the U.S. portion of the headwaters region of the Santa Cruz River.”

Original 48-site network before climate screening. A total of 48 tree-ring chronologies were assembled for the study from a search of the files of the Laboratory of Tree-Ring Research (LTRR) at the University of Arizona and the online files of NOAA’s International Tree-Ring Data Bank (ITRDB). The network contains all available total-width, earlywood-width and latewood width chronologies with complete time coverage of at least the period A.D. 1780-1965 located between latitudes 29°N and 33°N and longitudes 109°W and 112 °W (Figure 1). Species, location, time coverage and other information for the tree-ring chronologies of total width (38), earlywood width (5) and latewood width (5) are listed in Table 1. The earlywood and latewood chronologies were re-standardized for this project from the original ring widths to ensure uniformity of data processing --- in particular removal of age-related or size-related trend from the ring widths in converting them to dimensionless indices of tree growth. Following recommended guidelines, these ring-width series were all detrended with a cubic smoothing spline whose frequency response is 0.50 at a wavelength 70% the length of the ring-width series (Cook et al. 1990). The full set of 48 tree-ring chronologies for the period A.D. 1270 to the end of record are listed in Tree_Ring_Study.xls.

Precipitation data. The precipitation data for the analysis was specified to be a previously prepared “merged Nogales” record of seasonal total precipitation for four seasons: October,

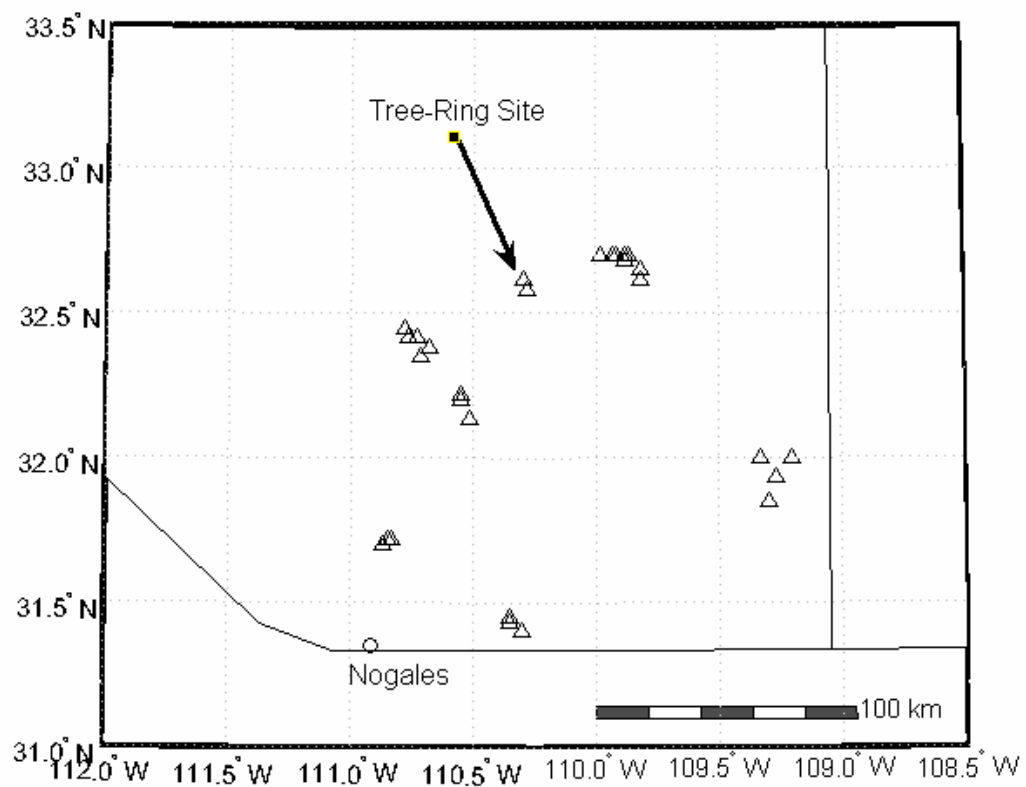


Figure mapsites_1. Tree-ring network for Nogales precipitation reconstruction. Network includes 48 chronologies. Number of distinct symbols fewer than 48 because some approximate locations represented by multiple chronologies (e.g., of different species).

Table 1. Listing of tree-ring chronologies. Screening criteria were: starting year 1800 or earlier, (29°N <= latitude <33°N), and (109°W <= longitude < 112°W).

N ¹	File ²	Site Name	Species Code ³	v ⁴	Location ⁵			Period ⁶	
					lat	long	el(m)	Start	End
1	psc.crn	PAT SCOTT PEAK	PSME	wt	31.43	-110.35	2440	1571	1993
2	az556.crn	SCHEELITE CANYON, HUACHUCA MT	PSME	wt	31.45	-110.35	1750	1630	1995
3	az504.crn	SANTA RITA MTNS, HIGH (FLORIDA)	PSME	wt	31.72	-110.85	2438	1645	1966
4	az544.crn	SANTA RITA	PSME	wt	31.72	-110.83	2407	1600	1986
5	az526.crn	MOUNT HOPKIN'S	PIPO	wt	31.70	-110.87	2133	1720	1987
6	az519.crn	GREEN MOUNTIAN	PSME	wt	32.38	-110.68	2194	1550	1986
7	az531.crn	NORTH SLOPE	PSME	wt	32.22	-110.55	2441	1640	1987
8	az033.crn	GALIURO MTNS, SITE A	PSME	wt	32.58	-110.28	2134	1650	1965
9	az529.crn	NORTH SLOPE	ABCO	wt	32.22	-110.55	2441	1780	1987
10	az525.crn	HELEN'S DOME	PISF	wt	32.22	-110.55	2535	1720	1987
11	az557.crn	REEF OF ROCKS	PSME	wt	32.45	-110.78	2550	1321	1998
12	az520.crn	GREEN MOUNTAIN	PIPO	wt	32.38	-110.68	2194	1460	1986
13	az532.crn	NORTH SLOPE	PIST	wt	32.22	-110.55	2441	1700	1987
14	az516.crn	DEVIL'S BATHTUB	PIED	wt	32.20	-110.55	2286	1720	1987
15	az515.crn	BEAR WALLOW	PSME	wt	32.42	-110.73	2484	1610	1987
16	az506.crn	CHERRY CANYON	PICM	wt	32.35	-110.72	1645	1766	1987
17	az501.crn	SANTA CATALINA MTNS (HIGH)	PSME	wt	32.42	-110.77	2774	1526	1968
18	az524.crn	HELEN'S DOME	PIPO	wt	32.22	-110.55	2535	1690	1987
19	az555.crn	MT LEMMON	PSME	wt	32.45	-110.78	2700	1568	1983
20	pdf.crn	PADDYS RIVER DOUGLAS-FIR	PSME	wt	32.58	-110.28	2119	1605	1994
21	padpos.crn	PADDYS RIVER PONDEROSA PINE	PIPO	wt	32.58	-110.28	2134	1596	1994
22	az530.crn	NORTH SLOPE	PIPO	wt	32.22	-110.55	2441	1720	1987
23	dcydfs.crn	DOUGLAS CANYON DOUGLAS-FIR	PSME	wt	32.62	-110.30	2027	1652	1992
24	az546.crn	TUCSON SIDE	PISF	wt	32.22	-110.55	2362	1670	1987
25	az545.crn	TUCSON SIDE	PIPO	wt	32.20	-110.55	2362	1660	1987
26	az534.crn	PINERY CANYON	PSME	wt	31.93	-109.27	2286	1650	1986
27	az551.crn	FLY PEAK CHIRICAHUA MTS	PSME	wt	31.85	-109.30	2790	1703	1983
28	az549.crn	PETER'S FLAT, PINALENO MOUNTAI	PSME	wt	32.70	-109.93	2950	1557	1991
29	az550.crn	FORT GRANT OVERLOOK, PINALENO	PISF	wt	32.70	-109.92	2896	1249	1991
30	az528.crn	NOON CREEK	PIPO	wt	32.65	-109.82	2346	1770	1987
31	az540.crn	RHYOLITE CANYON	PIPO	wt	32.00	-109.33	1828	1640	1987
32	az512.crn	EMERALD PEAK, PINALENO MOUNTAI	ABLA	wt	32.70	-109.88	3120	1752	1989
33	az511.crn	MOUNT GRAHAM, PINALENO MOUNTAI	PCEN	wt	32.70	-109.87	3221	1696	1990
34	az537.crn	RHYOLITE CANYON	PSME	wt	32.00	-109.33	1828	1640	1987
35	az536.crn	POST CREEK	PSME	wt	32.68	-109.88	2727	1610	1986
36	cmpnt.crn	CAMP POINT, PINALENO MTNS	PSME	wt	32.70	-109.92	2900	1106	1990
37	az056.crn	LADYBUG PEAK, PINALENO MTNS	PSME	wt	32.62	-109.82	2652	1625	1967
38	az040.crn	CLARK PEAK SADDLE, PINALENO MT	PSME	wt	32.70	-109.98	3682	1630	1967
39	dcyw1.crn	DOUGLAS CANYON DOUGLAS-FIR	PSME	we	32.62	-110.30	2027	1652	1993
40	pdfw1.crn	PADDYS RIVER DOUGLAS-FIR EW	PSME	we	32.58	-110.28	2119	1605	1994
41	rhyw1.crn	RHYOLITE CANYON EARLYWOOD	PSME	we	32.00	-109.20	1828	1528	1992
42	rinw1.crn	RINCON PEAK EARLYWOOD	PSME	we	32.13	-110.52	2774	1591	1997
43	slcw1.crn	SCHEELITE CANYON EARLYWOOD	PSME	we	31.40	-110.30	1750	1630	1995
44	dcyw11.crn	DOUGLAS CANYON DOUGLAS-FIR	PSME	wl	32.62	-110.30	2027	1652	1992
45	pdfw11.crn	PADDYS RIVER DOUGLAS-FIR LW	PSME	wl	32.58	-110.28	2119	1605	1994
46	rhyw11.crn	RHYOLITE CANYONE LATEWOOD	PSME	wl	32.00	-109.20	1828	1528	1992
47	rinw11.crn	RINCON PEAK LATEWOOD	PSME	wl	32.13	-110.52	2774	1591	1997
48	slcw11.crn	SCHEELITE CANYON LATEWOOD	PSME	wl	31.40	-110.30	1750	1630	1995

¹N=sequential number equal to column of chronology in time series storage matrix

²File= computer file of standard index chronology. Files from the International Tree-Ring Data Bank are identified by a state code followed by an number (e.g., AZ040.crn). All other chronologies were obtained from computer files at the Laboratory of Tree-Ring Research (LTRR).

³Species code: PSME = *Pseudotsuga menziesii*, ABCO = *Abies concolor*, PISF = *Pinus strobiformis*, PIPO = *Pinus ponderosa*, PIED = *Pinus edulis*, ABLA = *Abies lasiocarpa*, PCEN=Picea cen

⁴v=variable type (wt is total-width, we is earlywood width, wl is latewood width)

⁵location = approximate location of the tree-ring site

⁶Period = starting and ending year of the standard chronology

winter (Nov-Mar), dry season (April-June), and summer (July-September). Time series of seasonal precipitation for 1914-2000 or 1915-2000 (winter) were provided by HRC (Nick Graham, personal communication). The seasons are labeled to as oct, wtr, dry, and smr elsewhere in this report. The precipitation data for all seasons were not serially complete, as required for calibration in the tree-ring reconstruction models. Missing values for oct (1920, 1947) and dry (1947, 1999) were estimated by the mean-ratio method from monthly PRISM precipitation (Gibson et al. 2002) at coordinate 31.35°N, 110.917°W. For 85 years of overlap, seasonal precipitation for the Nogales merged record are highly correlated with the PRISM data: $r = 0.96$ for oct and $r = 0.90$ for dry. To estimate a missing seasonal total in the Nogales record, the corresponding seasonal total from the PRISM record was multiplied by 0.9164 (oct) or 1.0082 (dry).

After filling in the missing values in the Nogales seasonal precipitation, an additional season (water year, or wyr) was generated by summing the other four seasons. The resulting serially complete Nogales seasonal precipitation time series are listed in Tree_Ring_Study.xls. spreadsheet along with the monthly PRISM data used the mean-ratio estimation.

Screening Procedure. Tree-ring chronologies were screened against seasonal precipitation by linear regression. Because tree-ring indices have persistence that is at least partly biological in origin (Fritts 1976), a preliminary adjustment was made to remove linear dependence of the tree-ring index on its past values (prewhitening). A distributed-lag regression of precipitation on the prewhitened index was then used to quantify the strength of precipitation signal and to screen out tree-ring chronologies with no significant precipitation signal. The main steps are:

1. Prewhiten the standard tree-ring chronology with an autoregressive (AR) model to remove the statistical dependence of the annual index on its few preceding values
2. Regress seasonal precipitation against the prewhitened tree-ring index and its lagged values
3. Measure the signal strength of the chronology by the percentage of precipitation variance accounted for by regression (R^2 of regression)

The AR prewhitening models were estimated using the tree-ring indices for A.D 1270 and later (earlier part truncated, if necessary). AR models up to order 3 were fit, and the best model was selected by the Final Prediction Error (FPE) criterion (Ljung 1987). The AR residuals from the selected model are the prewhitened tree-ring indices. Seasonal precipitation was regressed against each prewhitened tree-ring index for the full available overlap of tree-rings and precipitation using a forward stepwise selection of variables. The predictand for a model was seasonal precipitation in year t ; the pool of potential predictors was the prewhitened tree-ring index in years $t - 3$ to $t + 1$.

The stepwise regression procedure had the following constraints:

1. A variable was allowed to enter if the p -value of its partial F -to-enter was less than 0.05 (Weisberg 1985).
2. A variable was removed if the p -value of its F -to-remove was greater than 0.10.

3. The model was rejected if the zero lag was not among the lags in the final model
4. The model was rejected as reflecting an unstable response if split-sample validation (Snee 1977) indicated lack of skill when the model calibrated on either the first or second half of the data was applied to predict the precipitation for the other half. The measure of skill used was the reduction of error statistic, RE, (Fritts et al. 1990), for which a positive value indicates “some” skill.
5. For those chronologies with a significant precipitation signal, the long-term tree-ring index was substituted into the regression model to generate individual reconstructions of the precipitation series from each chronology. These are referred to as “single-site reconstructions”.

Screening Results. The screening analysis indicated that the strongest tree-ring signal for precipitation is for the winter season, and that no statistically significant response exists for the single-month October season. The number of chronologies (of a maximum possible 48) with a significant ($\alpha = 0.05$ level) relationship with precipitation as measured by the overall F of regression varies from 0 for October to 41 for the water-year total (Table 2). Based on these results, reconstructions were generated for all seasons except October, and analysis of was focused on the winter reconstruction. Detailed summaries of the screening results for each season are include in Appendix A.

Table 2. Summary of signal strength for seasonal precipitation in individual tree-ring chronologies

Season	N ¹	Variance _{max} ²
October	0	--
Winter	37	53%
Dry	22	18%
Summer	4	11%
Water Year	41	29%

¹Number of chronologies (maximum possible 48) with statistically significant regression equation of seasonal precipitation on tree rings

²Maximum percentage of precipitation variance explained by any chronology

SEASONAL PRECIPITATION RECONSTRUCTIONS

“Task 2. Convert the network of screened chronologies into estimates of seasonal and total precipitation in the target headwaters region using regression models. Supply uncertainty estimates with the annual reconstructed values.”

The single-site reconstructions from the previous step were re-calibrated against the seasonal precipitation to arrive at the single final reconstruction of seasonal precipitation. The approach taken essentially amounts to a weighting of importance of the individual single-site reconstructions, and takes advantage of the likelihood that each chronology or group of chronologies might express a somewhat independent part of the precipitation variance. The approach, which is similar to that used in a reconstruction of San Pedro Basin precipitation (Meko 1997), also ensures the long-term reconstruction relies on tree-ring variations at many sites, and so is robust to unknown disturbances (e.g., insect infestations) that might have distorted tree-growth at individual sites.

Reconstruction Method. The method starts with the single-site reconstructions of seasonal precipitation generated from the previous step as input. These reconstructions have variable time coverage, depending on the length of the chronologies, and variable quality, as reflected in the R^2 of regression.

A review of the regression statistics for the individual chronologies (Appendix A) along with the time coverage of the chronologies (Table 1) suggested that the period of reliable precipitation reconstruction for this region is limited to about the last 300 years. Most of the chronologies with strong precipitation signal drop out before mid-1600s, and although there are chronologies extending to the A.D. 1300s or earlier (Table 1), those chronologies have a relatively weak signal for seasonal precipitation. The reconstruction models were therefore designed with the objective of precipitation reconstructions to the mid-1600s.

The main reconstructions steps for a particular season are:

1. Identify the chronologies with required time coverage and strong precipitation signal. Depending on the season of precipitation, additional restrictions were placed on tree-ring chronologies (single-site reconstructions) to be used as predictors for the final reconstructions. For seasons wtr and dry, only total-width and earlywood width were used; for wtr, only total-width chronologies were used; and for smr, only latewood width chronologies were used. Because there are only 5 latewood/earlywood chronologies, all of these were used in the model for the final reconstruction.
2. Run a principal components analysis (PCA) on the single-site reconstructions from step 1 above to derive a reduced number of orthogonal variables representing the main modes of tree-ring signal for seasonal precipitation. This PCA was run on the covariance matrix rather than the correlation matrix of the single-site reconstructions because the difference in variances of those reconstructions is important (we want to weight more heavily those chronologies that individually explain the most variance of seasonal precipitation). The PCA was run on the full common period of the selected set of single-site reconstructions. The new, orthogonal, tree-ring variables are the PC scores.

3. Regress the seasonal precipitation on the PC scores in a forward stepwise procedure, as before with the sequential F having a p -enter of 0.05 and p -remove of 0.10. Any PC individually accounting for more than 5 percent of the variance of the single-site reconstructions was included in the pool of potential predictors.
4. At each step of the stepwise procedure, the model was validated using “leave- n -out” cross-validation (Meko 1997); stepwise entry of predictors was terminated if the root-mean-square error (RMSE) of cross-validation increased with an additional predictor. This cross-validation check could in effect over-ride the p -enter criterion if the additional predictor failed to improve accuracy of prediction on independent data.

Reconstruction Results. Seasonal reconstructions were generated for all seasons except October, for which no chronologies had a significant precipitation signal. Statistics on the regression models are listed in Table 3. The starting year of reconstruction varies by season from A.D. 1647 to A.D. 1654, and precipitation variance explained ranges from 11% for summer to 57% to winter. The final seasonal reconstructions are based on only one or two PCs of the single-site reconstructions. The breakdown of predictors from chronologies to PCs is given under the “Predictors” heading in Table 3. For example, the winter reconstruction is based on regression of winter precipitation on the scores of two tree-ring PCs – PCs 1 and 3. Those predictors were in turn selected from a predictor pool of three PCs, and the PCs themselves are linear combinations of tree-ring variations for 24 tree-ring chronologies.

Table 3. Statistics of final seasonal precipitation reconstruction models.

Season	Year ¹	Accuracy ²		Predictors ³		Validation ⁴	
		R^2	R^2_{adj}	#vars	PCs	RMSE	RE(n_1/n_2)
Winter	1647	.57	.57	24/3/2	1,3	1.6947	0.50(52/7)
Dry	1650	.20	.19	14/4/2	1,2	0.7082	0.13(70/5)
Summer	1654	.11	.11	5/3/1	2	2.7547	0.05(79/7)
Water Year	1647	.33	.33	20/2/1	1	3.3826	0.28(52/9)

1Starting year of reconstructed precipitation

2Accuracy: Multiple coefficient of determination (R^2) and adjusted R^2 of the regression model; calibration period for models were 1915–66 (wtr), 1914–83 (dry), 1914–92 (smr) and 1915–66 (wyr)

3Predictors: #vars is the number of single-site reconstructions (chronologies) on which the PCA was done, the number of PCs included in the pool of potential predictors, and the number of PCs selected as predictors for the final model; PCs indicates which PCs were selected as the final predictors (1=PC#1, 2=PC#2, 3=PC#3).

4Validation root-mean-square error (RMSE) and reduction of error statistic. In parentheses after the RE statistic are the number of observations for the cross-validation residuals, and the number of observations, m , left out in leave- m -out cross-validation

The column labeled “RMSE” in Table 3 gives a conservative estimate of the reconstruction uncertainty. Assuming normally distributed residuals, the true precipitation should fall within $\pm 2\text{RMSE}$ of the reconstructed value 95% of the time. For example, the 95% confidence interval for wtr is $\hat{y} \pm 3.3894$ inches, where \hat{y} is the reconstructed precipitation for a given year.

It is evident from the statistics in Table 3 that winter is the only season with a strong tree-ring reconstruction. Time series plots of the observed and reconstructed precipitation series for the calibration periods likewise indicate that only the winter reconstruction strongly tracks the observed data (Figure 2). The tree-rings capture only 11% of the variance of precipitation in the wettest season -- summer. A considerably higher proportion of variance is explained for the water year, $R^2 = 0.33$, reflecting a combination of the weak signal for summer and strong signal for winter. Twenty percent of the precipitation variance is explained for the dry season, but that season contributes little to the annual total precipitation.

Detailed summaries of the stepwise models are deferred to Appendixes B and C.

LOW FREQUENCY VARIATIONS IN RECONSTRUCTED PRECIPITATION

“Task 3. Summarize the low-frequency variability of the individual seasonal reconstructions and differences in low-frequency components for warm season and cool season.”

Low-Frequency Variations in Seasonal Reconstructions. The time series of reconstructed winter and summer precipitation were examined with cross-spectral analysis for the common period 1654-1966. The method for the analysis was the smoothed periodogram, following Bloomfield (2000). The oct, dry and wyr reconstructions were not subjected to this analysis because of they are either highly correlated with the wtr reconstruction or are relatively poorly reconstructed by the tree-ring data. The smr component is also poorly reconstructed (11% variance explained) but is analyzed because the smr reconstruction was done exclusively with latewood-width chronologies, which were not used in any of the other seasonal reconstructions. We therefore might expect some freedom for independent movement in the seasonal reconstructions for wtr and smr.

The spectrum of reconstructed wtr is somewhat low-frequency in appearance, with less variance than expected at frequencies greater than about $f=0.35 \text{ yr}^{-1}$ (Figure 3, top left). The spectrum of reconstructed smr is flatter, and not significantly different from a white-noise spectrum except for decreased variance at the very low frequencies. This loss of very-low-frequency variance is probably an artifact of the detrending process applied to the latewood width time series used for smr reconstruction. The usable part of the latewood-width time series is usually restricted to the inner ~150 rings, and detrending that with conventional smoothing-spline techniques would greatly damp the variance at wavelength longer than 100 yr.

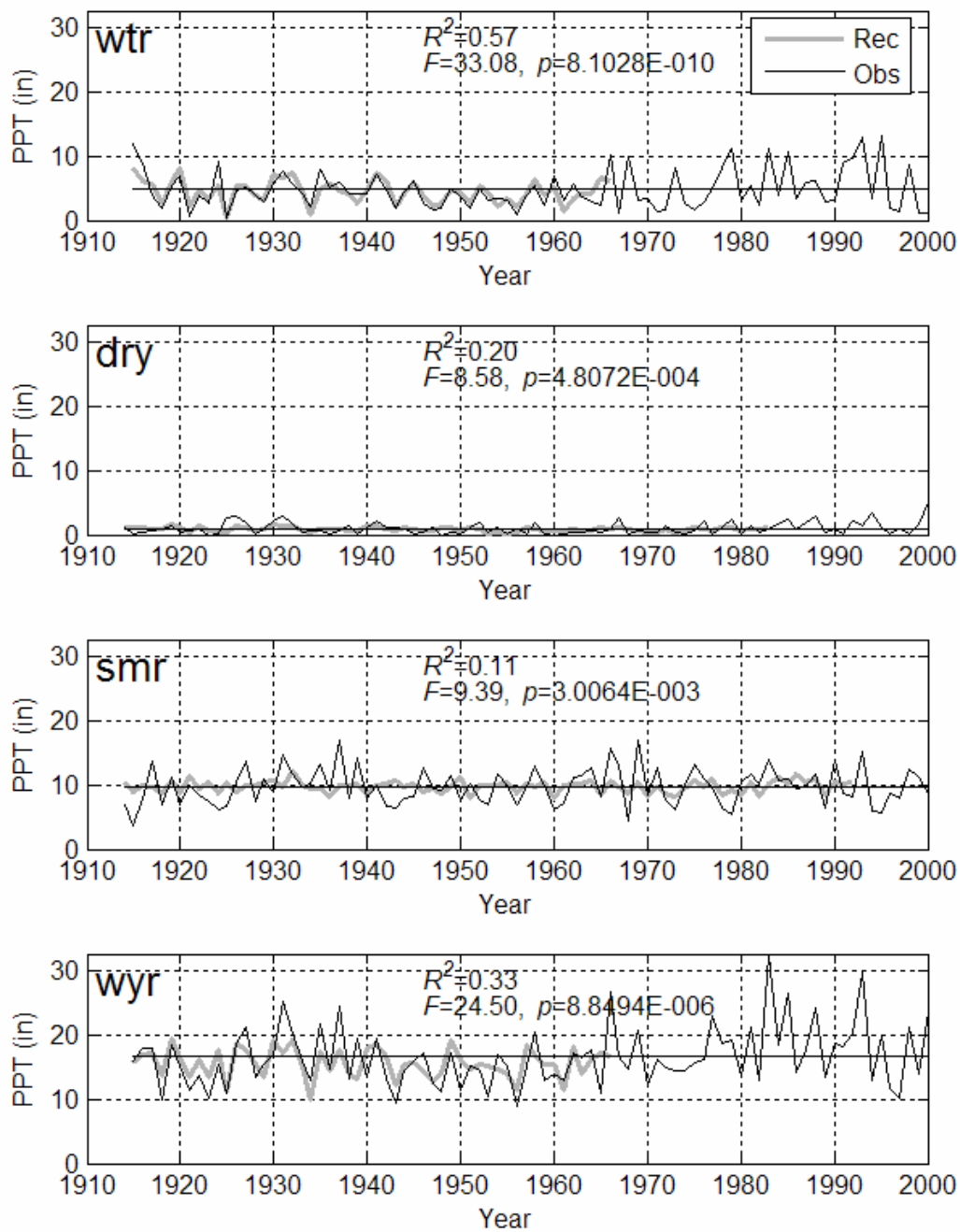


Figure recobs1. Time series of reconstructed and observed seasonal precipitation for the period covered by observed precipitation.

The cross-spectrum for reconstructed wtr and smr shows significant coherency at between wavelengths 10 and 50 yr (Figure 3, top right), and the phase diagram indicates that the highest coherency is associated with in-phase variations in the two time series. This coherency might indicate similar multidecadal climatic influence on precipitation in the two seasons, but might also be the result of the wtr and smr reconstructions not being derived from independent tree-ring variables. The smr reconstruction was generated from latewood-width chronologies and the wtr reconstruction from total-width and earlywood-width chronologies, but in the total-width component includes both the earlywood and latewood. Unfortunately, at this time the network of partial-width chronologies is not dense enough to use just earlywood width in deriving the wtr reconstruction.

The two reconstructed time series (wtr and smr) smoothed to emphasize multidecadal variation with a 9-yr Gaussian filter corroborate a generally synchrony in the low frequencies, though there certainly are exceptions (e.g., just before 1750) (Figure 4).

The smoothed time series has a much greater range for wtr than for smr, but that is largely a consequence of the regression process. Because the wtr reconstruction has a much higher explained variance than the summer reconstruction, we expect a greater range for wtr (e.g., zero explained variance would result in a horizontal line, no variability, for the reconstruction).

The most accurate of the seasonal reconstructions, wtr, is plotted in Figure 5. The top plot shows the unsmoothed time series, and the bottom the time series smoothed by various Gaussian filter emphasizing the low frequencies. Filter weights used for the plots are listed in Appendix D. The least-smoothed of the series (10-year Gaussian) retains considerable variability, with lows near 1670, 1820, 1890 and 1955, and largest positive departure early in the 20th century. Computation from the smoothed periodogram analysis indicated that about 31% of the variance of the reconstructed wtr series, 1647-1966, is at wavelengths greater than 10 years. For white noise, we would expect about 20% of the variance at wavelengths longer than 10 years (variance evenly distributed over the frequency range 0 to 0.5 yr⁻¹).

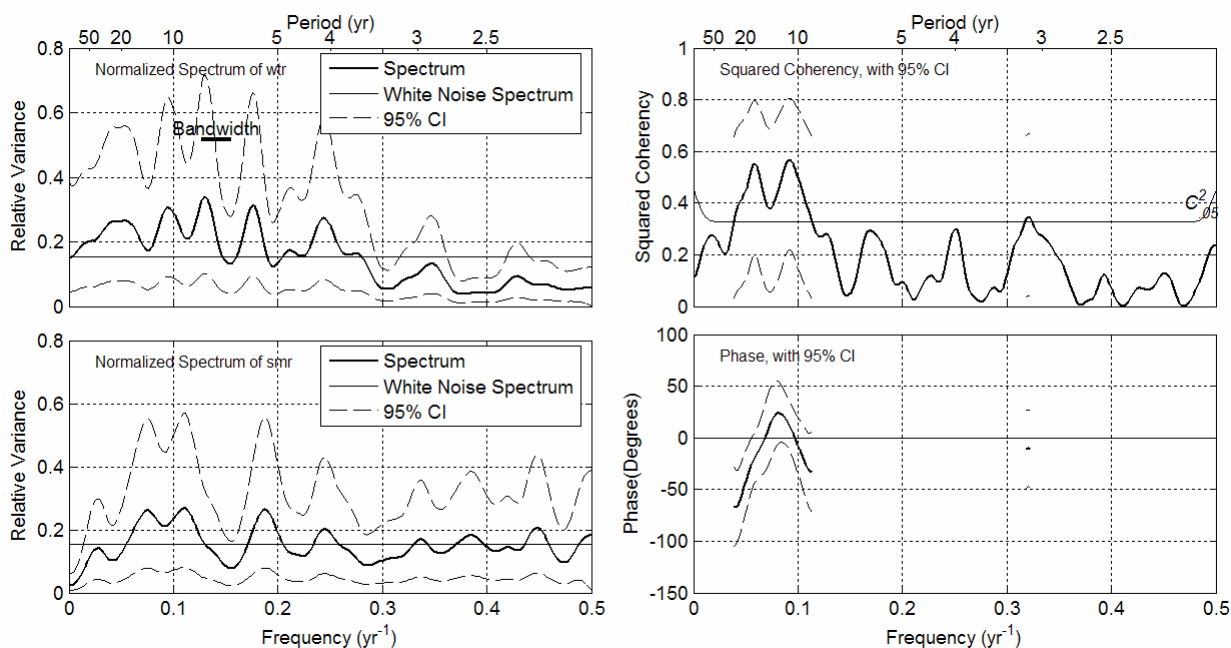


Figure 3. Summary plots of cross-spectral analysis of reconstructed winter (wtr) and summer (smr) precipitation for common period 1654-1966. Spectra are plotted at left, squared coherency at upper right, and phase at lower right. Method for the analysis was the smoothed periodogram (Bloomfield 2000)

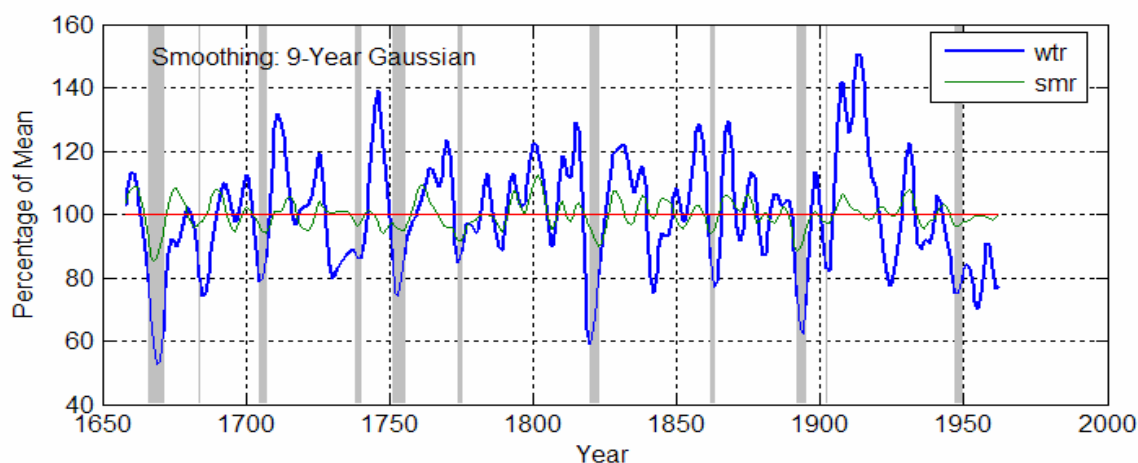


Figure 4. Time series of Gaussian-smoothed reconstructed wtr and smr precipitation. Filter weights: [0.0135 0.0477 0.1172 0.2012 0.2408 0.2012 0.1172 0.0477 0.0135]. Series expressed as percentage of common-period (1654-1966) means based on data before smoothing. Frequency response of filter is 0.50 at wavelength of about 8.7 years. Shading marks periods both smoothed series simultaneously below their 0.25 quantile.

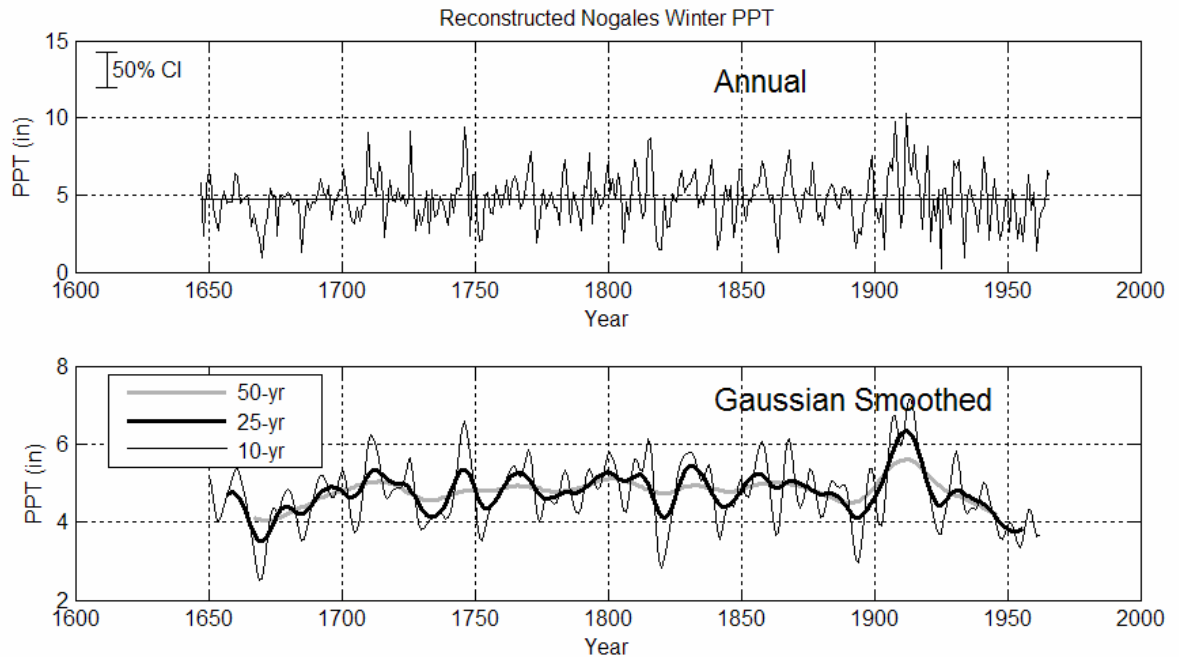


Figure 5. Long-term reconstructed time series of reconstructed winter Nogales precipitation. Top: unsmoothed annual values. Bottom: annual values smoothed by three different Gaussian filters with 50% frequency response at wavelengths 10, 25 and 50 years. Annotated 50% error bar for annual reconstructed values based on assumption that residuals are normally distributed with mean zero and standard deviation equal to the root-mean-square error of cross-validation. Filter weights listed in Appendix D.

Fidelity of Winter Frequency Response. Winter (wtr) is the only seasonal reconstruction with a high enough variance explained to merit detailed analysis. The observed and reconstructed series overlap for only a short period (1915-1966). Results of a cross-spectral analysis on the two series are summarized by the spectra and cross-spectra in Figure 6. The Gaussian-smoothed time series for the analysis period are plotted in Figure 7.

The spectra of the reconstructed and observed wtr series are quite similar (Figure 6, left). Neither contain any strong peaks, but both have greatest variance concentrated between around 4-5 years. There is no indication that the tree-ring reconstruction overestimates the low-frequency component of variance – and in fact at the lowest frequencies the spectrum of the reconstruction is below the white noise and the spectrum of the observed is above the white noise spectrum. Of course, with these exceedingly short time series the confidence bands are wide and little can be said about significance of variations.

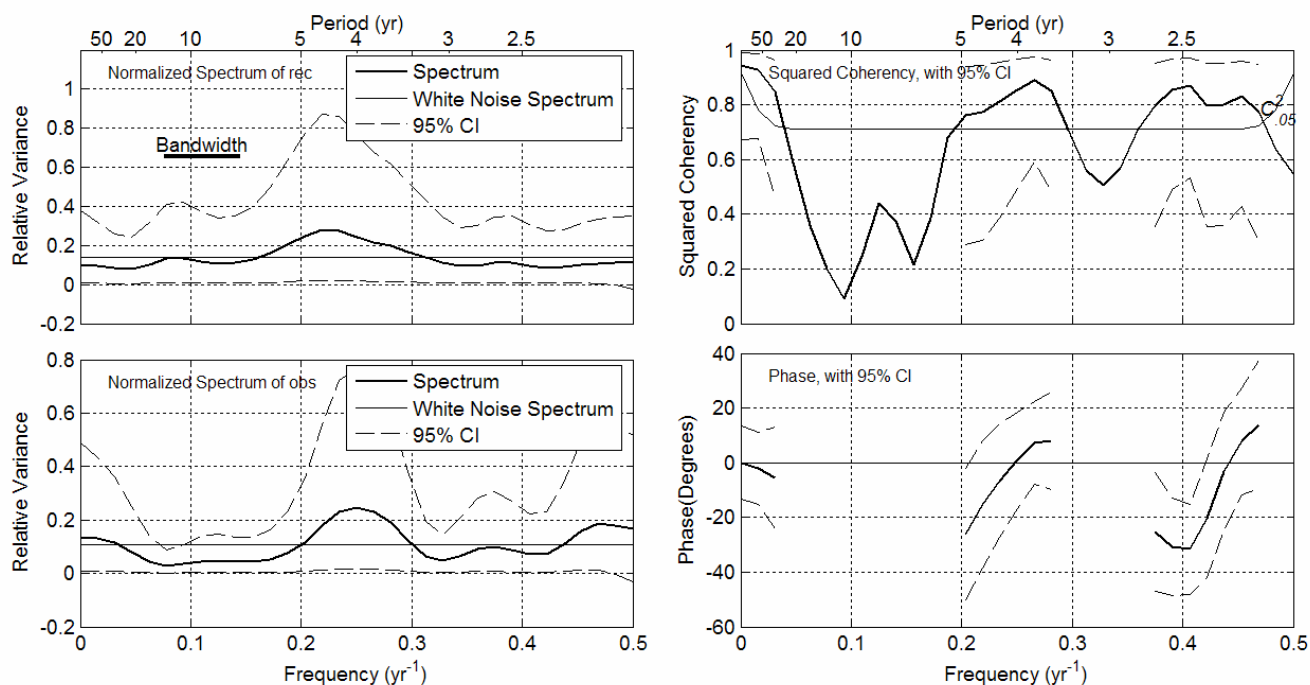


Figure 6. Summary plots of cross-spectral analysis of reconstructed and observed winter (wtr) precipitation for common period 1915-66. Spectra are plotted at left, squared coherency at upper right, and phase at lower right. Method for the analysis was the smoothed periodogram (Bloomfield 2000)

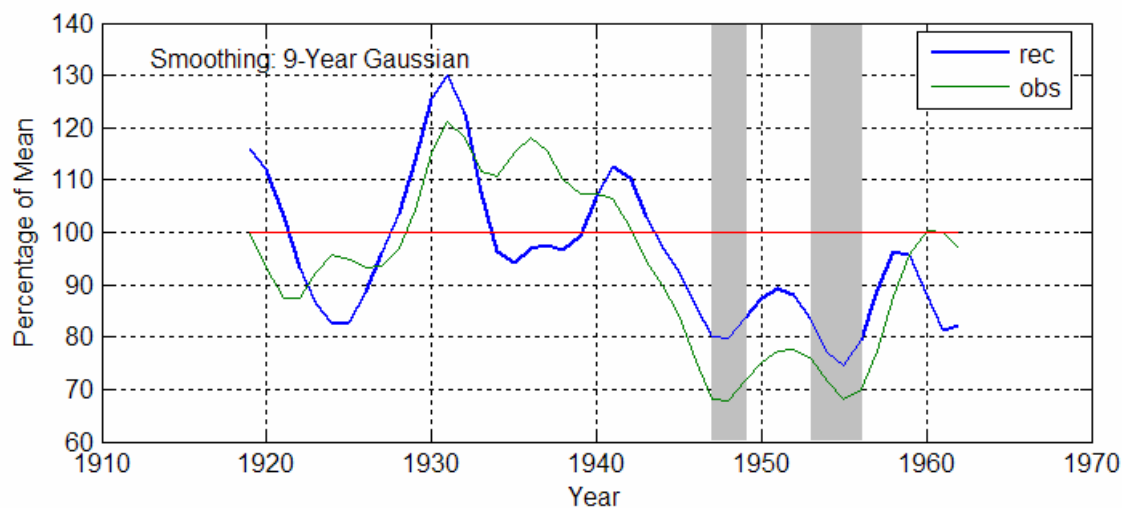


Figure 7. Gaussian-smoothed time series of reconstructed and observed wtr precipitation. Series plotted as percentage of mean of unsmoothed data for common period 1915-1966. Filter specifications same as in caption to Figure 4.

The observed and reconstructed series appear to be highly coherent and in-phase over most of the frequency axis. Where coherence does drop (centered on about 10 yr) the variance in the observed series is relatively low.

The Gaussian-smoothed time series of observed and reconstructed wtr likewise support the notion that the reconstruction can track variations in precipitation at low frequencies (Figure 7). Lows and highs in the two series occur at nearly the same time. The general downward trend over most of the observed record is also reflected in the reconstruction. Some discrepancies do occur – for example the failure to capture the minor wet peak in the 1930s. It should be emphasized, however, that even for this winter component the reconstruction accounts for just 57 % of the variance of the observed precipitations, and some departure is expected due to the unexplained variance.

CONSISTENCY WITH OTHER RECONSTRUCTIONS

“Task 4. Check the consistency of the reconstructed precipitation series with existing dendroclimatic reconstructions of gridpoint Palmer Drought Severity Index (PDSI) and divisional-average precipitation.”

Several existing tree-ring reconstruction of climate variables applicable to the southern Arizona region were examined to check the consistency of low-frequency fluctuations with those in reconstructed Nogales winter precipitation (wtr). The comparison series are described in the list below:

1. Gridpoint Palmer Drought Severity Index (Cook et al. 2004). These are reconstructions of summer-average (JJA) PDSI on a 2.5 x 2.5 degree grid over much of North America. The series used here is the nearest gridpoint to Nogales, 32.5N, 110W. This series has time coverage to A.D. 1. The reconstructions were derived from a large-scale network of more than 600 tree-ring chronologies, and the gridpoint reconstruction involves some spatial smoothing that might obscure localized variations in moisture. It should also be emphasized that although the reconstructed variable is summer PDSI, the reconstructions correspond most closely to variations in cool-season moisture conditions. This is because total ring width, the predictor variable for the PDSI reconstruction, responds most strongly to cool-season moisture variations. Lag effects in the PDSI computation (Palmer 1964) result in a built in persistence in PDSI from the cool season to the summer. T
2. Cool-season precipitation, San Pedro Basin, Arizona . (Meko 1997). This is a reconstruction of November-April precipitation from total-width tree-ring indices. The reconstruction was done as a sample application of a new reconstruction method, and did not utilize all existing tree-ring data from the region. The reconstruction extends back to A.D. 1271, but the period of reliable reconstruction goes back only to the mid-1600s (Meko 1997).

3. Cool-season precipitation, Arizona Climate Division 7. (Ni et al. 2002). This is a reconstruction of divisional-average November-April precipitation from a network of specially screened 1000-year long tree-ring chronologies, mostly from the Four Corners area. The screening was done with the view to retention of low-frequency climate information often removed in the conventional processing of tree-ring chronologies. The reconstruction is quite long, beginning in A.D. 1000, but the relevance to the Nogales precipitation record is perhaps marginal because the tree-rings sites are far from Nogales.

The low-frequency components of reconstructed wtr and the three other reconstruction are compared in the time series plots in Figure 8. Series have been converted to Z-scores before plotting to eliminate differences due to scale of variables. Reconstructed wtr appears most closely to track the reconstructed PDSI series, with major lows coinciding near 1670, 1730, 1820, 1890 and 1950. Least similar is the reconstructed Division 7 precipitation, which has several major features not shared with wtr (e.g., the drought near 1770).

A correlation analysis bears out the observations from the time series (Table 4). Reconstructed wtr correlates highly with the gridpoint PDSI series in both the unsmoothed ($r=0.79$) and smoothed data ($r=0.64$), and is least correlated at with reconstructed Division 7 precipitation. In summary, the reconstructed PDSI strongly corroborates the wtr reconstructions. The discrepancies with the Division 7 reconstruction can be explained by the remote location of the tree-ring sites from Nogales.

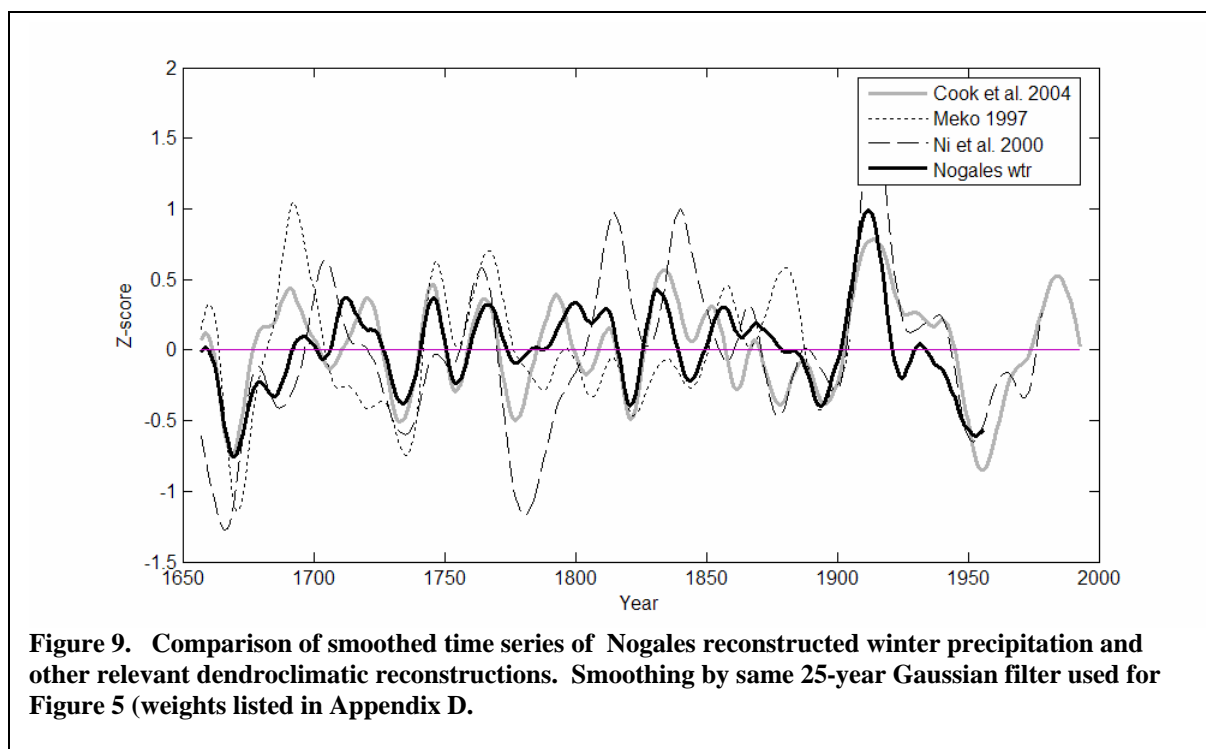


Table 4. Correlation of reconstructed winter Nogales precipitation¹ (wtr) with other tree-ring reconstructions², 1647-1966.

	PDSI	Div7 PPT	San Pedro PPT
Wtr(unsmoothed)	0.7915	0.5354	0.6686
Wtr(25-yr smoothed)	0.6402	0.3940	0.4683

¹Wtr is reconstructed Nov-Apr precipitation for Nogales; first row is the unsmoothed data; second row is the data smoothed with a 25-year Gaussian filter.

²PDSI is the gridpoint PDSI from Cook et al. (2004); Div7 PPT is Nov-Apr precipitation for Arizona climatic division 7 (Ni et al. 2002); San Pedro PPT is Nov-Apr precipitation for the San Pedro River Basin (Meko 1997).

CONCLUSIONS

1. Seasonal reconstructions of Nogales precipitation were generated from tree rings. The reconstructions are for winter (Nov-Mar), the dry season (Apr-June), summer (July-Sept), and the water year (Oct-Sept). A reconstruction was not done for October separately because there was no significant tree-ring signal for that single month's precipitation. Of the other reconstructions, winter is the only season with more than 50% of seasonal precipitation explained by tree rings. The winter reconstruction covers the period 1647-1966.
2. Reconstructed winter precipitation tracks the observed precipitation closely at low and high frequencies for the 1915-66 calibration period.
3. The long-term winter reconstructed precipitation appears to have a slightly lower-frequency spectrum than white noise, with no significant periodicities. The summer reconstructed precipitation is closer to white noise, but conclusions on the summer spectrum are perhaps not justified as the reconstruction explains only 11 percent of observed summer precipitation.
4. The low-frequency fluctuations in reconstructed winter precipitation are strongly consistent with variations in reconstructed gridpoint summer (JJA) Palmer Drought Severity Index over the common period 1647-1966. Both reconstructions probably reflect mostly the cool-season precipitation regime in Southern Arizona.
5. Data deliverables, including the seasonal precipitation reconstructions and the original tree-ring data used to derive them, have been organized into a spreadsheet (Tree_Ring_Study.xls) accompanying this report.

REFERENCES

- Bloomfield P. (2000) *Fourier analysis of time series: an introduction, second edition*. John Wiley & Sons, Inc., New York. 261 p.
- Cook E. R., Briffa K., Shiyatov S. and Mazepa V. (1990) Tree-ring standardization and growth-trend estimation. In *Methods of Dendrochronology, Applications in the Environmental Sciences* (ed E. R. Cook and L. A. Kairiukstis), pp. 104-123. Kluwer Academic Publishers.
- Cook E. R., Woodhouse C., Eakin C. M., Meko D. M. and Stahle D. W. (2004) Long-term aridity changes in the western United States. *Science* **306**, 1015-1018.
- Fritts H. C., Guiot J. and Gordon G. A. (1990) Verification. In *Methods of Dendrochronology, Applications in the Environmental Sciences* (ed E. R. Cook and L. A. Kairiukstis), pp. 178-185. Kluwer Academic Publishers.
- Gibson W., Daly C., Kittel T., Nychka D., Johns C., Rosenbloom N., McNab A. and Taylor G. (2002) Development of a 103-year high-resolution climate data set for the conterminous United States, pp. 181-183. Proc., 13th AMS Conf. on Applied Climatology, Amer. Meteorological Soc., Portland, OR, May 13-16.
- Ljung L. (1987) *System Identification: Theory for the User*. Prentice-Hall, Inc., Englewood Cliffs, NJ, 07632, 519 pp.
- Meko, D.M., 1997, Dendroclimatic reconstruction with time varying subsets of tree indices: *Journal of Climate*, v. 10, p. 687-696.
- Meko D. M. and Baisan C. H. (2001) Pilot study of latewood-width of conifers as an indicator of variability of summer rainfall in the north American Monsoon region. *International J. of Climatology* **21**, 697-708.
- Mitchell J. M., Jr., Dzerdzeevskii B., Flohn H., Hofmeyr W. L., Lamb H. H., Rao K. N. and Wallen C. C. (1966) Climatic change. Technical Note 79. World Meteorological Organization, Geneva.
- Ni F., Cavazos T., Hughes M. K., Comrie A. C. and Funkhouser G. (2002) Cool-season precipitation in the southwestern USA since A.D. 1000: comparison of linear and nonlinear techniques for reconstruction. *International Journal of Climatology* **22**, 1645-1662.
- Percival D. B. and Walden A. T. (1993) *Spectral analysis for physical applications*. Cambridge University Press.
- Snee R. D. (1977) Validation of regression models: methods and examples. *Technometrics* **19**, 415-428.
- Weisberg S. (1985) *Applied Linear Regression*, 2nd ed. John Wiley, New York, 324 pp.

Appendix A. *Summary of single-site regressions (screening of chronologies with precipitation data)*

This appendix contains tabular summaries of the autoregressive models used to prewhiten tree-ring chronologies, and the single-site regressions of seasonal precipitation on prewhitened chronologies. Individual tables A1-A4 list results for winter, dry, summer and water-year seasons.

Interpretation of the tables is illustrated by example. The first table, Table A1, summarizes results for the winter season. The first site listed is Pat Scott Peak, which according to the number in parentheses is also site #1 in the full listing of site information (Table 1 in text). The chronology was prewhitened with an autoregressive model of order 2, which explained 18.9 percent of the chronology variance. In the stepwise regression of winter precipitation on current and lagged values of the prewhitened tree-ring index, only lag 0 entered the model. The regression equation is statistically significant, with an overall F statistic of 5.5, which is significant at the 0.05 α -level. The model accounts for just 7 percent of the variance of precipitation in the calibration period. When the model was re-calibrated on the first half of data and used to predict the precipitation for the second half, the reduction of error statistic (RE) was 0.12; calibration on the second half and validation on the first half gave RE=0.04. Since positive RE is regarded as “some” skill (Fritts et al. 1990), the model is judged to successfully verify by this split-sample procedure.

Table A1. Summary of chronology persistence and precipitation signal, winter (Nov-Mar) season.

Chronology ¹		AR Model ²		Regression Model ³			RE ⁴	
N (N*)	Name	p	%var	Lags	R ²	F	A	B
1 (1)	PAT SCOTT PE	2	18.9	0	0.07	5.5*	0.12	0.04
2 (2)	SCHEELITE CA	3	38.1	0	0.41	55.3***	0.52	0.35
3 (3)	SANTA RITA M	2	28.2	0	0.31	21.6***	0.28	0.26
4 (4)	SANTA RITA	2	25.1	0	0.22	19.7***	0.35	0.15
5 (5)	MOUNT HOPKIN	2	20.2	0	0.21	18.9***	0.32	0.16
6 (6)	GREEN MOUNTI	2	22.0	0	0.24	21.8***	0.34	0.18
7 (7)	NORTH SLOPE	2	34.1	0	0.10	7.6**	0.12	0.09
8 (8)	GALIURO MTNS	3	18.3	0	0.53	54.8***	0.47	0.67
9 (9)	NORTH SLOPE	2	28.4	0	0.24	21.8***	0.24	0.25
10 (10)	HELEN'S DOME	3	23.5	0	0.08	6.0*	0.09	0.07
11 (11)	REEF OF ROCK	3	22.1	0, -1	0.17	8.6***	0.24	0.15
12 (12)	GREEN MOUNTA	3	32.5	0	0.12	9.8**	0.28	0.03
13 (15)	BEAR WALLOW	3	30.1	0, -1	0.12	9.7**	0.15	0.10
14 (16)	CHERRY CANYO	3	27.0	0	0.10	7.5**	0.15	0.08
15 (17)	SANTA CATALI	2	31.4	0, -1	0.24	8.5***	0.35	0.28
16 (19)	MT LEMMON	2	45.9	0, -1	0.17	13.7***	0.34	0.08
17 (20)	PADDYS RIVER	1	20.7	0, -1	0.40	25.7***	0.52	0.35
18 (21)	PADDYS RIVER	2	14.1	0, -1	0.19	9.3***	0.41	0.12
19 (23)	DOUGLAS CANY	1	14.6	0, -1	0.36	21.6***	0.52	0.30
20 (25)	TUCSON SIDE	2	25.4	0, -1	0.11	4.6*	0.28	0.07
21 (26)	PINERY CANYO	1	12.7	0	0.24	22.1***	0.22	0.28
22 (27)	FLY PEAK CH	2	35.8	0	0.27	24.8***	0.29	0.28
23 (28)	PETER'S FLAT	3	33.7	0	0.17	15.4***	0.17	0.18
24 (30)	NOON CREEK	3	35.7	0, -2, -3	0.14	11.4**	0.19	0.13
25 (31)	RHYOLITE CAN	3	12.2	0	0.08	5.8*	0.04	0.12
26 (32)	EMERALD PEAK	3	28.3	0	0.07	5.3*	0.07	0.07
27 (33)	MOUNT GRAHAM	2	18.0	0	0.22	21.0***	0.25	0.21
28 (34)	RHYOLITE CAN	2	10.3	0	0.33	34.7***	0.29	0.42
29 (35)	POST CREEK	2	23.1	0	0.23	21.1***	0.22	0.25
30 (36)	CAMP POINT,	3	20.6	0	0.16	13.6***	0.13	0.20
31 (37)	LADYBUG PEAK	1	18.0	0, -1	0.35	26.8***	0.37	0.25
32 (38)	CLARK PEAK S	1	24.8	0, -1	0.40	17.1***	0.49	0.40
33 (39)	DOUGLAS CANY	2	13.1	0, -1	0.35	40.1***	0.48	0.26
34 (40)	PADDYS RIVER	2	14.0	0, -1	0.40	51.9***	0.54	0.33
35 (41)	RHYOLITE CAN	0	0.0	0	0.39	48.6***	0.38	0.43
36 (42)	RINCON PEAK	2	10.8	0, -1	0.32	38.4***	0.43	0.28
37 (43)	SCHEELITE CA	2	12.8	0, -1	0.51	41.9***	0.62	0.47

¹Site number (site number in Table 1), and chronology name

²AR model: persistence properties of standard chronology:

p = order of autoregressive model

%var = percent of chronology variance due to modeled persistence

³regression modeling specifications and statistics:

Lags = lags included on predictors

R2 = variance explained by regression, adjusted

F = overall F-level and significance (*, **, *** indicate 0.05, 0.01 and 0.001 alpha-levels)

⁴Reduction of error statistic for split sample validation;

A = validation on second half of data (calibration on first)

B = validation on first half of data (calibration on second)

Table A2. Summary of chronology persistence and precipitation signal, dry (April-June) season.

Chronology ¹		AR Model ²		Regression Model ³			RE ⁴	
N (N*)	Name	p	%var	Lags	R ²	F	A	B
1 (1)	PAT SCOTT PE	2	18.9	0,-1	0.09	7.3**	0.08	0.09
2 (4)	SANTA RITA	2	25.1	0	0.08	6.1*	0.08	0.08
3 (7)	NORTH SLOPE	2	34.1	0,1	0.11	9.2**	0.11	0.13
4 (8)	GALIURO MTNS	3	18.3	0,1	0.18	5.8**	0.20	0.12
5 (9)	NORTH SLOPE	2	28.4	0	0.14	11.5**	0.15	0.15
6 (10)	HELEN'S DOME	3	23.5	0	0.12	10.1**	0.13	0.12
7 (11)	REEF OF ROCK	2	12.2	0	0.13	12.2***	0.07	0.18
8 (13)	NORTH SLOPE	3	29.0	0	0.10	7.8**	0.10	0.10
9 (14)	DEVIL'S BATH	2	12.8	0	0.10	7.9**	0.11	0.09
10 (15)	BEAR WALLOW	3	30.1	0,-1,1	0.06	4.6*	0.11	0.02
11 (19)	MT LEMMON	2	45.9	0	0.10	7.7**	0.10	0.14
12 (20)	PADDYS RIVER	1	20.7	0,1	0.09	7.7**	0.05	0.15
13 (24)	TUCSON SIDE	2	25.0	0	0.09	7.0*	0.04	0.18
14 (25)	TUCSON SIDE	2	25.4	0	0.10	7.5**	0.13	0.06
15 (26)	PINERY CANYO	1	12.7	0,1	0.10	7.9**	0.14	0.06
16 (28)	PETER'S FLAT	3	33.7	0	0.06	4.7*	0.15	0.01
17 (31)	RHYOLITE CAN	3	12.2	0,1	0.09	7.3**	0.08	0.09
18 (32)	EMERALD PEAK	3	28.3	0,1	0.11	5.2**	0.28	0.03
19 (36)	CAMP POINT,	3	17.9	0	0.06	4.8*	0.08	0.04
20 (40)	PADDYS RIVER	2	14.0	0,-1,1	0.08	7.1**	0.04	0.14
21 (41)	RHYOLITE CAN	0	0.0	0,1	0.12	5.4**	0.10	0.16
22 (42)	RINCON PEAK	2	10.8	0,1	0.11	5.7**	0.05	0.27

¹Site number (site number in Table 1), and chronology name

²AR model: persistence properties of standard chronology:

p = order of autoregressive model

%var = percent of chronology variance due to modeled persistence

³regression modeling specifications and statistics:

Lags = lags included on predictors

R2 = variance explained by regression, adjusted

F = overall F-level and significance (*, **, *** indicate 0.05, 0.01 and 0.001 alpha-levels)

⁴Reduction of error statistic for split sample validation;

A = validation on second half of data (calibration on first)

B = validation on first half of data (calibration on second)

Table A3. Summary of chronology persistence and precipitation signal, summer (July-Sept) season.

Chronology ¹		AR Model ²		Regression Model ³			RE ⁴	
N (N*)	Name	p	%var	Lags	R ²	F	A	B
1 (12)	GREEN MOUNTA	3	32.8	0, -3	0.10	7.9**	0.10	0.09
2 (18)	HELEN'S DOME	3	36.3	0	0.10	8.2**	0.08	0.16
3 (25)	TUCSON SIDE	2	25.4	0	0.07	5.5*	0.08	0.07
4 (46)	RHYOLITE CAN	2	1.0	0	0.11	9.3**	0.00	0.33

¹Site number (site number in Table 1), and chronology name

²AR model: persistence properties of standard chronology:

p = order of autoregressive model

%var = percent of chronology variance due to modeled persistence

³Regression modeling specifications and statistics:

Lags = lags included on predictors

R² = variance explained by regression, adjusted

F = overall F-level and significance (*, **, *** indicate 0.05, 0.01 and 0.001 alpha-levels)

⁴Reduction of error statistic for split sample validation;

A = validation on second half of data (calibration on first)

B = validation on first half of data (calibration on second)

Table A4. Summary of chronology persistence and precipitation signal, water-year (October–September) season.

Chronology ¹		AR Model ²		Regression Model ³			RE ⁴	
N (N*)	Name	p	%var	Lags	R ²	F	A	B
1 (1)	PAT SCOTT PE	2	18.9	0	0.07	5.9*	0.09	0.08
2 (2)	SCHEELITE CA	3	38.1	0,-2	0.18	9.3***	0.20	0.18
3 (3)	SANTA RITA M	2	28.2	0	0.14	7.9**	0.09	0.16
4 (4)	SANTA RITA	2	25.1	0,-3	0.13	5.7**	0.23	0.10
5 (5)	MOUNT HOPKIN	2	20.2	0,-3	0.24	22.1***	0.16	0.29
6 (6)	GREEN MOUNTI	2	22.0	0,-3	0.19	8.7***	0.41	0.08
7 (7)	NORTH SLOPE	2	34.1	0,-3	0.08	6.3*	0.17	0.06
8 (8)	GALIURO MTNS	3	18.3	0	0.29	19.3***	0.29	0.23
9 (9)	NORTH SLOPE	2	28.4	0,-3	0.24	11.4***	0.29	0.22
10 (10)	HELEN'S DOME	3	23.5	0	0.09	6.7*	0.17	0.04
11 (11)	REEF OF ROCK	3	22.1	0	0.08	7.1**	0.18	0.03
12 (12)	GREEN MOUNTA	3	32.5	0	0.14	11.5**	0.29	0.07
13 (14)	DEVIL'S BATH	2	12.8	0,-2	0.11	4.9*	0.22	0.08
14 (15)	BEAR WALLOW	3	30.1	0,-3	0.11	4.9*	0.19	0.08
15 (16)	CHERRY CANYO	3	27.0	0	0.17	14.6***	0.21	0.13
16 (17)	SANTA CATALI	2	31.4	0,-3	0.09	4.8*	0.08	0.10
17 (18)	HELEN'S DOME	3	36.3	0	0.09	6.9*	0.26	0.03
18 (19)	MT LEMMON	2	45.9	0,-3	0.24	10.9***	0.43	0.11
19 (20)	PADDYS RIVER	1	20.7	0,-1	0.17	16.1***	0.25	0.14
20 (21)	PADDYS RIVER	2	14.1	0	0.09	7.6**	0.14	0.06
21 (22)	NORTH SLOPE	2	26.8	0	0.06	4.7*	0.20	0.02
22 (23)	DOUGLAS CANY	1	14.6	0,-1	0.08	6.9*	0.28	0.01
23 (24)	TUCSON SIDE	2	25.0	0,-3	0.15	6.9**	0.15	0.18
24 (25)	TUCSON SIDE	2	25.4	0	0.14	11.2**	0.39	0.03
25 (26)	PINERY CANYO	1	12.7	0	0.12	9.1**	0.19	0.10
26 (27)	FLY PEAK CH	2	35.8	0	0.10	7.2**	0.25	0.02
27 (28)	PETER'S FLAT	3	33.7	0,-1,-3	0.12	5.5**	0.20	0.09
28 (31)	RHYOLITE CAN	3	12.2	0	0.09	6.8*	0.14	0.11
29 (32)	EMERALD PEAK	3	28.3	0	0.08	6.5*	0.12	0.05
30 (33)	MOUNT GRAHAM	2	18.0	0,-2	0.15	12.4***	0.20	0.10
31 (34)	RHYOLITE CAN	2	10.3	0	0.14	11.7**	0.18	0.17
32 (35)	POST CREEK	2	23.1	0,-3	0.18	7.9***	0.33	0.11
33 (36)	CAMP POINT,	3	20.6	0,-2,-3	0.22	10.5***	0.30	0.19
34 (37)	LADYBUG PEAK	1	18.0	0,-3	0.23	14.5***	0.35	0.07
35 (38)	CLARK PEAK S	1	24.8	0,-3	0.15	9.2**	0.31	0.05
36 (39)	DOUGLAS CANY	2	13.1	0,-1	0.10	8.9**	0.23	0.04
37 (40)	PADDYS RIVER	2	14.0	0,-1,1	0.16	14.9***	0.33	0.08
38 (41)	RHYOLITE CAN	0	0.0	0	0.15	13.1***	0.25	0.13
39 (42)	RINCON PEAK	2	10.8	0	0.15	13.8***	0.27	0.08
40 (43)	SCHEELITE CA	2	12.8	0	0.14	12.5***	0.20	0.10
41 (46)	RHYOLITE CAN	2	1.0	0	0.06	5.0*	0.00	0.19

¹Site number (site number in Table 1), and chronology name

²AR model: persistence properties of standard chronology:

p = order of autoregressive model

%var = percent of chronology variance due to modeled persistence

³Regression modeling specifications and statistics:

Lags = lags included on predictors

R² = variance explained by regression, adjusted

F = overall F-level and significance (*, **, *** indicate 0.05, 0.01 and 0.001 alpha-levels)

⁴Reduction of error statistic for split sample validation;

A = validation on second half of data (calibration on first)

B = validation on first half of data (calibration on second)

Appendix B. *Summary of multi-site regression models used to generate final reconstructions*

This appendix contains tabular summaries of the stepwise regression models for final seasonal reconstructions of seasonal precipitation. Tables B1-B4 apply to winter, dry, summer and water-year seasons. Columns are defined in the footnotes below the tables.

The estimated equation for regression of seasonal precipitation on PCs of single-site reconstructions is listed below the footnotes for each table. For example, for the winter season, the reconstruction equation is

$$\hat{y} = 4.742 + 0.31753X_1 + 0.53267X_3$$

where \hat{y} is the estimated precipitation in a given year (inches), X_1 is the score of principal component 1 in that year, and X_3 is the score of principal component 3 in that year. The principal components themselves are linear combinations of single-site reconstructions generated from each tree-ring chronology (see text). The weights of the principal components on the chronologies are listed in Appendix C. The information for the reconstruction model includes the 95% confidence interval for the regression coefficients (CI), the R^2 of regression, the F -level for the equation, and the significance of that computed F -level, equivalent to the p -value of the computed F . The root-mean-square error of the cross-validation of the regression equation is also given (RMSE_{cv}). RMSE_{cv} is a measure, in inches, of the uncertainty of the estimated precipitation. The true precipitation should lie approximately within $\pm 2\text{RMSE}_{cv}$ of the reconstructed value 95% of the time.

Table B1. Summary of stepwise regression model for final reconstruction, winter (wtr) season.

Step	Variables ¹	R ² adj	RE Statistic ²			RMSEcv ³	Residuals ⁴		
			A	B	cv		r ₁	T	N
1	1	0.49	0.55	0.51	0.46	1.7740	P	0	F
2*	1,3	0.57	0.41	0.57	0.50	1.6947	P	0	F
3	1,2,3	0.56	0.38	0.57	0.50	1.7097	P	0	F

¹Principal components (covariance matrix) of single-site reconstructions entering at each step in the stepwise regression. Final step for reconstruction model marked by "*". Variables are the numbered principal components (e.g., variable "1" is PC 1, the component explaining the most variance in the PCA of single-site reconstructions.

²Reduction of error statistic from (A) calibration on 1915-1940 and validation on 1941-1966, (B) calibration on 1941-1966 and validation on 1915-1940, (cv)cross-validation with 7 observations left out at each iteration

³Root-mean-square error of cross-validation

⁴Analysis of residuals: Column labeled "r₁" list results of Durbin-Watson test for first-order autocorrelation of residuals; "T" is test for significance of slope of a regression of regression residuals on time (trend); "N" is Lilliefors test for normality of residuals; "P" or "F" for Durbin-Watson or Lilliefors test indicates "pass" or "fail" ("pass" means the test statistic not significant at 0.05 alpha-level); 0 for the trend test indicates slope of trend line not significant at 0.05 level, while - or + indicates significant negative or positive trend in residuals

Model Equation

Var	Coef	95% CI	
Con	4.742	(4.2779	5.206)
X1	0.31753	(0.23506	0.39999)
X3	0.53267	(0.19059	0.87475)

R-squared = 0.57448

F-level = 33.0761

sig = 8.102830E-0109

RMSEcv = 1.6947

Table B2. Summary of stepwise regression model for final reconstruction, April-June (dry) season.

Step	Variables ¹	R ² adj	RE Statistic ²			RMSEcv ³	Residuals ⁴		
			A	B	cv		r ₁	T	N
1	1	0.14	0.16	0.15	0.09	0.7229	P	0	F
2*	1,2	0.19	0.25	0.24	0.13	0.7082	P	0	F
3	1,2,3	0.22	0.21	0.27	0.13	0.7077	P	0	F
4	1,2,3,4	0.22	-0.02	0.09	0.12	0.7136	P	0	F

¹Principal components (covariance matrix) of single-site reconstructions entering at each step in the stepwise regression. Final step for reconstruction model marked by "*". Variables are the numbered principal components (e.g., variable "1" is PC 1, the component explaining the most variance in the PCA of single-site reconstructions.

²Reduction of error statistic from (A) calibration on 1914-1948 and validation on 1949-1983, (B) calibration on 1949-1983 and validation on 1914-1948, (cv)cross-validation with 5 observations left out at each iteration

³Root-mean-square error of cross-validation

⁴Analysis of residuals: Column labeled "r₁" list results of Durbin-Watson test for first-order autocorrelation of residuals; "T" is test for significance of slope of a regression of regression residuals on time (trend); "N" is Lilliefors test for normality of residuals; "P" or "F" for Durbin-Watson or Lilliefors test indicates "pass" or "fail" ("pass" means the test statistic not significant at 0.05 alpha-level); 0 for the trend test indicates slope of trend line not significant at 0.05 level, while - or + indicates significant negative or positive trend in residuals

Model Equation

Var	Coef	95% CI	
Con	0.87863	(0.71317	1.0441)
X1	0.45067	(0.19929	0.70205)
X2	0.52637	(0.075323	0.97742)

R-squared = 0.20393

F-level = 8.5817

sig = 4.807172E-0049

RMSEcv = 0.70824

Table B3. Summary of stepwise regression model for final reconstruction, summer (smr) season.

Step	Variables ¹	R ² adj	RE Statistic ²			RMSEcv ³	Residuals ⁴		
			A	B	cv		r ₁	T	N
1	1*	0.11	0.08	-0.21	0.05	2.7547	P	0	P
2	1,2	0.12	-0.02	-0.19	0.04	2.7714	P	0	P

¹Principal components (covariance matrix) of single-site reconstructions entering at each step in the stepwise regression. Final step for reconstruction model marked by "*". Variables are the numbered principal components (e.g., variable "1" is PC 1, the component explaining the most variance in the PCA of single-site reconstructions.

²Reduction of error statistic from (A) calibration on 1914-1952 and validation on 1953-1992, (B) calibration on 1953-1992 and validation on 1914-1952, (cv)cross-validation with 7 observations left out at each iteration

³Root-mean-square error of cross-validation

⁴Analysis of residuals: Column labeled "r₁" list results of Durbin-Watson test for first-order autocorrelation of residuals; "T" is test for significance of slope of a regression of regression residuals on time (trend); "N" is Lilliefors test for normality of residuals; "P" or "F" for Durbin-Watson or Lilliefors test indicates "pass" or "fail" ("pass" means the test statistic not significant at 0.05 alpha-level); 0 for the trend test indicates slope of trend line not significant at 0.05 level, while - or + indicates significant negative or positive trend in residuals

Model Equation

Var	Coef	95% CI	
Con	9.785	(9.17857	10.3914)
X1	0.97026	(0.339774	1.60075)

R-squared = 0.1087

F-level = 9.3903

sig = 3.006446E-0039

RMSEcv = 2.7547

Table B4. Summary of stepwise regression model for final reconstruction, water-year (wyr) season.

Step	Variables ¹	R ² adj	RE Statistic ²			RMSEcv ³	Residuals ⁴		
			A	B	cv		r ₁	T	N
1*	1	0.33	0.29	0.39	0.28	3.3826	P	0	P

¹Principal components (covariance matrix) of single-site reconstructions entering at each step in the stepwise regression. Final step for reconstruction model marked by "*". Variables are the numbered principal components (e.g., variable "1" is PC 1, the component explaining the most variance in the PCA of single-site reconstructions.

²Reduction of error statistic from (A) calibration on 1915-1940 and validation on 1941-1966, (B) calibration on 1941-1966 and validation on 1915-1940, (cv)cross-validation with 9 observations left out at each iteration

³Root-mean-square error of cross-validation

⁴Analysis of residuals: Column labeled "r₁" list results of Durbin-Watson test for first-order autocorrelation of residuals; "T" is test for significance of slope of a regression of regression residuals on time (trend); "N" is Lilliefors test for normality of residuals; "P" or "F" for Durbin-Watson or Lilliefors test indicates "pass" or "fail" ("pass" means the test statistic not significant at 0.05 alpha-level); 0 for the trend test indicates slope of trend line not significant at 0.05 level, while - or + indicates significant negative or positive trend in residuals

Model Equation

Var	Coef	95% CI	
Con	15.8061	(14.8784	16.7339)
X1	0.396809	(0.235778	0.557841)

R-squared = 0.32883

F-level = 24.4969

sig = 8.849441E-0069

RMSEcv = 3.3826

Appendix C. *PC loadings and equivalent regression weights on chronologies.*

This appendix contains tables listing the loadings of the principal components of tree-ring chronologies used in the seasonal precipitation reconstructions. The tables also give the equivalent weights of the reconstruction equation on individual chronologies. Tables C1-C4 apply to winter, dry, summer and water-year seasons.

Table C1. PC loadings and equivalent regression weights on chronologies, winter (wtr) season.

N ¹	CHRONOLOGY	LOADINGS ²		WEIGHTS ³	
		X1	X3	W	W*
1 (1)	PAT SCOTT PE	0.083	-0.102	-0.0081	-0.03
2 (2)	SCHEELITE CA	0.268	0.063	0.0785	0.29
3 (3)	SANTA RITA M	0.164	-0.113	-0.0043	-0.02
4 (4)	SANTA RITA	0.206	-0.159	-0.0110	-0.04
5 (6)	GREEN MOUNTI	0.189	-0.101	0.0038	0.01
6 (7)	NORTH SLOPE	0.146	-0.162	-0.0150	-0.06
7 (11)	REEF OF ROCK	0.176	0.108	0.0521	0.20
8 (12)	GREEN MOUNTA	0.134	-0.118	-0.0085	-0.03
9 (15)	BEAR WALLOW	0.136	-0.151	-0.0161	-0.06
10 (17)	SANTA CATALI	0.180	0.079	0.0503	0.19
11 (19)	MT LEMMON	0.143	-0.188	-0.0240	-0.09
12 (20)	PADDYS RIVER	0.336	0.442	0.2669	1.00
13 (21)	PADDYS RIVER	0.200	0.354	0.1394	0.52
14 (28)	PETER'S FLAT	0.145	-0.288	-0.0510	-0.19
15 (31)	RHYOLITE CAN	0.109	-0.147	-0.0139	-0.05
16 (34)	RHYOLITE CAN	0.220	-0.121	0.0038	0.01
17 (35)	POST CREEK	0.205	-0.299	-0.0504	-0.19
18 (36)	CAMP POINT,	0.179	-0.333	-0.0548	-0.21
19 (37)	LADYBUG PEAK	0.214	-0.129	-0.0005	-0.00
20 (38)	CLARK PEAK S	0.202	-0.017	0.0355	0.13
21 (40)	PADDYS RIVER	0.283	0.167	0.1394	0.52
22 (41)	RHYOLITE CAN	0.241	-0.075	0.0250	0.09
23 (42)	RINCON PEAK	0.226	-0.022	0.0412	0.15
24 (43)	SCHEELITE CA	0.301	0.360	0.2319	0.87

¹Sequential number of chronology used in this reconstruction, with the site number in parentheses for cross reference to full site-information table (Table 1 in text)

²Loadings. Column "Xi" lists the loadings of the ith principal component on the single-site reconstructions (filtered and scaled chronologies). The final, or multi-site, reconstruction was generated by regression of flow on the PC scores

³The final reconstruction can alternatively be expressed in terms of the single-site reconstructions for the individual chronologies. The applicable weights to generate the reconstruction from the single-site reconstructions are listed in column "W". Column "W*" lists the same weights proportionally scaled so that the largest weight is 1.0. The weights W and W* measure the relative importance of the individual chronologies to the final reconstruction. The site with a weight W*=1.0 is the most important in terms of being most heavily weighted in the reconstruction.

The final reconstruction can be generated from the original standard tree-ring chronologies by the following steps:

1. filter and scale the original chronologies into single-site reconstructions of seasonal precipitation as described in the text of the report
2. Convert the single-site reconstructions to Z-scores by subtracting the calibration-period mean and dividing by the calibration-period standard deviation
3. Multiply the Z-score series by the regression weights in next-to-last column (W) above
4. Restore the calibration-period mean and standard deviation (multiply time series from (3) by the calibration-period standard deviation and add the calibration-period mean

Table C2. PC loadings and equivalent regression weights on chronologies, April-June (dry) season.

N ¹	CHRONOLOGY	LOADINGS ²		WEIGHTS ³	
		X1	X3	W	W*
1 (1)	PAT SCOTT PE	0.217	-0.050	0.0214	0.17
2 (4)	SANTA RITA	0.288	-0.038	0.0322	0.26
3 (7)	NORTH SLOPE	0.396	-0.081	0.0467	0.37
4 (11)	REEF OF ROCK	0.367	-0.126	0.0389	0.31
5 (15)	BEAR WALLOW	0.221	-0.061	0.0172	0.14
6 (19)	MT LEMMON	0.283	-0.095	0.0248	0.20
7 (20)	PADDYS RIVER	0.324	-0.062	0.0365	0.29
8 (26)	PINERY CANYO	0.023	0.523	0.0914	0.73
9 (28)	PETER'S FLAT	0.209	-0.092	0.0118	0.09
10 (31)	RHYOLITE CAN	0.038	0.628	0.1065	0.85
11 (36)	CAMP POINT,	0.273	-0.114	0.0165	0.13
12 (40)	PADDYS RIVER	0.268	-0.042	0.0303	0.24
13 (41)	RHYOLITE CAN	0.252	0.456	0.1247	1.00
14 (42)	RINCON PEAK	0.298	0.241	0.0927	0.74

¹Sequential number of chronology used in this reconstruction, with the site number in parentheses for cross reference to full site-information table (Table 1 in text)

²Loadings. Column "Xi" lists the loadings of the ith principal component on the single-site reconstructions (filtered and scaled chronologies). The final, or multi-site, reconstruction was generated by regression of flow on the PC scores

³The final reconstruction can alternatively be expressed in terms of the single-site reconstructions for the individual chronologies. The applicable weights to generate the reconstruction from the single-site reconstructions are listed in column "W". Column "W*" lists the same weights proportionally scaled so that the largest weight is 1.0. The weights W and W* measure the relative importance of the individual chronologies to the final reconstruction. The site with a weight W*=1.0 is the most important in terms of being most heavily weighted in the reconstruction.

The final reconstruction can be generated from the original standard tree-ring chronologies by the following steps:

1. filter and scale the original chronologies into single-site reconstructions of seasonal precipitation as described in the text of the report
2. Convert the single-site reconstructions to Z-scores by subtracting the calibration-period mean and dividing by the calibration-period standard deviation
3. Multiply the Z-score series by the regression weights in next-to-last column (W) above
4. Restore the calibration-period mean and standard deviation (multiply time series from (3) by the calibration-period standard deviation and add the calibration-period mean

Table C3. PC loadings and equivalent regression weights on chronologies, summer (smr) season.

N ¹	CHRONOLOGY	LOADINGS ²	WEIGHTS ³	
		X1	W	W*
1 (44)	DOUGLAS CANY	0.107	0.0088	0.03
2 (45)	PADDYS RIVER	0.004	0.0004	0.00
3 (46)	RHYOLITE CAN	0.969	0.3112	1.00
4 (47)	RINCON PEAK	0.219	0.0350	0.11
5 (48)	SCHEELITE CA	0.032	0.0056	0.02

¹Sequential number of chronology used in this reconstruction, with the site number in parentheses for cross reference to full site-information table (Table 1 in text)

²Loadings. Column "Xi" lists the loadings of the ith principal component on the single-site reconstructions (filtered and scaled chronologies). The final, or multi-site, reconstruction was generated by regression of flow on the PC scores

³The final reconstruction can alternatively be expressed in terms of the single-site reconstructions for the individual chronologies. The applicable weights to generate the reconstruction from the single-site reconstructions are listed in column "W". Column "W*" lists the same weights proportionally scaled so that the largest weight is 1.0. The weights W and W* measure the relative importance of the individual chronologies to the final reconstruction. The site with a weight W*=1.0 is the most important in terms of being most heavily weighted in the reconstruction.

The final reconstruction can be generated from the original standard tree-ring chronologies by the following steps:

1. filter and scale the original chronologies into single-site reconstructions of seasonal precipitation as described in the text of the report
2. Convert the single-site reconstructions to Z-scores by subtracting the calibration-period mean and dividing by the calibration-period standard deviation
3. Multiply the Z-score series by the regression weights in next-to-last column (W) above
4. Restore the calibration-period mean and standard deviation (multiply time series from (3) by the calibration-period standard deviation and add the calibration-period mean

Table C4. PC loadings and equivalent regression weights on chronologies, Water-year (wyr) season.

N ¹	CHRONOLOGY	LOADINGS ²	WEIGHTS ³	
		X1	W	W*
1 (1)	PAT SCOTT PE	0.126	0.0142	0.18
2 (2)	SCHEELITE CA	0.223	0.0389	0.49
3 (3)	SANTA RITA M	0.152	0.0207	0.26
4 (4)	SANTA RITA	0.246	0.0451	0.57
5 (6)	GREEN MOUNTI	0.273	0.0594	0.75
6 (7)	NORTH SLOPE	0.194	0.0261	0.33
7 (11)	REEF OF ROCK	0.161	0.0183	0.23
8 (12)	GREEN MOUNTA	0.218	0.0374	0.47
9 (15)	BEAR WALLOW	0.220	0.0371	0.47
10 (17)	SANTA CATALI	0.065	0.0076	0.10
11 (19)	MT LEMMON	0.262	0.0499	0.63
12 (20)	PADDYS RIVER	0.268	0.0521	0.66
13 (21)	PADDYS RIVER	0.199	0.0280	0.35
14 (28)	PETER'S FLAT	0.215	0.0348	0.44
15 (31)	RHYOLITE CAN	0.171	0.0224	0.28
16 (34)	RHYOLITE CAN	0.186	0.0319	0.40
17 (35)	POST CREEK	0.307	0.0565	0.72
18 (36)	CAMP POINT,	0.375	0.0790	1.00
19 (37)	LADYBUG PEAK	0.240	0.0452	0.57
20 (38)	CLARK PEAK S	0.173	0.0270	0.34

¹Sequential number of chronology used in this reconstruction, with the site number in parentheses for cross reference to full site-information table (Table 1 in text)

²Loadings. Column "Xi" lists the loadings of the ith principal component on the single-site reconstructions (filtered and scaled chronologies). The final, or multi-site, reconstruction was generated by regression of flow on the PC scores

³The final reconstruction can alternatively be expressed in terms of the single-site reconstructions for the individual chronologies. The applicable weights to generate the reconstruction from the single-site reconstructions are listed in column "W". Column "W*" lists the same weights proportionally scaled so that the largest weight is 1.0. The weights W and W* measure the relative importance of the individual chronologies to the final reconstruction. The site with a weight W*=1.0 is the most important in terms of being most heavily weighted in the reconstruction.

The final reconstruction can be generated from the original standard tree-ring chronologies by the following steps:

1. filter and scale the original chronologies into single-site reconstructions of seasonal precipitation as described in the text of the report
2. Convert the single-site reconstructions to Z-scores by subtracting the calibration-period mean and dividing by the calibration-period standard deviation
3. Multiply the Z-score series by the regression weights in next-to-last column (W) above
4. Restore the calibration-period mean and standard deviation (multiply time series from (3) by the calibration-period standard deviation and add the calibration-period mean

Appendix D. *Weights of Gaussian filters used in the report.*

Below are listings of weights for the 50-yr, 25-yr and 10-yr Gaussian filters used to smooth the annual reconstructed values in the report. The filter weights were computed as recommended by Mitchell et al. (1966).

Wt. No.	50-yr	25-yr	10-yr
1	0.00272504914622	0.00543740766513	0.01351956901598
2	0.00360847939456	0.00939805182508	0.04766217910887
3	0.00470999319516	0.01533445742017	0.11723004402070
4	0.00605985858053	0.02362020323623	0.20116755999376
5	0.00768512362400	0.03434657878936	0.24084129572137
6	0.00960694681421	0.04714851036952	0.20116755999376
7	0.01183766578240	0.06109942254464	0.11723004402070
8	0.01437781600161	0.07474650199670	0.04766217910887
9	0.01721337096090	0.08632354732381	0.01351956901598
10	0.02031351571484	0.09411358606158	
11	0.02362927627296	0.09686346553554	
12	0.02709329995710	0.09411358606158	
13	0.03062101271303	0.08632354732381	
14	0.03411327017440	0.07474650199670	
15	0.03746047822666	0.06109942254464	
16	0.04054800023286	0.04714851036952	
17	0.04326251100172	0.03434657878936	
18	0.04549882326264	0.02362020323623	
19	0.04716662114367	0.01533445742017	
20	0.04819650284122	0.00939805182508	
21	0.04854476991864	0.00543740766513	
22	0.04819650284122		
23	0.04716662114367		
24	0.04549882326264		
25	0.04326251100172		
26	0.04054800023286		
27	0.03746047822666		
28	0.03411327017440		
29	0.03062101271303		
30	0.02709329995710		
31	0.02362927627296		
32	0.02031351571484		
33	0.01721337096090		
34	0.01437781600161		
35	0.01183766578240		
36	0.00960694681421		
37	0.00768512362400		
38	0.00605985858053		
39	0.00470999319516		
40	0.00360847939456		
41	0.00272504914622		

Annex B

Notes from Field Tour of the Santa Cruz River (SCAMA and Mexican Regions)

Tour Date: 20 April 2005

Participants:

Alejandro Barcenas and Edward Shaffer, *ADWR Santa Cruz AMA*.

Keith Nelson, *Arizona Department of Water Resources (ADWR) Hydrology*.

Jesus Quintanar, *International Boundary and Water Commission (IBWC) - Mexico*.

Ricardo Rodriguez, *Commission of Potable Water and Sewers of the State of Sonora (COAPAES) – State of Sonora, Mexico*

Glenn Hansel, *IBWC – United States*

Kosta Georgakakos and Eylon Shamir, *Hydrologic Research Center*.

During the first part of the tour we traveled along the U.S. side of the Santa Cruz River in the AMA region of the northern aquifer and the micro basins south of the Nogales International Wastewater Treatment Plant (NIWWTP). We first stopped at the Elephant Head Bridge Streamflow gauge (Figure AB-1). At this location the channel is very wide (~200 feet) with embankments on the sides. We estimated the current flow in the channel to be 5 cfs. The channel is mainly barren with isolated desert shrubs and cottonwood trees. The conductivity and the recharge rate at this area can be generally classified into three categories: 1) the younger alluvium which is highly conductive located mainly along the river channel (horizontal $K \sim 100$ ft/day); 2) the older alluvium which can be seen in the floodplain area outside of the channels (horizontal $K \sim 30$ ft/day); and the consolidated material of the Nogales formation seen on the hill-slopes with low conductivity (horizontal $K \sim 0.3$ ft/day). For modeling purposes vertical K values are set to $1/10^{\text{th}}$ of the corresponding horizontal K values.



Figure AB-1: The view upstream (south) from Elephant Head Bridge

The second stop was in Tubac at the USGS streamflow gauge site (Figure AB-2). This area is characterized by high water table and a narrow aquifer. The channel is densely vegetated with riparian vegetation. The aquifer is highly responsive to channel flow events.

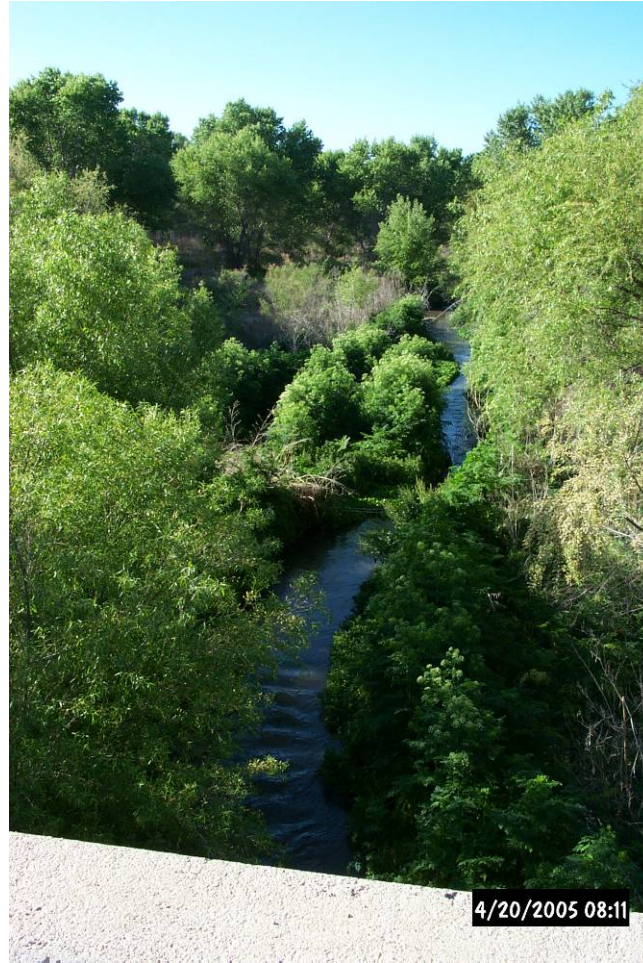


Figure AB-2: The view south (upstream) from the Tubac Bridge

The next stop was at the confluence with Sonoita Creek just downstream of the Nogales treatment plant (Figure AB-3). This is a key point that receives discharge from the treatment plant. There is also a constant release of water into the Sonoita Creek from the Patagonia Lake (located east of the Santa Cruz River). Apparently the water infiltrates into the channel and provides a constant lateral flow contribution to the aquifer at the confluence. The treatment plant release creates the formation of algae and the development of a biological film on the channel bed that reduces significantly infiltration within the stream channel. This biological film, however, is scoured during larger flow events, restoring the natural infiltration rates.

Kino Springs pumping station on the edge of one of the micro basins is a highly productive well field that is vulnerable to rapid decline rates. There are live cottonwood trees near the pump. The horizontal conductivity in the younger alluvium in the micro-basins is estimated to be 500-700 ft/day. Such a rate means that flows up to about 100 cfs are completely recharged into the micro-basins. Generally the micro-basins recharge rate is dominated by the aquifer's capacity to store channel water. As the water content in an upstream micro basin reaches full capacity, the next downstream micro basin receives more channel water for recharge. It appears that the micro-basins can be conceptualized to constitute a series of reservoirs.



Figure AB-3: The Santa Cruz River at the confluence with Sonoita Creek north of the IWWTP

The channel at the site of the Buena Vista streamflow gauge (Figure AB-4), which provides the record of flow for the HRC project, was dry. It is located in a small river bend with the western bank consisting of exposed rocks, with an asymmetric cross section skewed toward the east and forming a wide alluvium channel. We were told that there has not been an event that reached bankfull in recent years. Channel width at this point was estimated to be about 60 ft.

On the Mexican side, we were joined by members of the IWBC and COAPAES. We drove along the Santa Cruz River tracing the river loop all the way to Santa Cruz town near the American border across from Lochiel. We stopped first at the infiltration gallery (Figure AB-5), which consists of a set of perforated pipes lined underground horizontally

to drain channel water into a collection system. The design takes advantage of very high transmissivity and high water table in the young channel alluvium. We looked into one of the gallery wells and the water was flowing at a depth of about 12 ft below the surface. There were two perforated pipes visible, one for high groundwater levels near the channel bed and one at about 10 ft below the surface.



Figure AB-4: The USGS Nogales streamflow gauge -looking northwest across the Santa Cruz River



Figure AB-5: A well at the infiltration gallery in San Lazaro (Mexico)

Next we stopped at a flowing section of the river just upstream of the infiltration gallery (Figure AB-6). We speculated that there is an impermeable layer beneath the channel younger alluvium that creates a shallow groundwater aquifer.



Figure AB-6: Perennial section upstream from the infiltration gallery.

The next stop was in El Cajon streamflow gauging station and the town of San Lazaro (Figure AB-7). The gauge site was renovated in 2003. It is a well designed and maintained gauging station with the potential for high quality data. It includes a concrete weir structure, a water level recording station, and capability (cable and cart) for discharge measurements at various locations along the cross-section of the river. Flow was observed in the channel at this site and was estimated to be about 30 cfs.

Near the town of Santa Cruz there is evidence of substantial agricultural production with irrigated fields of forage crops. The comment was made that agriculture has migrated from apple groves to forage crops, and it has been declining.

We returned to Nogales Sonora through the mountain passage along the international border. The Northern facing slopes at a 6000 ft elevation are covered with lush vegetation indicating heavy and frequent precipitation.



Figure AB-7: El Cajon stream gauge.

During the tour we looked for evidence that might explain the trend of reduction of summer flow peaks at the Buena Vista gauge. We did not see any major developments that occurred recently on the channel affecting the flow crossing to the US. In fact it was mentioned that there are institutional restrictions on agriculture to accommodate water shortage in response to drought. We did not see any channel improvements, reservoirs or other developments. Although the city of Nogales Sonora is growing in a steady rate, it was indicated that the Santa Cruz River basin supplies only 50% of the potable water from deep wells.

